

REPORT DOCUMENTATION PAGE			Form Approved OMB NO. 0704-0188		
<p>The public reporting burden for this collection of information is estimated to average 1 hour per response, including the time for reviewing instructions, searching existing data sources, gathering and maintaining the data needed, and completing and reviewing the collection of information. Send comments regarding this burden estimate or any other aspect of this collection of information, including suggestions for reducing this burden, to Washington Headquarters Services, Directorate for Information Operations and Reports, 1215 Jefferson Davis Highway, Suite 1204, Arlington VA, 22202-4302. Respondents should be aware that notwithstanding any other provision of law, no person shall be subject to any penalty for failing to comply with a collection of information if it does not display a currently valid OMB control number.</p> <p>PLEASE DO NOT RETURN YOUR FORM TO THE ABOVE ADDRESS.</p>					
1. REPORT DATE (DD-MM-YYYY) 29-05-2014		2. REPORT TYPE Final Report		3. DATES COVERED (From - To) 15-Oct-2010 - 14-Feb-2014	
4. TITLE AND SUBTITLE Unsteady Aerodynamic Flow Control of Moving Platforms				5a. CONTRACT NUMBER W911NF-11-1-0010	
				5b. GRANT NUMBER	
				5c. PROGRAM ELEMENT NUMBER 611102	
6. AUTHORS Ari Glezer				5d. PROJECT NUMBER	
				5e. TASK NUMBER	
				5f. WORK UNIT NUMBER	
7. PERFORMING ORGANIZATION NAMES AND ADDRESSES Georgia Tech Research Corporation Office of Sponsored Programs 505 Tenth Street NW Atlanta, GA 30332 -0420				8. PERFORMING ORGANIZATION REPORT NUMBER	
9. SPONSORING/MONITORING AGENCY NAME(S) AND ADDRESS (ES) U.S. Army Research Office P.O. Box 12211 Research Triangle Park, NC 27709-2211				10. SPONSOR/MONITOR'S ACRONYM(S) ARO	
				11. SPONSOR/MONITOR'S REPORT NUMBER(S) 57780-EG.5	
12. DISTRIBUTION AVAILABILITY STATEMENT Approved for Public Release; Distribution Unlimited					
13. SUPPLEMENTARY NOTES The views, opinions and/or findings contained in this report are those of the author(s) and should not be construed as an official Department of the Army position, policy or decision, unless so designated by other documentation.					
14. ABSTRACT This ARO program focused on the experimental investigation of fundamental flow mechanisms that are associated with transitory aerodynamic forces and moments effected by fluidic actuation on the flow boundaries of stationary and moving platforms. Aerodynamic forces and moments are induced on a movable, wire-mounted wind tunnel model of an axisymmetric bluff body with novel embedded fluidic actuation for aft-body control. Control is effected fluidically by interactions of azimuthally- and streamwise-segmented individually-addressable synthetic jet actuators with the embedding flow over the platform. The interaction between the actuation and the local cross					
15. SUBJECT TERMS flow control, axisymmetric platform, wire traverse, synthetic jets, feedback control					
16. SECURITY CLASSIFICATION OF:			17. LIMITATION OF ABSTRACT UU	18. NUMBER OF PAGES	19a. NAME OF RESPONSIBLE PERSON Ari Glezer
a. REPORT UU	b. ABSTRACT UU	c. THIS PAGE UU			19b. TELEPHONE NUMBER 404-894-3266

Report Title

Unsteady Aerodynamic Flow Control of Moving Platforms

ABSTRACT

This ARO program focused on the experimental investigation of fundamental flow mechanisms that are associated with transitory aerodynamic forces and moments effected by fluidic actuation on the flow boundaries of stationary and moving platforms. Aerodynamic forces and moments are induced on a movable, wire-mounted wind tunnel model of an axisymmetric bluff body with novel embedded fluidic actuation for aft-body control. Control is effected fluidically by interactions of azimuthally- and streamwise-segmented individually-addressable synthetic jet actuators with the embedding flow over the platform. The interaction between the actuation and the local cross flow over the moving surface is investigated using high-resolution PIV, while the global aerodynamic effects are assessed from the time-resolved force measurements. Of particular interest is the transitory onset and evolution of streamwise vorticity concentrations, which are amplified by the body-tailored adverse pressure gradient, and their effects on three-dimensional separation.

In Year I, the model's trajectory was prescribed by synchronous activation of shape memory alloy (SMA) segments coupled with a miniature inline force transducer in each of the mounting wires, and the aerodynamic forces and moments were manipulated over a range of pitch attitudes. Flow control effectiveness was demonstrated by nearly complete suppression or significant enhancement of the asymmetric aerodynamic forces and moments that are effected by the model's prescribed motion (§III.1) indicating potential for flight stabilization and attitude control of an airborne platform.

Following these investigations flow-controlled stabilization and steering a free axisymmetric yawing platform was explored in Years II and III (§III.2). Unsteady aerodynamic yaw deflections and moments were effected by transitory flow actuation, and a closed-loop controller was developed to affect a desired, time-dependent model attitude. The interaction between the aft-body actuation and the local cross flow over the moving surface was investigated using high-resolution PIV with specific emphasis on the transitory onset and evolution of vorticity concentrations that are amplified by local adverse pressure gradients, and the effects of three-dimensional separation and forced reattachment on aerodynamic forces and moment for controlling the platform's motion.

These control approaches were demonstrated in Year III (§III.3) using a unique 6-DOF wire traverse traversing mechanism (ARO DURIP) coupled with a dedicated ("inner-loop") feedback controller to remove the model's parasitic mass and inertia. The traverse-driven model motion was tested in multiple degrees of freedom in complex trajectories in which aerodynamic forces and moments could be varied by large fraction of their uncontrolled levels indicating capabilities for steering and stabilization of a free-flying platform without moving (mechanical) control surfaces.

Enter List of papers submitted or published that acknowledge ARO support from the start of the project to the date of this printing. List the papers, including journal references, in the following categories:

(a) Papers published in peer-reviewed journals (N/A for none)

Received

Paper

05/29/2014	4.00	Philip Abramson, Bojan Vukasinovic, Ari Glezer. Fluidic Control of Aerodynamic Forces on a Bluff Body of Revolution, AIAA JOURNAL, (04 2012): 832. doi:
------------	------	--

TOTAL: 1

Number of Papers published in peer-reviewed journals:

(b) Papers published in non-peer-reviewed journals (N/A for none)

Received Paper

TOTAL:

Number of Papers published in non peer-reviewed journals:

(c) Presentations

"Unsteady Aerodynamic Flow Control of a Suspended Axisymmetric Moving Platform", APS DFD Conference Presentation, Baltimore, 2011.

"Synthetic Jet Control of a Yawing Axisymmetric Body", APS DFD Conference Presentation, Grapevine, 2012.

"Motion Control of a Moving Axisymmetric Body using Synthetic Jets", APS DFD Conference Presentation, Pittsburgh, 2013.

Number of Presentations: 3.00

Non Peer-Reviewed Conference Proceeding publications (other than abstracts):

Received Paper

05/29/2014	3.00	Thomas J. Lambert, Bojan Vukasinovic, Ari Glezer. Aerodynamic Flow Control of a MovingAxisymmetric Bluff Body, AIAA SciRech 52nd Aerospace Sciences Meeting13-17 January 2014, National Harbor, Maryland. 13-JAN-14, . : ,
10/22/2013	2.00	Thomas J. Lambert, Bojan Vukasinovic, Ari Glezer. Yaw Control of a Moving Axisymmetric Body using Synthetic Jets, AIAA Aerospaces Sciences Meeting 2013. 07-JAN-13, . : ,
TOTAL:	2	

Number of Non Peer-Reviewed Conference Proceeding publications (other than abstracts):

Peer-Reviewed Conference Proceeding publications (other than abstracts):		
<u>Received</u>		<u>Paper</u>
09/27/2012	1.00	Thomas J. Lambert, Bojan Vukasinovic, Ari Glezer. Unsteady Aerodynamic Flow Control of a Wire-Suspended, Moving Axisymmetric Body, 50th AIAA Aerospace Sciences Meeting including the New Horizons Forum and Aerospace Exposition 09 - 12 January 2012, Nashville, Tennessee. 09-JAN-12, . : ,
TOTAL:		1

Number of Peer-Reviewed Conference Proceeding publications (other than abstracts):

(d) Manuscripts		
<u>Received</u>		<u>Paper</u>
TOTAL:		

Number of Manuscripts:

Books		
<u>Received</u>		<u>Book</u>
TOTAL:		

TOTAL:

Patents Submitted

Patents Awarded

Awards

Graduate Students

NAME	PERCENT SUPPORTED	Discipline
Thomas Lambert	0.50	
FTE Equivalent:	0.50	
Total Number:	1	

Names of Post Doctorates

NAME	PERCENT SUPPORTED
FTE Equivalent:	
Total Number:	

Names of Faculty Supported

NAME	PERCENT SUPPORTED	National Academy Member
Ari Glezer	0.08	
FTE Equivalent:	0.08	
Total Number:	1	

Names of Under Graduate students supported

NAME	PERCENT SUPPORTED
FTE Equivalent:	
Total Number:	

Student Metrics

This section only applies to graduating undergraduates supported by this agreement in this reporting period

The number of undergraduates funded by this agreement who graduated during this period: 0.00

The number of undergraduates funded by this agreement who graduated during this period with a degree in science, mathematics, engineering, or technology fields:..... 0.00

The number of undergraduates funded by your agreement who graduated during this period and will continue to pursue a graduate or Ph.D. degree in science, mathematics, engineering, or technology fields:..... 0.00

Number of graduating undergraduates who achieved a 3.5 GPA to 4.0 (4.0 max scale):..... 0.00

Number of graduating undergraduates funded by a DoD funded Center of Excellence grant for Education, Research and Engineering:..... 0.00

The number of undergraduates funded by your agreement who graduated during this period and intend to work for the Department of Defense 0.00

The number of undergraduates funded by your agreement who graduated during this period and will receive scholarships or fellowships for further studies in science, mathematics, engineering or technology fields: 0.00

Names of Personnel receiving masters degrees

NAME

Philip Abramson

Total Number: 1

Names of personnel receiving PHDs

NAME

Total Number:

Names of other research staff

NAME

PERCENT SUPPORTED

Bojan Vukasinovic 0.05

FTE Equivalent: 0.05

Total Number: 1

Sub Contractors (DD882)

Inventions (DD882)

Scientific Progress

See Attachment

Technology Transfer

Unsteady Aerodynamic Flow Control of Moving Platforms

Final Project Report

August 01, 2010 - July 31, 2013

submitted by

Ari Glezer

**Woodruff School of Mechanical Engineering
Georgia Institute of Technology**

Program Overview

This ARO program focused on the experimental investigation of fundamental flow mechanisms that are associated with transitory aerodynamic forces and moments effected by fluidic actuation on the flow boundaries of stationary and moving platforms. Aerodynamic forces and moments are induced on a movable, wire-mounted wind tunnel model of an axisymmetric bluff body with novel embedded fluidic actuation for aft-body control. Control is effected fluidically by interactions of azimuthally- and streamwise-segmented individually-addressable synthetic jet actuators with the embedding flow over the platform. The interaction between the actuation and the local cross flow over the moving surface is investigated using high-resolution PIV, while the global aerodynamic effects are assessed from the time-resolved force measurements. Of particular interest is the transitory onset and evolution of streamwise vorticity concentrations, which are amplified by the body-tailored adverse pressure gradient, and their effects on three-dimensional separation.

In Year I, the model's trajectory was prescribed by synchronous activation of shape memory alloy (SMA) segments coupled with a miniature inline force transducer in each of the mounting wires, and the aerodynamic forces and moments were manipulated over a range of pitch attitudes. Flow control effectiveness was demonstrated by nearly complete suppression or significant enhancement of the asymmetric aerodynamic forces and moments that are effected by the model's prescribed motion (§III.1) indicating potential for flight stabilization and attitude control of an airborne platform. Following these investigations flow-controlled stabilization and steering a free axisymmetric yawing platform was explored in Years II and III (§III.2). Unsteady aerodynamic yaw deflections and moments were effected by transitory flow actuation, and a closed-loop controller was developed to affect a desired, time-dependent model attitude. The interaction between the aft-body actuation and the local cross flow over the moving surface was investigated using high-resolution PIV with specific emphasis on the transitory onset and evolution of vorticity concentrations that are amplified by local adverse pressure gradients, and the effects of three-dimensional separation and forced reattachment on aerodynamic forces and moment for controlling the platform's motion.

These control approaches were demonstrated in Year III (§III.3) using a unique 6-DOF wire traverse traversing mechanism (ARO DURIP) coupled with a dedicated ("inner-loop") feedback controller to remove the model's parasitic mass and inertia. The traverse-driven model motion was tested in multiple degrees of freedom in complex trajectories in which aerodynamic forces and moments could be varied by large fraction of their uncontrolled levels indicating capabilities for steering and stabilization of a free-flying platform without moving (mechanical) control surfaces.

I. Technical Background

Numerous earlier investigations have shown that stalled or separated flows over external aerodynamic platforms can be either fully or partially attached by fluidic manipulation at or upstream of flow separation. It has been shown that the separating shear layer over stalled 2- and 3-D aerodynamic surfaces is typically dominated by a strong coupling to the instability of the near wake (e.g., Wu et al. 1998). Traditional separation control strategy uses actuation coupling to the narrow-band receptivity of the separating flow at the unstable Strouhal numbers of the near wake (e.g., $St_D \sim O(1)$, Hsiao et al. 1990, Neuberger and Wygnanski 1987, Williams et al. 1991, Chang et al. 1992, Seifert et al. 1993). An alternative approach uses actuation at substantially higher frequencies to decouple the global flow instabilities from fluidic modification of the “apparent” aerodynamic shape of the body (e.g., $St_D \gg O(1)$, Erk 1997, Smith et al. 1998, Amitay et al. 2001, Honohan et al. 2000, Glezer et al. 2005). The global flow characteristics are typically modified with active flow control by issuing a jet through a high aspect ratio orifice along the body surface. More aggressive ‘hybrid’ (combined active and passive) flow control can be achieved by fluidic actuation over a Coanda surface, as shown in a substantial body of work since the 1940s. As shown by Newman (1961), the flow direction of a planar jet can be substantially altered near the exit plane either by the jet adherence to a curved surface that is a smooth extension of the nozzle, or by the reattachment of a separated jet to an adjacent solid ‘Coanda’ surface. The Coanda effect has been the basis of circulation control over lifting surfaces in aerodynamic systems (e.g., Englar 2000). Hybrid flow control was also demonstrated by Nagib et al. (1985) who combined a short backward facing step with a jet to control local separation. This approach was also utilized for internal flows, such as controlling separation in adverse pressure gradients in a diffuser (Lo et al. 2012).

Aerodynamic flow control has also been applied to axisymmetric platforms with an objective to control their airborne flight dynamics. Freund and Mungal (1994) applied steady circumferentially-uniform blowing over Coanda surfaces at the aft corner of the body, leading to drag reduction up to 30%. Rinehart et al. (2003, 2011) investigated the generation of a normal force on an aerodynamic platform using the interaction of a single synthetic jet with an integrated axisymmetric Coanda surface. Their results suggested that the induced force by actuation was equivalent to the lift force on the body at an angle of attack of 3° . McMichael et al. (2004) were able to control the trajectory of a 40 mm axisymmetric spin stabilized projectile by exploiting separated base flow control which effected steering forces and moments. Corke et al. (2008) reported an altered drag and side force, generated with a tangential blowing plasma actuator placed upstream of a Coanda surface on an axisymmetric body. Abramson et al. (2011) investigated the effects of asymmetric flow actuation on an axisymmetric body of revolution with four, equally-spaced azimuthal synthetic jets issuing from within a rearward facing step in the tail, inducing aerodynamic forces and moments on the model with fluidic actuation. Abramson et al. (2012) further studied different active control actuation amplitude modulation schemes for possible utilization in controlling the wake behind an axisymmetric body.

Control of the aerodynamic forces on axisymmetric airborne platforms builds on numerous earlier investigations of the uncontrolled baseline flow and its natural instabilities. The basic motions of spinning projectiles, including natural nutation and precession linear and nonlinear instabilities, induced by Magnus, damping, and normal forces and moments are discussed in detail in the classical work of Nicolaidis (1970). The instabilities of axisymmetric bodies in the presence and absence of spin were discussed in detail by Murphy (1980). While the spin-

stabilized ones are gyroscopically stable to axisymmetric moment instability, they are susceptible to roll resonance (Price, 1967), and spin-yaw lock in (Murphy, 1987), which add complicated non-linear effects to the body dynamics that are in general hard to correct for. In recent years considerable attention has been devoted to the development active control approaches for both fin- and spin-stabilized axisymmetric bodies, including aerodynamic forces induced by a piezoelectric-articulated nose section (Barrett and Lee, 2004), synthetic jet actuation on a spinning projectile (Sahu, 2006), and the swerve response of finned and spin-stabilized airborne bodies to generic control forces (Ollerenshaw and Costello, 2008). In the present work, synthetic jet actuation is applied to investigate the potential for both steering and stabilization in a model that would not use spin or fins for stabilization.

An inherent problem with any experimental aerodynamic study of a nominally ‘free’ body is related to its mounting into a test section. Ideally, the model support should not cause aerodynamic interference (e.g., magnetic-force supports Higuchi et al. 1996), but the predominant supports involve sting mounts that are directly in the body’s wake. An alternative support, aimed at minimizing the wake-support interference, was utilized by Abramson et al. (2011, 2012), where a model is supported by thin static wires. The latter support system is made dynamically modifiable in the present work by utilization of the recent developments in nickel-titanium shape memory alloy wire technology (Zak et al. 2003, Nemat-Nasser and Guo, 2006), and the previously passive-support assembly is fitted with actively controlled support wires. Thereby, the support system enables a versatile and controllable model orientation that can be adjusted both statically and dynamically.

The goal of the present experimental investigation is to assess the fundamental flow mechanisms that are associated with time-dependent aerodynamic forces and moments effected by flow control on a moving aerodynamic platform.

II. Experimental Model

The present investigation is conducted in an open-return wind tunnel at Georgia Tech in a square test section measuring 91cm on the side with a free stream velocity of $U_0 = 40$ m/s. The axisymmetric wind tunnel model (Figure II.1a) is assembled using stereo-lithographed and aluminum components ($D = 90$ mm, $L = 165$ mm, $Re_D = 2.3 \cdot 10^5$). The

mid-section and nose are hollow and connected to the tail assembly by a central shaft. An azimuthal array of four independently-driven synthetic jet actuators (labeled the top, left, bottom, and right actuators, as shown in Figure II.1b) are equally distributed along the perimeter of the tail section and are used to effect aerodynamic control forces and associated moments. Each jet is issued in the streamwise direction with the orifice placed at the bottom of a backward-facing step to the circumference extending into a Coanda surface. The step height, $h_s = 1.5$ mm, is selected to be shallow enough to enable local flow attachment when the control jet is activated, but deep enough to prevent attachment of the free stream flow in the absence of the jet actuation. There is a streamwise cut-in recess downstream of the orifice edge which guides the jet flow and prevents its spanwise diffusion. The actuator geometry is chosen to have a Coanda radius of

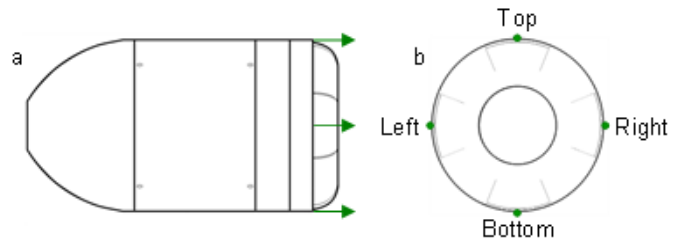


Figure II.1 Side (a) and upstream (b) views of the wind tunnel model with four hybrid fluidic actuators marked by arrows.

$R_C = 12.7$ mm and an orifice height of $h_J = 0.38$ mm ($A_J = 13.03$ mm²), which are based on the parameter studies of Rinehart (2011). The jet actuation leads to the partial attachment of the outer flow along the surface resulting in a reaction force by the turning of the outer flow into the wake region.

In order for all synthetic jets to induce comparable aerodynamic forces on the axisymmetric body, they are calibrated over a wide range of actuation frequencies, f_A , and applied powers P_A . The actuation frequency is scaled by the hydraulic diameter ($\sim 2h_J$)

yielding $f_A^* = 2f_A h_J / U_0$, and the actuation power is scaled similar to the force coefficients $P_A^* = 24P_A / (\pi \rho U_0^3 D^2)$. The jet calibration is executed using hot-wire anemometry in a test stand where the time-resolved velocity of each synthetic jet is measured at the center of each of the actuator orifices. The resulting velocity measurements yielded a rectified sinusoidal waveform representing the suction and expulsion phases of the jet formation. The peak of the expulsion velocity, U_J , is recorded over a frequency range of $0.035 < f_A^* < 0.050$ at excitation powers of $P_A^* \cdot 10^3 = 2.0, 3.3$, and 4.6 . The jet momentum coefficient is calculated as a ratio of jet to free stream momentums, $C_\mu = (4U_J^2 A_J) / (\pi U_0^2 D^2)$, and is presented in Figure II.2. These calibration curves are used to pre-select the jet momentum coefficient utilized in the present work. It is noteworthy that no sharp resonance peaks are observed, which combined with a decrease of the resonance frequency with increasing power indicates weakly nonlinear behavior.

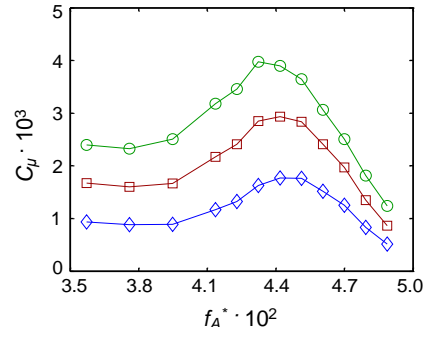


Figure II.2 Variation of the jet momentum coefficient, C_μ with the actuation frequency, f_A^* , and actuation power, $P_A^* \cdot 10^3 = 2.0$ (\diamond), 3.3 (\square), and 4.6 (\circ).

III. Aerodynamic Flow Control of an Axisymmetric Bluff Body: Discussion of Results

In the present report, the discussion of the technical results is organized in three primary parts:

III.1 Quasi-Steady Actuation *Flow control effectiveness was demonstrated by nearly complete suppression or significant enhancement of asymmetric aerodynamic forces and moments that are effected by the model's prescribed motion.*

III.2 Free Yawing, 1-DOF Axisymmetric Body *Closed-loop control of desired, time-dependent model attitude using unsteady aerodynamic yaw deflections and moments effected by transitory flow actuation.*

III.3 Aerodynamic Flow Control in 6 DOF Motions *Design, development and validation of a control system for prescribed dynamic motions of wire-mounted wind tunnel models in six degrees of freedom.*

III.1 Quasi-Steady Actuation

Quasi-steady and transitory controlled interactions of integrated synthetic jet actuators with the cross flow over an axisymmetric bluff body are used to induce localized flow attachment over the body's aft end and thereby alter the global aerodynamic forces and moments. Actuation is effected using an array of four aft-facing synthetic jet actuators (§II). The axisymmetric model is supported by eight wires, each including a shape memory alloy (SMA) segment and a miniature inline force transducer, and the model position is varied both quasi-statically and dynamically by controlling the strain of individual SMA wire segments. The aerodynamic forces and moments on the moving platform are manipulated over a range of model attitudes in pitch. The efficacy of open-loop active flow control is demonstrated by either nearly complete suppression or significant enhancement of asymmetric aerodynamic forces and moments that result from the model's motion by prescribed activation of the SMA wires.

III.1.1 Experimental Setup and Calibration

The frame and components used to mount this axisymmetric model in the wind tunnel are shown in Figure III.1. The basic frame structure is a cylindrical frame that is secured to the tunnel wall, as shown in side view in Figure III.1a and back view in Figure III.1b. This frame consists of two steel circular rings that are connected by four streamwise cylindrical rods.

The connection to the wind tunnel wall utilizes dampers, to isolate the model from tunnel vibrations. The wind tunnel model is mounted within the frame using eight stainless steel wires, which are each coupled directly to a $L_{SMA} = 10$ cm long and $D_{SMA} = 0.5$ mm diameter shape memory alloy (SMA) wire (Figure III.1b). The model mounting cables are oriented such that they are not in line with the model's center, forcing the body to rotate when offset tensions are applied, as depicted in Figure III.1. All of the eight SMA wires are individually actuated from the laboratory computer using an eight-channel power amplifier and transmitted through electrical wires that are fastened directly to the frame. Each SMA wire is directly connected to an inline force measurement transducer that was custom designed and constructed (after Abramson et al. 2011). The force-measurement transducers are connected to respective modified violin tighteners embedded in the frame which can be tightened or loosened to control the initial pretension on the model. The model positioning is initially set manually through the violin tuners, while the dynamic motion from the initial state is achieved through SMA wire

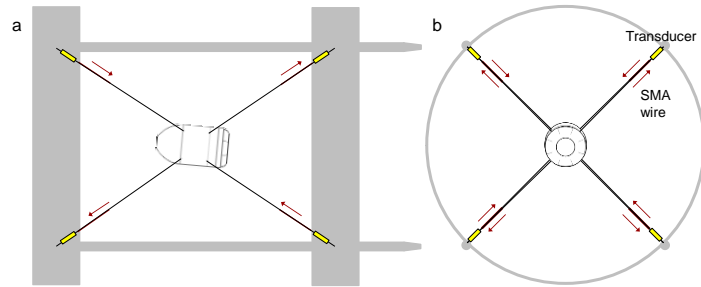


Figure III.1 Schematics of the axisymmetric model setup oriented to a pitch up position by the SMA wires, side (a) and upstream (b) views.

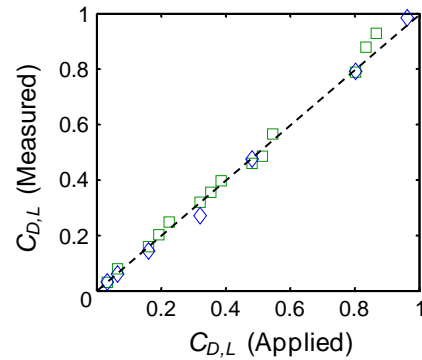


Figure III.2 Measured versus applied force coefficients for drag (◇) and lift (□) directions.

activation.

The force transducers are used to measure the time-dependent tension in the mounting wires with sufficient resolution to determine the aerodynamic forces and moments on the model. As noted above, each transducer is mounted in line with the support wires, but its auxiliary circuitry is mounted directly onto the frame. Each of the force transducers is independently calibrated ahead of the tunnel measurements using precision weights to produce a set of linear calibration curves (output voltage vs. applied load). The transducers are also calibrated to check and correct for their weak temperature dependence (output voltage vs. ambient temperature). The resulting calibration is periodically checked by applying known static forces on the model in the lift and drag directions and measuring the resulting force. The forces and moments on the model are presented using force coefficients $C_{D,S,L} = 8F_{D,S,L} / (\pi\rho U_0^2 D^2)$ for drag, side, and lift forces, respectively, and moment coefficients $C_{M,Y} = 8F_{M,Y} / (\pi\rho U_0^2 D^2 L)$ for pitch and yaw moments, respectively. The roll moment is not resolved using the present orientation of mounting wires, but due to the axisymmetry of the setup is assumed to be zero. Figure III.2 shows the measured vs. applied force coefficients in the lift and drag directions, which are in good agreement, particularly in the primary range of interest at lower force coefficients ($C_{D,L} < 0.5$).

Prior to the aerodynamic measurements, a study was conducted in order to assess feasibility of the novel SMA wire utilization for the model static and dynamic orientation in the wind tunnel test section. The SMA wire is a Nickel-Titanium alloy that rearranges its molecular structure from its initial Martensite phase at temperatures below 21°C to an Austenite phase at temperatures above 47°C, with a mixture of the two phases in between those temperatures (Nemat-Nasser and Guo, 2006). As it transitions between these two phases, the wire contracts and, therefore induces an increase in tension. The wire can be operated such that its tension increases or decreases relative to a selected intermediate operating point. Operation of multiple SMA wires can lead to translation and rotation of the model in the frame. The temperature-induced phase change is controlled by Joule heating from the power dissipated through the wire. In the present experiments, the computer-controlled power supply is utilized to statically and dynamically alter the model orientation through the individually-controlled current through each of the SMA wires, a novel concept of dynamical model adjustment in the wind tunnel.

The transient activation of SMA wire with applied power, P_{SMA} , is

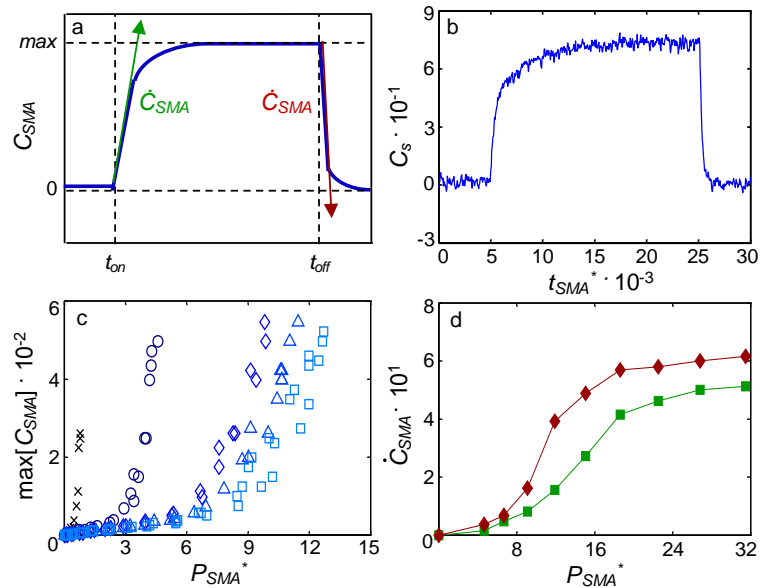


Figure III.3 Ideal (a) and measured (b) SMA force coefficient, C_{SMA} , with time, maximum C_{SMA} with varying power, P_{SMA}^* , for varying tunnel speeds, $U/U_0 = 0$ (x), 0.2(o), 0.5(◇), 0.75(△), and 1(□) (c), and C_{SMA} onset (■) and termination (◆) rates, \dot{C}_{SMA} , with varying P_{SMA}^* for $U/U_0 = 1$ (d).

modeled by a linear tension rate of change, \dot{F}_{SMA} , after which the maximum tension, F_{SMA} , is established. After wire deactivation, it then retracts back to its initial state, although the \dot{F}_{SMA} for retraction is typically different than for contraction, due to cooling of the wire through convection occurring on a different time scale than heating of the wire through Joule heating. The scaling of SMA parameters presented in Figure III.3 is given for time $t_{SMA}^* = tU_0/L_{SMA}$, force coefficient $C_{SMA} = 2F_{SMA}/(\rho U_0^2 D_{SMA} L_{SMA})$, force rate coefficient $\dot{C}_{SMA} = 2\dot{F}_{SMA}/(\rho U_0^3 D_{SMA})$, and applied power $P_{SMA}^* = 6P_{SMA}/(\rho U_0^3 D_{SMA} L_{SMA})$. The SMA wire operation is characterized theoretically (Figure III.3a) and experimentally at the tunnel nominal air speed $U/U_0 = 1$ (Figure III.3b). The SMA dynamic effect is dependent on the tunnel air speed, U , and is tested for multiple speeds ($U/U_0 = 0, 0.2, 0.5, 0.75$, and 1) and the realized maximum force coefficients, C_{SMA} , are shown as a function of applied power, P_{SMA}^* , in Figure III.3c. The force rate coefficient, \dot{C}_{SMA} , for both contraction and expansion vary with P_{SMA}^* and these rates are examined in Figure III.3d for the primary case of interest of $U = U_0$. It should be noted that the relaxation force rate is higher than the contraction force rate which would, in principle, induce a non-symmetric cyclic force oscillation for a given applied power. Therefore, the rise and fall powers need to be preset for the resulting rise and fall times to be matched for a symmetric dynamic model motion. In addition, for step dynamics, it is desired to achieve maximum rise and fall times for small steady state force changes, requiring fast commanded transitions of applied power.

In the present investigation the SMA wires are used only to manipulate the model's pitching motion, although by full utilization of all eight SMA wires, many other prescribed model motions can be realized, depending on the prescribed wire activation. Therefore, in order to manipulate only pitch, the SMA wires were manipulated such that there is a significant induced net pitching moment on the model as well as minimal induced net forces and yawing moment. This was executed by increasing the tension in the upstream two wires at the bottom of the model and the downstream two wires at the top of the model, as well as decreasing the power in the other four wires to induce a pitch up moment, and therefore induce a positive pitching angle. For a pitch down orientation, the opposite SMA power pattern was applied. The large initial pretension in the wires as well as the large force in each of the SMA wires generated by the applied power, relative to the aerodynamic forces on the body, validate an assumption that the model remains centered in the frame as it undergoes pitching motion. Under this assumption, the pitch of the model is measured experimentally by a laser vibrometer, which is mounted directly above the test section and focused on the model upper surface along its centerline, and at a known location downstream from the center of the model x_L . The pitching angle θ can then be extracted from the geometrical relationships among the known values x_L , D , and the time-resolved model displacement Δz measured by the laser vibrometer.

To align the model in the wind tunnel test section, both the manual pre-tension and the SMA controllable tension are utilized. First, each support wire on the frame is manually pre-tensioned ($C_{SMA} \sim 400$) in still air. Afterwards, the test section speed is varied and the measured forces are monitored. The pretension component of the wire tensions are then slightly adjusted until there is negligible change in the lift or side forces with varying tunnel speed (typically less than 5% of the increase in drag force), and then the model is considered aligned with the flow. After the initial alignment procedure, all of the power outputs to the SMA wires are activated such that they are at an intermediate temperature near the beginning of their material transition ($\sim 25^\circ\text{C}$), which adds an additional tension on each wire ($C_{SMA} \sim 150$). The test section speed is then

varied once and the force measurements are utilized to verify that the model is still aligned with the flow or ‘fine tune’ the SMA power if it needs a minor realignment.

III.1.2 Centered Static Model

Prior to examining the dynamic flow control scenarios in the current study, the flow control effects on a centered static model are first assessed in the current experimental setup. The actuation signal is first set to a frequency near the resonance of the synthetic jets based on the prior characterization ($f_A^* = 0.045$). Since there is no characteristic time of the model motion, the time is scaled by the model convective time scale, $t_C^* = tU_0/L$. Initially, the top jet is tested with $C_\mu \cdot 10^3 = 0.2, 0.8, 2.0$ and 3.0 , and the forces and moments on the model are recorded over a time span of $0 < t_C^* < 500$ prior to activation, $500 < t_C^* < 1500$ during actuation, and $1500 < t_C^* < 2000$ following the termination of actuation, where this time range is chosen such that both transient and quasi-steady effects associated with actuation onset and termination can be captured. The corresponding time traces of the actuation-induced force and moment coefficients ΔC_D , ΔC_S , ΔC_L , ΔC_M , and ΔC_Y are shown in Figures III.4a-e, respectively. Here, the moment coefficients, ΔC_M and ΔC_Y are defined relative to the center of the wire mounts on the model ($x_C = 0.54L$ from the nose). In addition, the sign of ΔC_S is defined to make ΔC_D , ΔC_S , ΔC_L a right handed coordinate system, the sign of ΔC_M is defined counter-clockwise positive around ΔC_S , and the sign of ΔC_Y is defined counter-clockwise positive around ΔC_L . Therefore, a positive ΔC_M indicates a tendency to move the model pitch up and hence when the top jet is activated it induces a positive lift force and a negative pitching moment on the model through alteration of the aerodynamic flow at the aft end. These results are in accord with the prior study (Abramson et al. 2011), yielding a maximum $\Delta C_L = 0.1$, virtually no ΔC_S , and a weak $\Delta C_D \sim 0.01$. The accompanying $\Delta C_M = 0.006$ is also comparable with the prior study, and there is also virtually no ΔC_Y . It is important to note that the pitch measurement has a transient oscillating rise and decay at a period of $t_C^* = 10.5$ (~ 23 Hz), which is associated with the natural frequency of the system. The excited pitch resonance decays back to baseline level in $t_C^* \sim 300$, which is associated with the natural damping of the system.

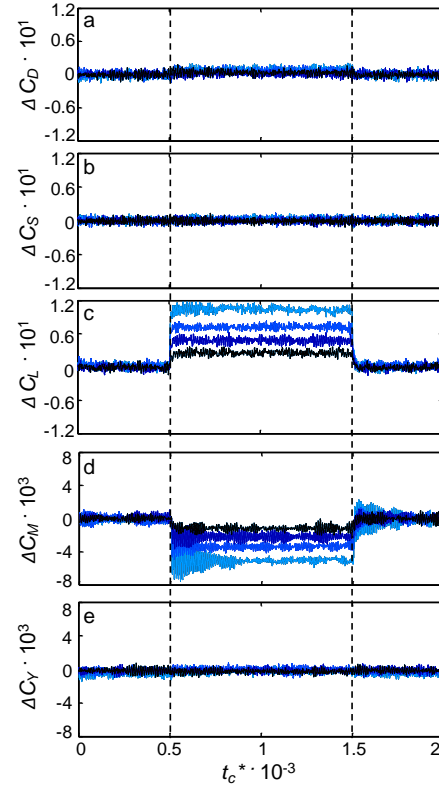


Figure III.4 Time traces of the relative measured drag (a), side (b), lift (c), pitch (d), and yaw (e) coefficients for the flow continuously actuated on from $t_c^* = 0.5-1.5 \cdot 10^{-3}$, with square amplitude modulation at $C_\mu \cdot 10^3 = 0.2, 0.8, 2.0$ and 3.0 , from darkest to lightest color, respectively.

The individual effect on the flow for the remaining (three) jets is characterized in a similar manner, and the steady time-averaged induced lift (ΔC_L) and pitching moment (ΔC_M) coefficients with C_μ are shown in Figures III.5a and b respectively. These data show an initially linear variation of induced forces with jet momentum that begins to saturate approximately when the jet peak velocity exceeds the free stream speed ($C_\mu = 3 \cdot 10^{-3}$) with $\Delta C_L = 0.1$ and $\Delta C_M = 0.006$. There was not a noticeable trend in variation of the side force, drag, or yaw moment with C_μ and they are not presented in this figure. Based on these characterizations, the jets' operating C_μ is typically set to 0.003 for the rest of the current study, as an optimized parameter that induces the maximum effect with the minimized control jet momentum.

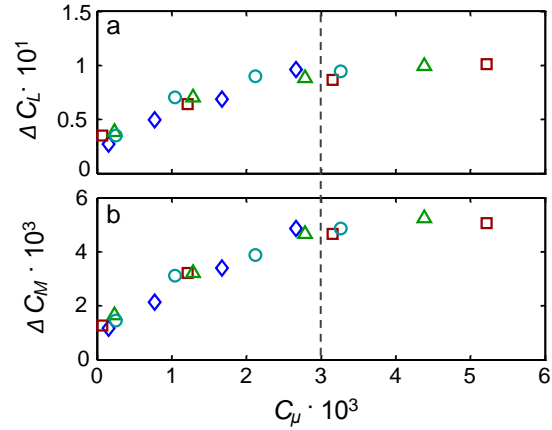


Figure III.5 Induced change in effective lift (a), and pitch coefficients (b), with the jet momentum coefficient, C_μ , for top (\diamond), right (\square), left (\triangle) and bottom (\circ) jets with the selected operation parameter shown with a dashed line.

As already noted in connection with Figure III.4, step activation and deactivation of the control jets introduces transient model oscillations at its natural resonance, which is particularly evident in the measured moment coefficient. Although it is very important to understand such transients from the standpoint of a delay between the actuation onset/termination and its full aerodynamic effect on the body, it is recognized that the natural resonance in free flight may be significantly different from the natural resonance observed in this tunnel setup. Therefore, it is expected that a better estimate of the actuation transient effects is assessed by direct measurements of the flow transients associated with actuation. Natural transient oscillations in the direct force measurements can be, alternatively, bypassed by ‘softening’ a sharp step onset and termination of actuation.

PIV measurements in the central vertical plane are taken to illustrate the changes effected by the flow control actuation in the wake, and all of the PIV presented in this study utilizes ensemble

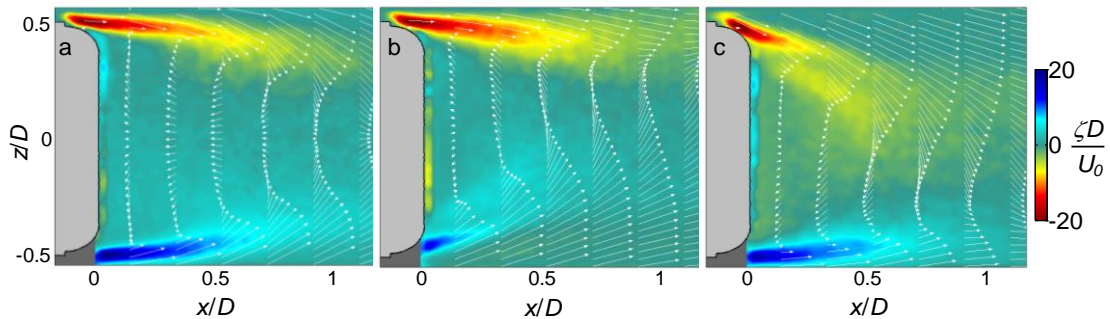


Figure III.6 Raster plots of the mean vorticity field, ζ , with overlaid equidistant mean velocity vectors with a pitching angle $\theta = 0$, for the baseline (a), and the flows controlled by the top (b) and bottom (c) jets at $C_\mu = 3 \cdot 10^{-3}$.

averages of 340 image pairs. The ensemble-averaged flow fields of the velocity, U , and vorticity, ζ , of the baseline flow at $\theta = 0$ for the unactuated flow, as well as controlled by the top and bottom actuator are shown in Figure III.6. All the flow fields are presented in terms of the equidistant averaged velocity profiles and a raster plot of the nondimensionalized vorticity field ($\zeta D/U_0$). The baseline flow (Figure III.6a) is fairly symmetric, where the reversed flow domain of the wake extends to slightly less than $x/D = 1$, which is in accord to the previous investigation of a smaller model (Abramson et al. 2011). The axisymmetric shear layer that forms at the point of flow separation off the body is marked by high vorticity levels ($\zeta D/U_0 > 20$) and it should also be noted that the different sense of vorticity in the upper and lower portions of the shear layer are artifacts of the x-z coordinate system of the measurement plane, in place of a cylindrical one. As either of the jets is activated with $C_\mu = 0.003$ (Figure III.6b,c), a significant vectoring of the affected side of the flow is measured (note the high vectoring angle of the shear layer), largely suppressing the reversed flow region at that side and inducing a dominant asymmetry in the wake, and the effect of the top jet vs. the bottom jet on the flow field are approximately symmetric opposites, as expected.

To understand the global wake development outside of the plane of symmetry, the alteration of the wake behind the model is investigated through PIV measured in the five planar fields of view with a constant offset of $\Delta y = 0.07D$, starting at the central plane. The axisymmetric geometry is then utilized to produce five effective rotated fields of view, and the streamwise velocity, u , and the cross-stream velocity, v_c , are extracted as the parameters of interest out of all the planes. Figure III.7 shows contour plots of the cross-stream velocity component of the wake. The cross-stream velocity is contoured from $-0.25 < v_c/U < 0.25$ with v_c defined to be positive when it is directed away from the center of the model, to clearly mark the actuation-induced asymmetry (commensurate with induced steering forces).

Figure III.7a shows the unactuated velocity field, where the outer flow is directed towards the center of the model through the Coanda effect, and the inner flow near the model surface is directed away from the center for continuity. Upon activation of all four jets in Figure III.7b, the region of flow directed away from the center is diminished in the center plane, and enlarged in the three furthest off-center planes. When a single jet is activated (Figure III.7c), there is a large asymmetry induced in the flow, which results in a large side force and pitching moment on the model. Figure III.7d shows the activation of two adjacent jets, which shows a response similar

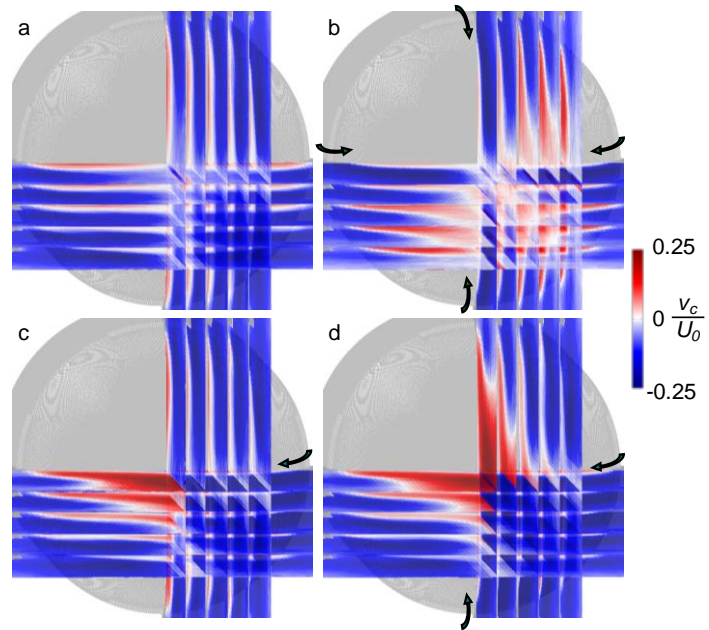


Figure III.7 Raster plots of the cross-stream velocity away from center-plane, v_c , for the baseline (a), and the flow actuated by four (b), one (c), and two (d) jets at $C_\mu = 3 \cdot 10^{-3}$, shown in central planes and four planes offset incrementally by $\Delta y/R = 0.07$

to the additive response expected from both of the jets independently (compare Figure III.7c and d). The result shows that there is little cross-correlation between the adjacent jets and the effect of these jets on the lift force and pitching moment can be assumed independent from the side force and yawing moment, caused by the segmented actuator distribution (Figure II.1).

III.1.3 Step-Pitch Model Displacement

One of the objectives of the present investigations is to examine the control authority of the synthetic jet actuators for the generation of asymmetric (radial) aerodynamic forces over a range of angles of attack. Flow control actuation can be used to either cancel or enhance asymmetric aerodynamic forces and moments that are engendered by nonzero angle of attack. These effects are initially assessed at steady body attitudes, where its static orientation is set by the SMA wires at a controlled angle with respect to the laboratory frame and held fixed, prior to the application of the flow control. In the initial study of static model positioning at non-zero angles of attack, the orientation was restricted to pure pitching.

Figure III.8 shows the resultant forces and moments with varying static pitching angles, θ . The forces induced entirely by non-zero angles of attack are shown in Figures III.8a-e, and the incremental force induced by the top jet actuation at these fixed angles in a range of $-3 < \theta/\theta_0 < 3$ are shown in Figures III.8f-j for $C_\mu = 3 \cdot 10^{-3}$. Figure III.8a shows the drag coefficient variation,

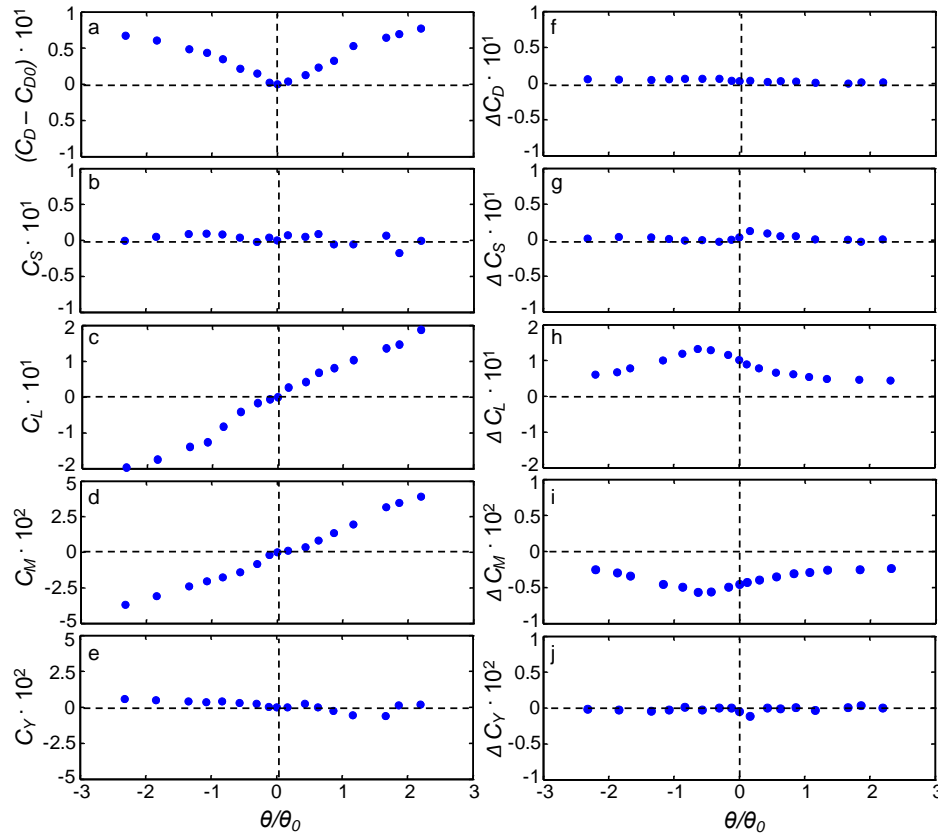


Figure III.8 Resultant static drag (a,f), side (b,g), lift (c,h), pitch (d,i), and yaw (e,j) coefficients with the pitch angle θ , with the induced changes due to the model orientation only (a-e), and due to actuation only (f-j).

which is measured relative to the baseline drag on the model C_{D0} at U_0 , and is symmetric about zero θ , as expected. The measured side and yaw coefficients shown in Figures III.8b and e, respectively, are nominally zero, and the measured small but nonzero changes are attributed to positioning deviations and/or small model imperfections. Other characteristics of these measurements are similar to low-angle pitching of airfoils, such as a linear variation of the lift and pitching coefficients with small θ (Figures III.8c and d, respectively). The data in Figure III.8d show that the present model is unstable, and when the model is pitched (up or down), the change in pitching moment is of the same sense as the change in θ , where the pitching moment acts to further deflect the model off center. Figure III.8f shows the induced drag coefficient which is slightly positive at all θ . Similar to Figures III.8b and e, Figures III.8g and j show nominally zero side and yaw coefficients with some deviation. The most dominant induced changes on the model forces and moments are induced in the lift (Figure III.8h) and pitch (Figure III.8i) coefficients. For this range of θ , the ΔC_L is approximately the same order of magnitude as the C_L , while the ΔC_M is approximately one fifth of the magnitude of C_M . A notable feature of the jet actuation is that the lift and pitch induced by each jet have a maximum when the model's centerline is tilted in the opposite direction (i.e., when the top jet is actuated, the peak force and moment occur at $\theta/\theta_0 \sim -2/3$). Although the effects of actuation remain significant over the entire range of θ , these data show that the actuators optimal performance (peak magnitudes of ΔC_L and ΔC_M) is tied to their favorable orientation into the free stream.

To illustrate the flow control effect on the near wake behind the body at nonzero pitch angle, PIV measurements are taken at $\theta = 2\theta_0$ (Figure III.9, using the same control as in Figure III.6). Contrary to the actuation at $\theta/\theta_0 = 0$ shown in Figure III.6, where the wake is nominally axisymmetric, the model alignment at $\theta = 2\theta_0$ induces asymmetry in the wake, as the outer flow is favorably aligned over the upper surface, and is also assisted by the Coanda-profiled tail (Figure III.9a). This, in turn, causes the change in C_D and C_L . It should be noted that the jet-induced wake flow fields are similar to the respective flow fields at $\theta = 0$ (compare Figures III.9b,c to III.6b, c). The major difference is that the activation of either jet at the present case is coupled with the altered outer flow and the pre-existing asymmetry in the flow field as shown in Figure III.9a. The orientation-induced vectoring of the outer flow becomes enhanced upon activation of the top jet, and is manifested by enhanced wake asymmetry. Likewise, when the bottom jet is activated, significant vectoring of the outer flow at the lower side is achieved, which partially suppresses the pre-existing vectoring on the upper side. It is noteworthy that because the jet-induced flow fields from the asymmetric and symmetric flows and the baseline flow field is initially vectored downwards, the top jet which vectors the wake downwards has a

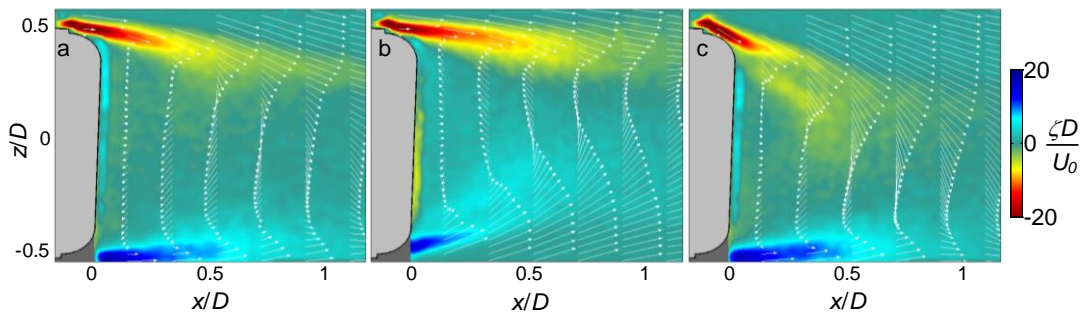


Figure III.9 Raster plots of the mean vorticity field, ζ , with overlaid equidistant mean velocity vectors with a pitching angle $\theta = 2\theta_0$ for the baseline (a), and the flows controlled by the top (b) and bottom (c) jets at $C_\mu = 3 \cdot 10^{-3}$.

less significant effect, and the bottom jet which vectors the wake upwards has a more significant effect. This observation is in agreement with the findings of Figure III.8 where the actuators have a more favorable effect when they are inclined into the free stream.

To characterize transient effects during dynamic model pitching and their coupling to the flow control, the model's time-resolved forces and moments are recorded both during uncontrolled and controlled step change in pitch. Initially ($0 < t_C^* < 500$), the model is centered, and at $t_C^* = 500$ undergoes a step change in angle of attack to $\theta = \theta_0$. At $t_C^* = 1000$, its pitch is step-changed back to zero angle of degrees, and held at that position for $1000 < t_C^* < 1500$. The measured C_D , C_L , C_M , and θ are shown in Figure III.10 in blue, and for brevity, the nominally zero C_S , and C_Y are omitted. The terminal values of all of the forces and the moments agree for the static model orientation at $\theta = \theta_0$, as expected (Compare Figure III.10 and III.8). The two controlled cases are applied such that the top/bottom actuator is also step activated in sync with the model initial motion ($t_C^* = 500$) and then terminated with the model pitch back to the center ($t_C^* = 1000$). The resulting forces and moments are shown in Figure III.10 in red and green, for the top and bottom jet activated, respectively. Here, the top jet actuation amplifies the lift force and suppresses the moment, while the bottom jet actuation has the opposite effect (Figure III.10b and c). The variation of the realized magnitudes of C_D , C_L , C_M , and θ with actuation are analyzed further in Figure III.11.

There are several distinctions between the flow control effects on the dynamic step (Figure III.10) and on the static equivalent change in pitch (Figure III.8). First, when the bottom actuator is applied and terminated, the lift force (Figure III.10b) exhibits transient spikes, which in the case of the control onset ($t_C^* = 500$) induces an initial negative lift force coefficient. Knowing that the bottom-jet actuation induces a lift force opposing the force induced by the pitch-up motion (and vice versa), this transient spike can be explained by consideration of the time scales. The flow control induces a wake response on the order of the model convective time scale ($\sim 1t_C^*$, as shown in Figure III.4c) and hence the corresponding aerodynamic force and moment response is much faster than the dynamics of the model, which is an order of magnitude slower ($\sim 10t_C^*$). As the body approaches its steady equilibrium position, actuation induced ΔC_L balances the baseline C_L and results in almost no net lift. Similarly, at the control termination ($t_C^* = 1000$), the flow control effect relaxes much faster than the body repositioning back to center, and the net C_L has a transient positive spike before settling back to zero. In order to suppress these transients, the flow control onset and termination

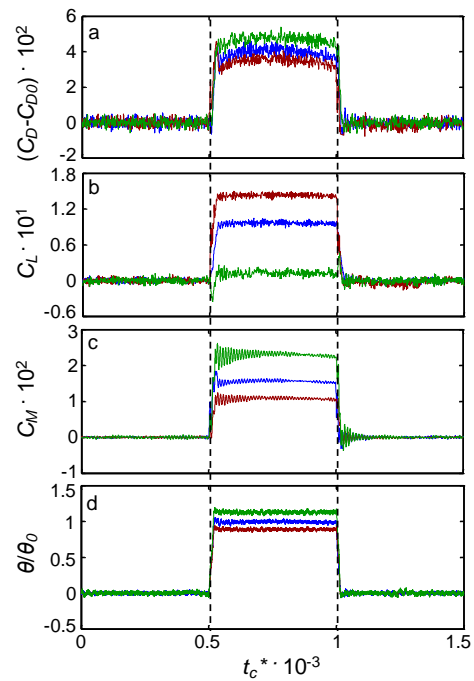


Figure III.10 Time traces of relative drag (a), lift (b), and pitch (c) coefficients, and pitching angle θ (d) for the uncontrolled (blue), and the model controlled by top (green) and bottom (red) jets from $t_C^* = 0.5$ – $1 \cdot 10^{-3}$, for a commanded pitching step of $\theta = \theta_0$.

would need to be amplitude modulated by a signal on the order of the body dynamics. Second, the step amplitude modulation of the actuation signal causes a resonance in the system shown in the realized C_M (Figure III.10c) which is similar to the resonance observed prior for the centered model. Although the resonance lasts on the same order of $t_C^* \sim 300$, the amplitude of the resonance is more severe for actuation that increases C_M , less severe for actuation that suppresses C_M , and isn't noticeably present in the unactuated case. Third, the physical model displaces to a different θ dependent on the actuation applied during the model transition. This is due to the SMA wires moving the model by imposing a fixed pitching moment, and not correcting for the effect of the fluidic control imposed on the model, which causes slight deflection (Figure III.10d). Finally, the drag coefficient has a smaller percentage change with actuation than both the lift and pitch coefficients.

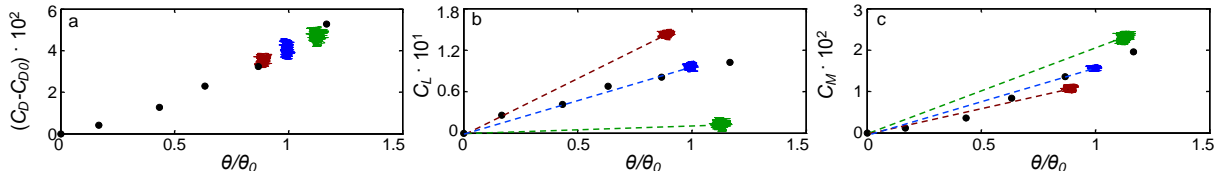


Figure III.11 Resulting quasi-steady magnitudes of relative drag (a), lift (b), and pitch (c) coefficients with the corresponding pitch angle, measured for the uncontrolled (blue), and the model controlled by top (green) and bottom (red) jets. The corresponding static results (\bullet) are shown for reference.

To quantify the steady state amplitude changes of C_D , C_L , C_M , and θ for a dynamic pitching step, the change in the aerodynamic coefficients with θ is shown in Figure III.11 for the quasi-steady positioning during $750 < t_C^* < 1000$ of Figure III.10. In addition, the static-induced changes in C_D , C_L , C_M with θ are also overlaid on Figure III.11, based on Figures III.8a,c, and d. Although the C_D varied a significant amount in Figure III.10a, it becomes apparent in Figure III.11a that this variation is coupled with the attained θ of the model, and the C_D measured with both top and bottom jet actuation are closely aligned with the static C_D curve. Figure III.11b shows that the C_L is almost entirely dampened and the realized θ is higher causing a decrease of C_L/θ by 92% when bottom actuation is applied during the dynamic step. When the top actuation is applied, the C_L is augmented and the realized θ is lower causing an increase of C_L/θ of 65%. Similarly, Figure III.11c shows a 23% decrease in C_M/θ with the bottom actuator active during the dynamic step, with a respective 30% increase in C_M/θ when the top actuator is active.

III.1.4 Harmonic Pitch Motion

The primary goal of the present investigation is to analyze the efficacy of the synthetic-jets flow control in the presence of a slowly changing aerodynamic environment. Initially, the dynamic forces and moments measured during a dynamic model oscillation are compared with the corresponding static forces measured when the model is held at static θ . For this test, a cyclic sinusoidal pitching at $k = 0.013$ and amplitude $\theta_0 = 1.5^\circ$ is imposed on the model using the SMA wires. The aerodynamic forces and moments are recorded with and without the top actuator active for the entire duration of this cycle, where the increments ΔC_D , ΔC_L , and ΔC_M (Figures III.12d-f) are differences between the controlled case and the dynamic motion induced C_D , C_L , and C_M (Figures III.12a-c). For brevity, the nominally zero C_S , C_Y , ΔC_S , and ΔC_Y are omitted from this analysis. The corresponding motion-induced and actuation-induced forces and moments with static θ from Figure III.8 are overlaid on Figure III.12, for comparison. Figures

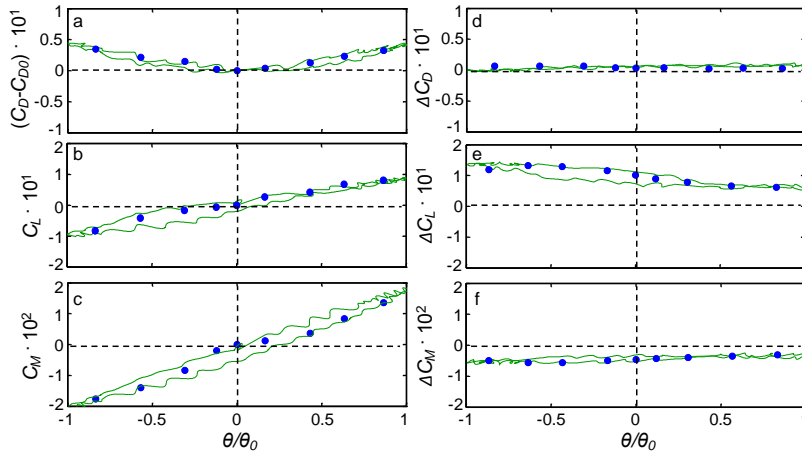


Figure III.12 Resultant motion-induced (a,b,c) and actuation-induced (d,e,f) dynamic drag (a,d), lift (b,e), and pitch (c,f) coefficients with a pitching amplitude of $\theta = \theta_0$ at $k = 0.013$. The corresponding static results (•) are shown for reference.

indicating that unsteady aerodynamic effects of actuation for this dynamic motion are also relatively small. The slight hysteresis that is observed in Figure III.12 is attributed to the small variation of the realized model motion from perfect sinusoidal motion, causing deviations in the model acceleration as well as slight unsteady aerodynamic effects. It is noteworthy that for this amplitude, θ_0 , and frequency, k , the magnitude of the lift force induced by pitching motion (Figure III.12b) and induced by the actuation (Figure III.12e) are approximately equal, and therefore these operation parameters are sufficient for suppressing the aerodynamic lift force on the model by the actuation-induced lift force. In addition, Figure III.12e shows that the dynamic actuation-induced lift force is larger when the actuator is inclined into free stream, similar to the static actuation induced lift force. This implies that the top actuator has a stronger effect when the model is pitch down, and therefore pitch down will be considered the favorable pitching direction for the top actuator.

Active flow control can be used to either enhance or suppress the dynamic forces/moments that are induced during the body's motion, which, in turn, can be utilized for either platform steering or stabilization during flight. As the motion-induced and actuation-induced lift forces were similar for the above model pitch oscillation shown in Figure III.12, this dynamic motion is used as an example for the active fluidic control. Here, three different flow control functions are created with a goal of controlling the aerodynamic lift force on the model in the open-loop approach, and are presented in Figure III.13. All of these control functions are designed relative to θ , which is shown in Figure III.13a. For the first flow control function, only the bottom jet was activated with a sinusoidal-modulated maximum jet momentum coefficient $C_{\mu} = 2 \cdot 10^{-3}$ during the first half of its pitching phase (when the model pitches up) for $0 < t_p^* < 0.5$. The amplitude-modulated actuation signal is shown as a cartoon relative to θ in Figure III.13b, and the C_{μ} was adjusted such that the induced ΔC_L matches the motion-induced C_L in magnitude. The objective of this control function is to keep the aerodynamic force constant across the first half of the model oscillation cycle using a single actuator. The second flow control function (Figure III.13c) has the same operation conditions for the bottom jet, and includes the additional

III.12a-c show that the static and dynamic C_D , C_L , and C_M are similar, despite the pitch oscillations, which indicates that the unsteady aerodynamic effects at these frequencies are relatively small. Note that the oscillation frequencies are much lower than the natural shedding frequencies off the body ($k \sim 1$), and therefore there is no direct manipulation of the natural wake shedding. Figures III.12d-f also show that the static and dynamic ΔC_D , ΔC_L , and ΔC_M are similar,

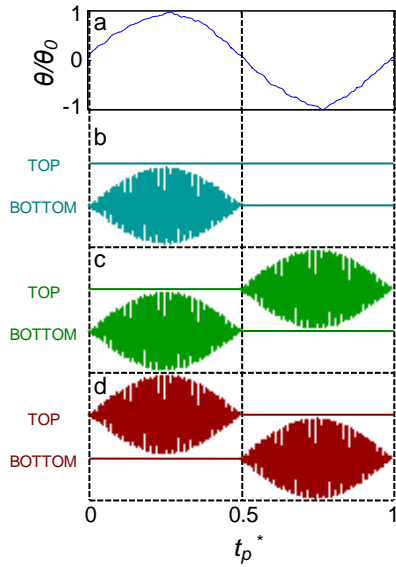


Figure III.13 Dynamic pitching angle of SMA-induced model oscillation (a), and the actuation waveforms of the top and bottom jet for half-cancellation (b), full-cancellation (c), and full-amplification (d) of the dynamic lift force.

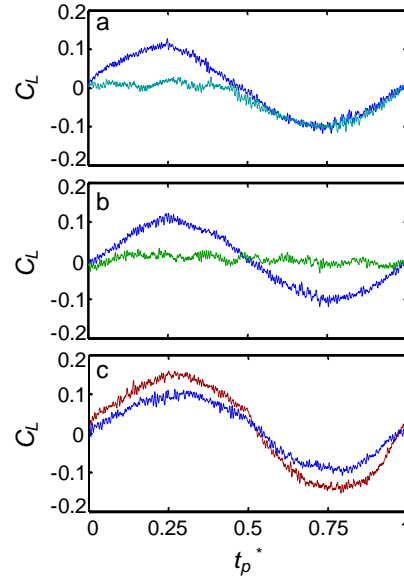


Figure III.14 Measured relative dynamic lift coefficient for the half-cancellation (a), full-cancellation (b), and full-amplification (c) control depicted in Fig. III.13, with the non-actuated lift coefficient shown in blue with a pitching amplitude of $\theta = \theta_0$ at $k = 0.013$ and a max $C_\mu = 2 \cdot 10^{-3}$ for cancellation and $3 \cdot 10^{-3}$ for amplification.

operation of the top jet for $0.5 < t_p^* < 1$ with $C_\mu = 2 \cdot 10^{-3}$, and aims to keep the lift force approximately constant for the entire dynamic cycle. The last flow control function (Figure III.13d) is designed for amplification of the lift force induced by the model oscillations. This function is designed by activating the jets with sinusoidal modulation that is 180° out of phase with function used for cancellation.

The resulting dynamic lift force measurements under these three control strategies are shown in Figure III.14. The initial periodic change in the lift force due to the model oscillations (blue) is shown in each of the plots for reference. When half-cancellation is applied (Figure III.13b), the resulting change in the lift force becomes completely suppressed for half of the model oscillation cycle, while the remaining half of the cycle remains unchanged (Figure III.14a). As the cancellation is extended to full cycle (Figure III.13c), the lift force remains unchanged for the full cycle of the model oscillation (Figure III.14b), completely suppressing the motion-induced force. Finally, when the control is reversed in order to enhance the flow-induced effect (Figure III.13d), there is about 45% increase in the amplitude of the lift oscillations (Figure III.14c), in line with the motion-induced force. This result also agrees well with the increase in lift force slope observed with step modulation (Figure III.10), which yielded an enhancement of 43%. It should be noted that when the jets are set to cancel the lift force induced by the model pitch, they can be operated at approximately two thirds of the saturation momentum coefficient. This finding that the jet-induced force is enhanced when cancelling the lift induced by pitch oscillations is consistent with the flow control results from static variation of the pitch angle (Figure III.8): the top and bottom jets have the most effect when each is operated opposite the pitch direction. Therefore, the amplification effect requires higher C_μ than cancellation for the

same magnitude of an effect, and C_μ need to be actively adjusted to obtain similar amplification and cancellation effects.

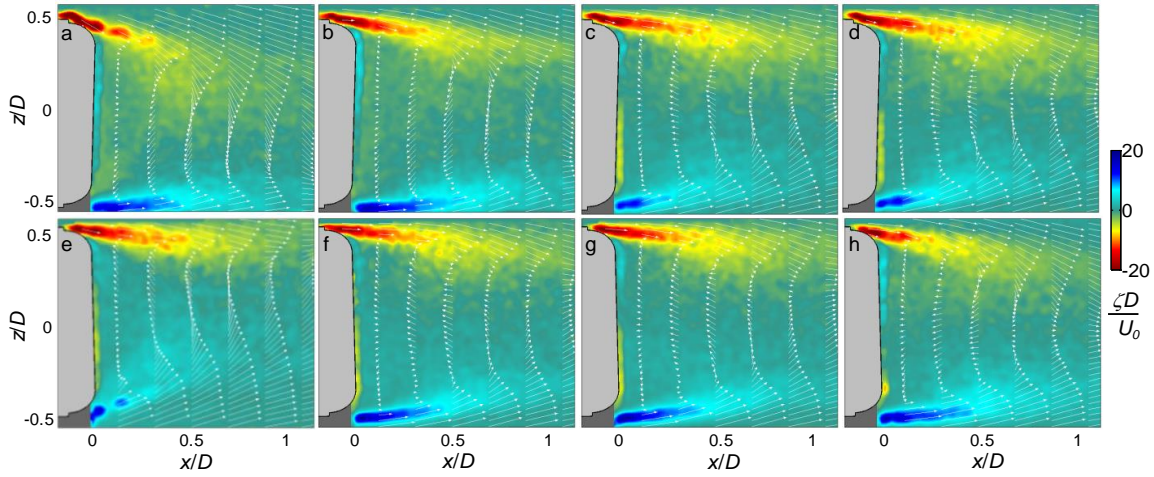


Figure III.15 Raster plots of the phase-averaged vorticity field with overlaid equidistant velocity vectors for $\theta = \pm\theta_0$ pitch dynamics at a phase $t_p^* = 0.25$ (a–d) and 0.75 (e–h), for full-amplification (a, e), non-actuated (b, f), half-cancellation (c, g), and full-cancellation (d, h), as schematically depicted in Fig. III.13.

Examples of the instantaneous wake flow fields under each of the three control programs of Figure III.13 are shown in Figure III.15. The PIV measurements are obtained phase-locked to the model oscillation cycle at 12 instances during the oscillation cycle starting at $t_p^* = 0$ in increments of $t_p^* = 1/12$. The phase-averaged velocity profiles are overlaid on raster plots of the phase-averaged vorticity in Figure III.15 for $t_p^* = 0.25$ (Figures III.15a–d) and 0.75 (Figures III.15e–h), i.e., at the apex of pitch up and pitch down during the oscillatory motion. The corresponding flow fields are presented for the lift force amplification actuation (Figures III.15a,e), baseline (Figures III.15b,f), half-cancellation (Figures III.15c,g) and full-cancellation (Figures III.15d,h) schemes. As seen in Figure III.14, at the pitch up apex deflection ($t_p^* = 0.25$), augmentation induces enhancement of the pitch-induced lift, while both half and full cancellation completely suppresses the lift force. The augmented pitch-induced lift force is realized by enhanced vectoring of the outer flow (Figure III.15a) and thereby increasing wake asymmetry. Both the half and full cancellations (Figures III.15c,d) force the otherwise asymmetric wake into a nearly symmetric flow field (in the measured plane), thereby cancelling the aerodynamic lift force, which was induced due to the wake asymmetry at a nonzero pitch angle. At the apex pitch down phase ($t_p^* = 0.75$), half-cancellation is inactive and does not alter the dynamic lift. Therefore, the baseline (Figure III.15f) and half-cancellation (Figure III.15g) flow fields do not differ in this case. Similar to the peak augmentation of the lift at $t_p^* = 0.25$, the maximum lift augmentation occurs at $t_p^* = 0.75$ as well, but with reversed sense. Therefore, the wake topology at these two phases is inverted about the centerline (cf. Figure III.15a and III.15e). Finally, full-cancellation again suppresses a change in lift, which correlates with the forced symmetry of the wake at this phase (Figure III.15h).

III.2 Free Yawing Axisymmetric Body

After the effectiveness of the proposed flow control approach was assessed on a static and quasi-steady dynamic model (§III.1), the same synthetic jet flow control approach is utilized on a nominally 'free' yawing axisymmetric model to induce localized flow attachment over the body's aft end and thereby alter the dynamic model orientation in a single degree of freedom. The model is supported by a vertical thin steel wire that passes through the model that undergoes natural oscillatory response to the oncoming flow. Hybrid fluidic actuation is effected using two independently driven aft-facing jet actuators that emanate from narrow, azimuthally-segmented slots, centered symmetrically on the opposite ends of the yawing plane, and placed on a circular tail end that extends into a Coanda surface. The body motion response is measured using a laser vibrometer, and the aft coupled body/flow dynamics is characterized using planar PIV. Continuous actuation schemes, independent of model motion, and the respective aerodynamic responses are investigated with 'open loop' fluidic control. In addition, a PID controller is developed to effect 'closed loop' fluidic control with optimally timed synthetic jet operation dependent on model motion.

III.2.1 Free Yawing Platform: Experimental Setup and Procedures

The investigation of yaw control of a single-degree-of-freedom axisymmetric body is conducted in the open-return wind tunnel at Georgia Tech having a test section that measures 91 cm on the side, with a test section speed, U_0 , of up to 40 m/s. The geometry of the wind tunnel model is the same as in the previous studies of the constrained-body configurations (§II). Although the present model is also equipped with the azimuthal array of four independently-driven synthetic jet actuators that are equally distributed along the perimeter of the tail section, the aerodynamic control moments on the model are generated using the two actuators within the plane of the model yawing motion. Both the jets are identical to those already described in detail in §II. The entire model is hollow and designed to have minimum weight, consisting of a nose and a body piece that are held together with screws. A through hole is placed in the nose piece to allow mounting at a fixed location.

All of the components used to mount this axisymmetric model in the wind tunnel are shown in Figure III.16. The steel support wire, $D_s = 1$ mm, is selected to be thin enough to reduce the drag coefficient and decouple its vortex shedding from the model, while thick enough to minimize translational and rotational vibrations. The wire-mounting mechanism consists of two bearings, and a vented screw that is secured to a shaft connector (Figure III.16a). The wire is held in place with the shaft connector, and is tightened by extending both vented screws from the tunnel wall. The model nose has two through holes that pass the support wire and the model is secured in place with two integrated shaft connectors from the inside. This yawing axis is chosen to be $x = 0.015c$ upstream of the

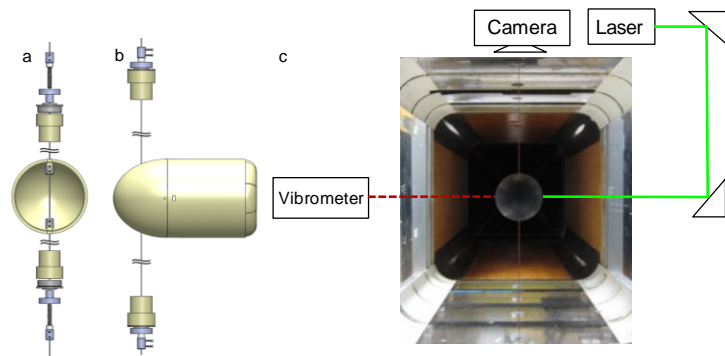


Figure III.16 Unassembled (a) and assembled (b) $D = 90$ mm axisymmetric CAD model and mounting mechanism, and upstream view of the model mounted in the tunnel (c).

The model nose has two through holes that pass the support wire and the model is secured in place with two integrated shaft connectors from the inside. This yawing axis is chosen to be $x = 0.015c$ upstream of the

center of pressure, such that the model is semi-stable. The rest of the model body containing the synthetic jet actuators is secured to the nose (Figure III.16b). The electrical connection for the actuators is enabled by means of additional thin high voltage wires weaved along the support wire and through the tunnel walls, while the support wire provides the electrical ground. The experimental model supported inside of the test section is shown in Figure III.16c.

Measurement of the model angle is acquired by the means of a laser vibrometer sensor mounted normal to the side wall of the test section at a fixed distance L_0 downstream of the model mounting wire. The vibrometer measures the velocity of the surface normal to the laser as an analog signal, and uses a built in low pass integrator to create a second analog signal of the position of the surface. Two surface positions and velocities are needed for a transformation into the model angular position and velocity, so a fixed mounting axis is assumed. The angle, θ , is then extracted from the laser vibrometer measured signal, distance L_0 , and the model diameter, D . The wake is characterized in the model central yawing plane by the PIV measurements. A horizontal PIV laser sheet is steered from the opposite tunnel side as the vibrometer, where the model blocks the laser light from affecting the vibrometer measurements. The PIV camera is mounted on top of the test section, having a capability for traversing in both the streamwise and cross-stream directions.

III.2.2 Baseline Response of the Free Yawing Platform

A primary objective of the present work is to assess the efficacy of synthetic jet flow control in the presence of a dynamically-changing aerodynamic environment. In order to characterize this efficacy, the baseline flow is first characterized in more detail. The model's response is constrained by the mounting mechanism described in §III.2.1 to respond only in one degree of freedom (yaw), where every

care was taken to minimize yaw friction. The mounted model is semi-stable: initial perturbations cause the model to oscillate when the model is exposed to flow. The self-excited oscillations are attributed to the lag between the model's dynamic wake response and its instantaneous orientations. An illustration for such a model oscillation is shown in Figure III.17 at $U_0 = 20$ m/s. Figure III.17a shows a time trace of the model angular position normalized by convective time scales ($\tau_{conv} = c/U_0 = 8.25$ ms), while the corresponding power spectrum is shown in Figure III.17b. The power spectrum was based on twenty cycles of the baseline motion which yielded a frequency resolution of $f_{res} = 0.08$ Hz, and shows a characteristic frequency peak at $f_c \approx 1.7$ Hz, along with its higher harmonics. The value of f_c , as well as the RMS amplitude of oscillation, θ_{RMS} , varies with U_0 and the variation of f_c with U_0 which has a strong linear effect. It should be noted, however, that f_c is more than an order of magnitude lower than the natural shedding frequency, f_s , from the axisymmetric body under the present conditions. The complete cycle RMS of the angular oscillations for ≈ 100 s (rounded down to an integer number of oscillation

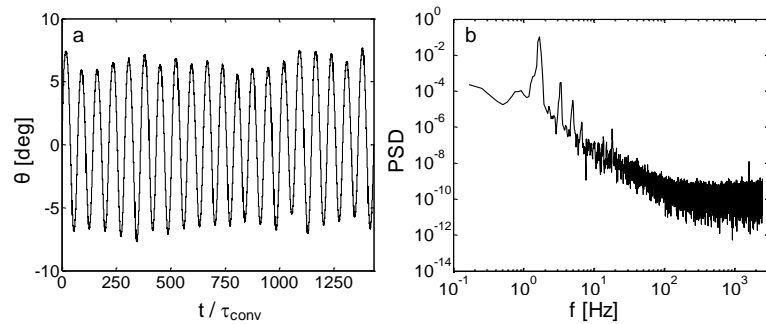


Figure III.17: A time-trace of the baseline model oscillation ($U_0 = 20$ m/s) measured by the laser vibrometer (a) and the corresponding power spectra (b) of displacement fluctuations.

periods from the start time), shows proportionality to U_0 between 14 m/s and 36 m/s, with a deviation in slope for very high and very low U_0 . It is noted that the RMS angle exhibits a weak saturation effect with higher U_0 .

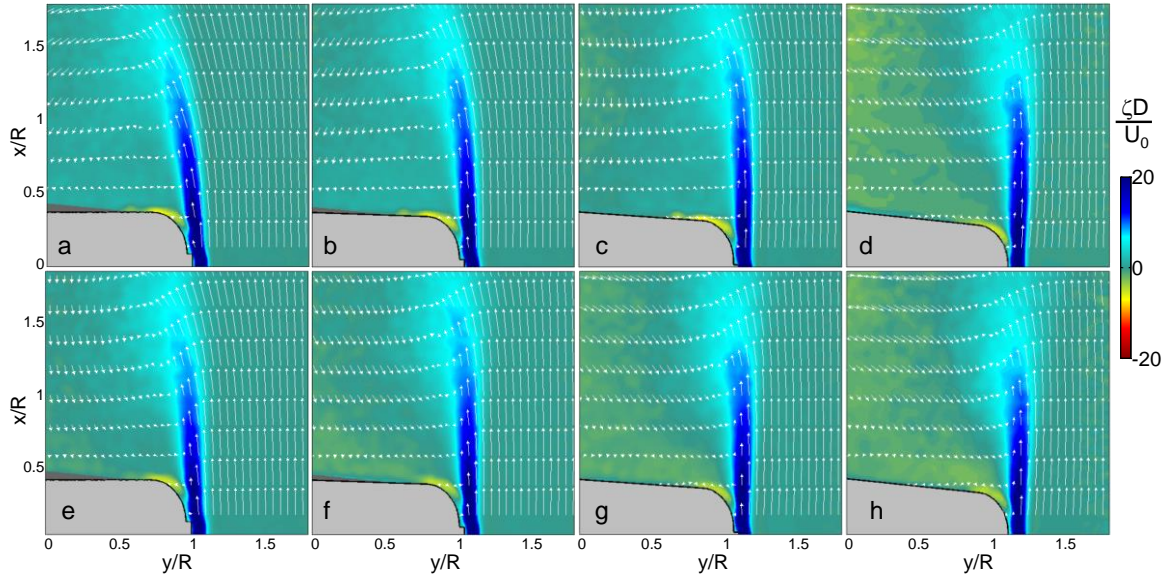


Figure III.18: Raster plots of the in-plane vorticity, ζ , with overlaid velocity field of the baseline flow ($U_0 = 20 \text{ m/s}$) averaged at model's deflections $\theta = 0^\circ$ (a,e), -2° (b,f), -4° (c,g), and -6° (d,h), with negative (a-d) and positive (e-h) angular velocities, ω .

A series of PIV measurements was taken conditionally averaged relative to the baseline oscillation cycle of the model. For each of the phases of that cycle, 170 image pairs are taken and averaged, with triggering off the vibrometer-measured model orientations. Figure III.18 presents such phase-averaged wake flow fields for one half of the cycle overlaid upon contours of the in-plane vorticity, ζ . The angular convention utilized is that the yawing angle and angular velocity, θ and ω , are positive in the counter clockwise direction. The phases presented are $\theta = 0^\circ$, -2° , -4° , and -6° , shown with negative angular velocity, ω , in Figure III.18a-d, and positive ω in Figure III.18e-h, with a $\theta_{RMS} \approx 5^\circ$. It is interesting to note that the cross-stream velocity of particles in the wake, V_w , lag compared to ω . In Figure III.18a, V_w is slightly positive (with a positive convention to the left) when ω is heavily negative, while, in Figure III.18d, V_w is strongly negative when ω is small, and, in Figure III.18e, V_w is slightly negative when ω is strongly positive. This suggests that the reaction force the wake effects on the model is out of phase with the position of the model, and is in accord with assumption that the initial baseline oscillation is caused by aerodynamic instability due to such a phase lag. Another interesting note is that ζ in the shear layer depends primarily on θ , while depending very weakly on ω (compare Figure III.18a-d to Figure III.18e-h).

III.2.2 Free Yawing Platform Response to Continuous Actuation

There are two flow control schemes that are utilized in the present work, the first being a continuous actuation of jets regardless of the model dynamic position in the cycle, and the second being a dynamic activation and termination of the jet actuation with respect to the model's dynamic position. The benefit of continuous, 'open loop' actuation is in simplicity of its implementation for a free-flight body, while the benefit of dynamic actuation is the ability to take

advantage of transient effects of the flow attachment, as well as to adjust control input based on the altered aerodynamic forces and moments coupled to body response due to the initial jet actuation, leading to a more substantial change in the body motion. The off-resonance frequency of operation is chosen such that the maximum expulsion velocity, $U_j \approx 25$ m/s, is obtained for each synthetic jet, yielding a jet cycle period of $\tau_{cycle} = 625$ μ s.

Initially, the effect of continuous actuation is examined at $U_0 = 20$ m/s with two different control schemes: a single-jet and both-jets control, along with the unactuated (baseline) flow. Instantaneous measurements of all three of these scenarios are shown in Figure III.19, with the operational jet momentum coefficient, $C_\mu = (U_j^2 \cdot A_j) / (U_0^2 \cdot \pi D^2) = 0.003$. The data are taken over sampling intervals of 2400 convective time scales where actuation is activated at $t = 600 \tau_{conv}$ and is terminated at $t = 1800 \tau_{conv}$ from the starting point. Figure III.19a shows the instantaneous baseline behavior of the model oscillation, and it is observed that while the frequency is well behaved, the nominal oscillation amplitude is modulated. When the flow is unactuated, the model oscillates around 0° , where it is aligned with the free stream. When the flow is actuated by the right actuator (Figure III.19b), the model rotates counter clockwise around the support axis and oscillates about $\theta = 3.5^\circ$, and a similar effect opposite in direction occurs when the left actuator is activated. It is noted that the left and right actuation effects occur at a faster rate than one oscillation cycle ($\tau_{osc} = .588$ s), where the maximum change from the continuous actuation occurs during the first oscillation cycle. Figure III.19c shows when both jets are activated the model remains centered about zero degrees, similar to the baseline case. However, the oscillation amplitude decreases from 7° to about 2.5° , causing roughly 60% suppression in baseline oscillation amplitude. It is also noteworthy that this decrease with both jets activated does not occur as fast as the offset deflection in the single jet activation case, where the suppression in cycle oscillation amplitude occurs between 5 - $6 \tau_{osc}$.

The single jet open loop control from Figure III.19b is investigated in more detail with the average of 25 data sets in Figure III.20 with phase plots of ω vs. θ in Figures III.20a and b, and the yaw moment, M_y vs. θ , in Figures III.20c and d, where M_y was calculated using a numerical derivative of ω along with the model's rotational inertia. Figures III.20a and c show the transient onset of a single jet from $120 \tau_{conv}$ before to $600 \tau_{conv}$ afterwards, with actuation segment shown in blue. Similarly, Figures III.20b and d show the transient termination of the single jet continuous actuation from $120 \tau_{conv}$ before to $600 \tau_{conv}$ afterwards. Initially, the baseline flow has an elliptical path in ω vs. θ , which is to be expected from quasi-sinusoidal motion, where the angular velocity would lag the position. Figure III.20a shows when actuation is applied, the model vibration becomes deflected to higher angles within one τ_{osc} , but the oscillation occurs with a diminished range of positions and velocities, where the

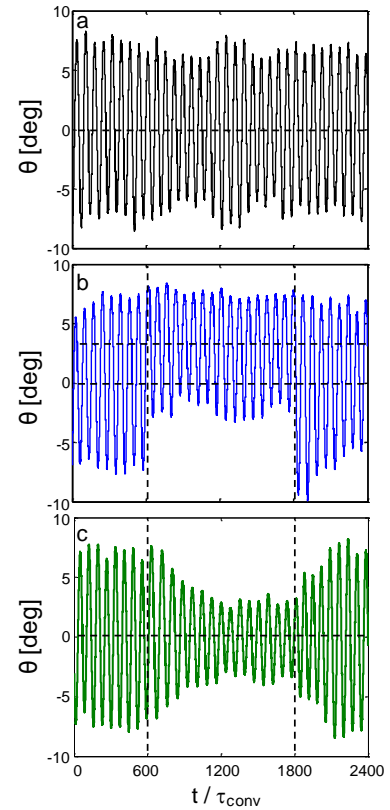


Figure III.19: Instantaneous variation of the model deflection angle, θ , for baseline (a), and actuated flows with single jet (b), and both jets (c) at $U_0 = 20$ m/s and $C_\mu = 0.003$.

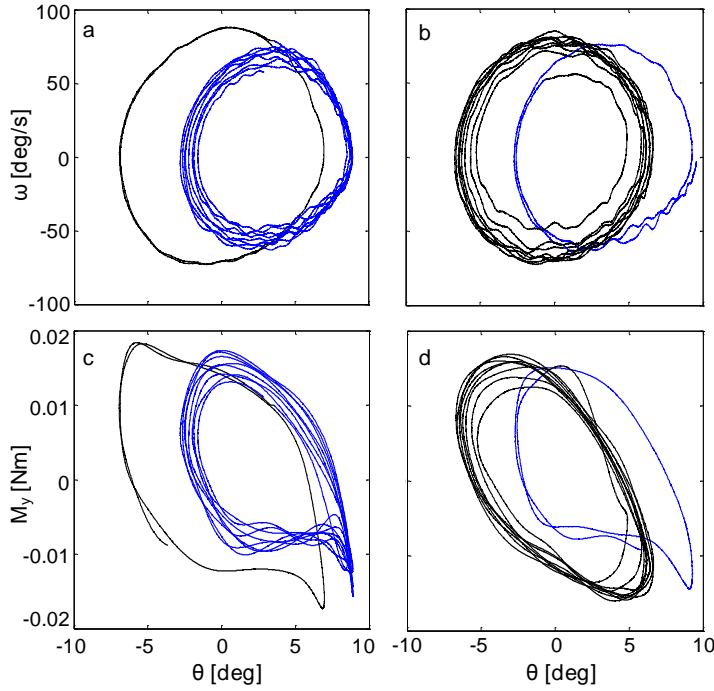


Figure III.20: Phase plot of 25 averages of angular velocity, ω (a,b), and yaw moment, M_y (c,d) for $120\tau_{conv}$ prior to $600\tau_{conv}$ after the transient activation (a,c), and termination (b,d) of single jet continuous actuation at $U_0 = 20$ m/s and $C_{\mu} = 0.003$.

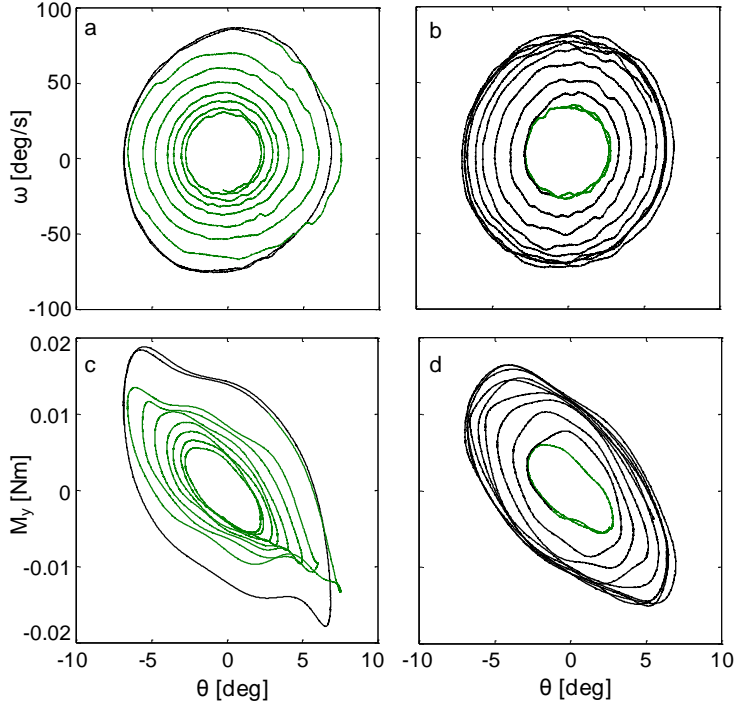


Figure III.21: Phase plot of 25 averages of angular velocity, ω (a,b), and yaw moment, M_y (c,d) for $120\tau_{conv}$ prior to $600\tau_{conv}$ after the transient activation (a,c), and termination (b,d) of both jets continuous actuation at $U_0 = 20$ m/s and $C_{\mu} = 0.003$.

baseline oscillation range was $\pm 7^\circ$ and $\pm 75^\circ/\text{s}$ and it is diminished to $\pm 6^\circ$ and $\pm 60^\circ/\text{s}$ with a new oscillation center of $\theta = 3.5^\circ$. The termination of actuation is shown in Figure III.20b, where the oscillation returns to baseline within one τ_{osc} . There are two notable moment peaks that emerge in the M_y vs. θ plots in Figures III.20c and d that occur after the model has reached its peak angle and reversed direction, which may be attributed to a reaction moment of vortex separation off of the wake of the model where the wake had the tendency to continue in the same direction the model was previously moving. When actuation is applied in Figure III.20c, the range of the yaw moment is also diminished from ± 0.18 Nm to ± 0.16 Nm, similar to the angular velocity. In addition, the vortex shedding peak that occurs at the $-\theta$ disappears while the peak at the $+\theta$ becomes enhanced, which is commensurate with the modified model motion traveling through a small $-\theta$ to a large $+\theta$. The effect of actuation termination on the model moment is shown in Figure III.20d. The model oscillation returns to center with a range similar to the initial baseline motion (compare Figures III.20c and d), with the exception that the baseline peaks have not yet reemerged after $600\tau_{conv}$.

A closer study of the suppression of model vibration in Figure III.19c is shown in Figure III.21 with phase plots analogous to Figure III.20, with ω vs. θ in Figures III.21a and b, and M_y vs. θ

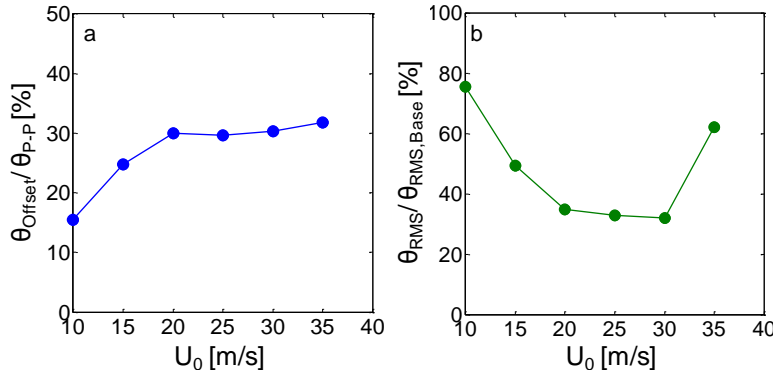


Figure III.22: Induced average deflection percentage with single jet actuation (a), and oscillation suppression percentage with both jets actuation (b) with variable free stream speed, U_0 , at $C_\mu = 0.003$.

with an ellipsoidal path in angular velocity and with moment peaks emerged at the extremes of the motion. Upon the onset of actuation the model vibration slowly reduces over several cycles in Figure III.21a, with the oscillation reducing to a value of $\pm 2.5^\circ$ and $\pm 30^\circ/\text{s}$, while upon termination the model vibration slowly returns to baseline in Figure III.21b. Upon actuation, Figure III.21c, the model moment path diminishes from $\pm 0.18 \text{ Nm}$ to $\pm 0.05 \text{ Nm}$, but its path resembles the initial baseline path including the peaks until a few oscillation cycles have passed, and then finally collapses into an ellipsoidal path. The absence of the moment peaks in the model path with both jets actuation is in agreement with the absence of the peak in the single jet actuation $-\theta$, where the moment peak only occurs when the model moves to a large enough

in Figures III.21c and d. Figures III.21a and c show the transient onset of both jets from $120\tau_{\text{conv}}$ before to $600\tau_{\text{conv}}$ afterwards, while Figures III.21b and d show the transient termination of both jets from $120\tau_{\text{conv}}$ before to $600\tau_{\text{conv}}$ afterwards, with actuation segment shown in green. The baseline flow of Figure III.21, shown in black, is analogous to the baseline flow present in Figure III.20,

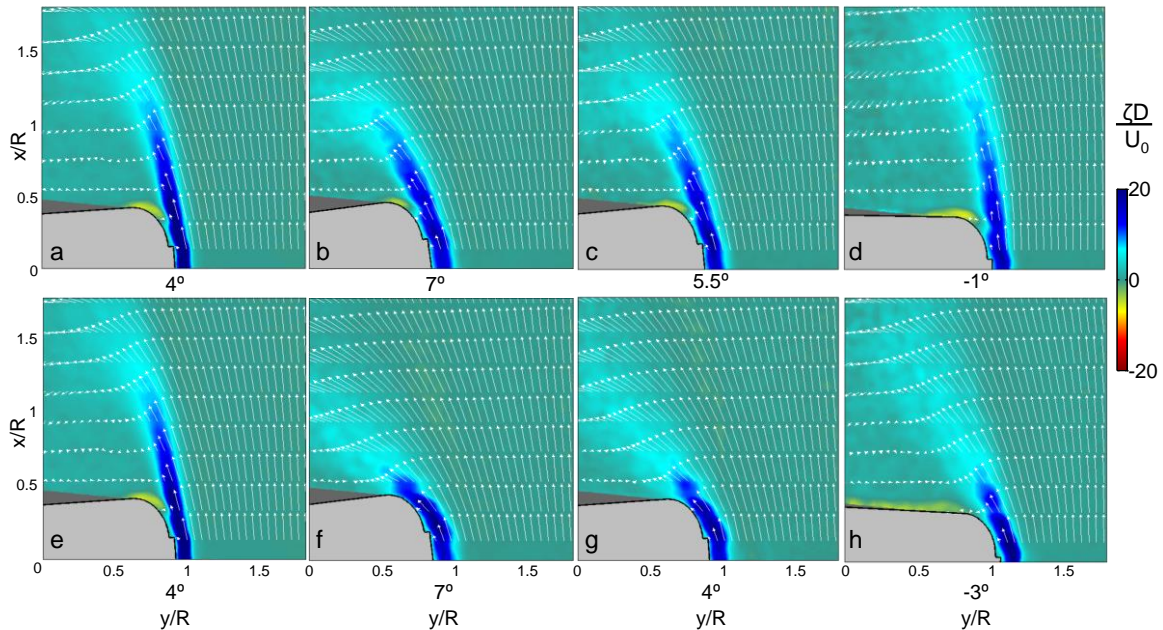


Figure III.23: Raster plots of the in-plane vorticity, ζ , with overlaid velocity field of the baseline flow ($U_0 = 20 \text{ m/s}$) with an initial model deflection of $\theta = 4^\circ$, at $t/\tau_{\text{cycle}} = 0$ (a,e), 125 (b,f), 250 (c,g), and 375 (d,h) after actuation onset for the baseline (a-d), and in-plane jet actuation at $C_\mu = 0.003$ (e-h). The corresponding model deflections are marked below each frame.

angle. This shows that the actuated motion of the model is more stable at smaller excursions, where large aerodynamic moments are induced at a faster rate when the model is yawed further from center. Upon termination, the model returns to the baseline moment curve, but the path remains elliptical, and the peaks have yet to reemerge, even after the passage of $600\tau_{conv}$.

The same study shown in Figures III.20 and III.21 was conducted over a wide range of U_0 and the results are presented in terms of the average steady state deflection of the model with one jet continuously actuated, and the average steady state model oscillation reduction, shown respectively in Figures III.22a and b. In Figure III.22a, the model deflection, θ_{offset} , is normalized by the peak to peak amplitude of the baseline vibration, θ_{p-p} , and this deflection seems to have a saturation effect of 30%, at $U_0 \geq 20$ m/s, with smaller deflection at $U_0 < 20$ m/s. In Figure III.22b, the reduced θ_{RMS} is normalized by θ_{RMS} of the baseline and a similar phenomenon is observed where there is a build up on vibration reduction percentage from 10 to 20 m/s and then saturation from 20 to 30 m/s at 40%, with a decrease in vibration reduction at 35 m/s, presumably caused from the limiting jet momentum at this speed.

Figure III.23 presents the effect of continuous actuation on the time scale of the model oscillation, where the initial $\theta = 4^\circ$, with a positive initial ω . The time steps are chosen to be $125\tau_{cycle}$, $250\tau_{cycle}$, and $375\tau_{cycle}$ (~85 ms, ~169ms, and ~253ms, respectively), and the average θ that the model attains at the corresponding times is shown below each frame. Figures III.23a-d depicts the baseline motion of the model in these time steps. Initially, the model reaches close to its full displacement in Figure III.23b, reverses velocity and starts moving back to center in Figure III.23c, and crosses past zero in Figure III.23d. The effect of continuously actuating the flow for this time duration is shown in Figure III.23e-h, where the model position is initially unchanged relative to the baseline (Figure III.23e) at the onset of actuation. Once the control jet is activated, comparison between Figures III.23b-d to 9f-h shows the wake being vectored towards the model, causing a reaction moment towards negative θ . Initially the model position is least effected in the first time step, and most effected in the final time step, where the effect of the wake vectoring becomes stronger when the jet is inclined into the direction of flow, in agreement with previous shown in §III.1.3.

III.2.3 Effects of Transitory Actuation on the Free Yawing Platform

Before investigating the body-coupled dynamics of activation and termination of the jet control, an investigation of the transient activation of the synthetic jets is conducted to analyze the mechanisms of the localized flow vectoring and attachment on a free moving body of revolution. The analogous comparison of fluidic flow attachment to a *fully constrained* body of revolution was investigated by Rinehart et al. (2003, 2011), and is used for comparison. Two cases of interest are presented with the body (and synthetic jet orifice) declined away from free stream, $\theta = 3^\circ$ (Figure III.24), and inclined into free stream, $\theta = -3^\circ$ (Figure III.25), both with ω such that the model is moving away from center. Both of these cases are characterized with the mean phase-locked vector fields when the initial model angular velocities are oriented away from center. Both figures capture the very onset of the actuation, which is represented by six time steps after the actuation onset, at $t/\tau_{cycle} = 0, 4, 8, 12, 16$, and 20 .

Figure III.24a shows the baseline flow state at the onset of actuation: dominant vorticity is concentrated in the separating boundary layer coupled to the evolving shear layer that bounds the model wake. The flow clearly separates off the short backward-facing step above the jet orifice, and a strong signature of the opposing flow along the model surface is marked by the opposite-sense

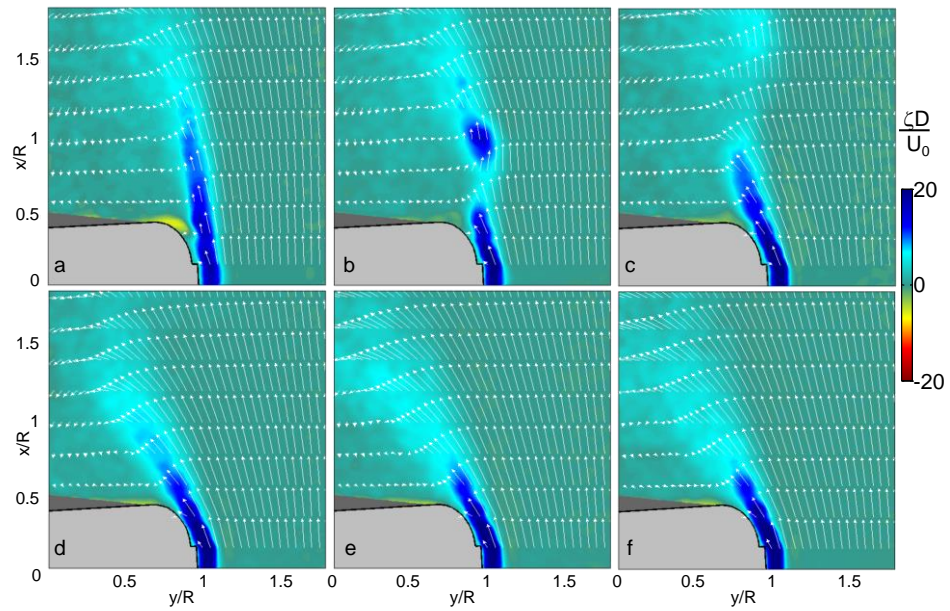


Figure III.24: Raster plots of the in-plane vorticity, ζ , with overlaid velocity field of the transient onset of synthetic jet actuation ($U_0 = 20$ m/s and $C_{\mu} = 0.003$) at initial model's deflection $\theta = 3^\circ$, with positive ω , phase locked at $t/\tau_{\text{cycle}} = 0$ (a), 4 (b), 8 (c), 12 (d), 16 (e), and 20 (f).

vorticity. Figure III.24b shows the flow captured at a moment when four jet-actuation cycles are completed. The large starting vortex is fully formed downstream from the body, as it entrains the outer flow and the wake grows in size. At the same time, under the action of the small-scale jet vortices (unresolved in this view), the flow immediately near the body surface is vectored along the Coanda surface that extends downstream from the jet orifice. At the next instant in time (Figure III.24c), the starting vortex is already shed into the wake, which disconnects the shear layer vorticity sheet. The re-growing shear layer curls into the wake, and the outer flow begins to vector into the wake not only along the model surface (small-scale effect), but also along the trail of the starting vortex. By the full twelve actuation cycles (Figure III.24d), a clear vectored shear layer is formed, which is also accompanied by its widening, i.e., an increase in its characteristic scale from Figure III.24c. After 16 actuation cycles, the wake is fully vectored (Figure III.24e), and only minor differences in the wake structure can be noted over a long time span (compare Figures III.24e and f). The overall time scale on which the full actuation effect is established is in good agreement with previous work on the constrained (§III.1.2), where the full vectoring effect was found to be established after about one convective time scale. The present work on the unconstrained model indicates somewhat longer time scale, but still less than one and a half of the convective time scale ($20\tau_{\text{cycle}} \approx 1.3\tau_{\text{conv}}$).

Figure III.25 shows the analogous flow evolution to that of Figure III.24, with a mirroring of θ around the centerline, and an opposite sense of ω . The development of the flow vectoring occurs in a similar fashion to that of Figure III.24, with some important differences. First, in Figure III.25a the shear layer is initially 'stronger', extending to a

larger downstream location (compare Figure III.24a to III.25a), where the initial vorticity layer size is dependent on θ , and weakly on ω , as shown previously in Figure III.18. Secondly, the growth and detachment of the starting vortex, shown in Figure III.25b and III.25c, is larger when the backward facing step is inclined into the free stream, where the characteristic scale of this starting vortex is similar to the scale of the initial baseline shear layer. This result is in accord with the findings in the case of a stationary body that the change in force relative to the baseline state by the control jet is greater when the model is inclined into the free (§III.1.3). Similar to the deflection towards the wake (Figure III.24), it is seen that the full vectoring effect is attained after about sixteen actuation cycles (Figure III.25e), and the somewhat weaker vectoring observed in Figure III.25f is attributed to the continuing model deflection into the free stream from sixteen to twenty actuation periods between Figures III.25e and f.

As the analysis of Figures III.24 and III.25 indicates significance of a *combined* effect of both the small-scale actuation vortices and a large-scale starting vortex, further insight into their relative

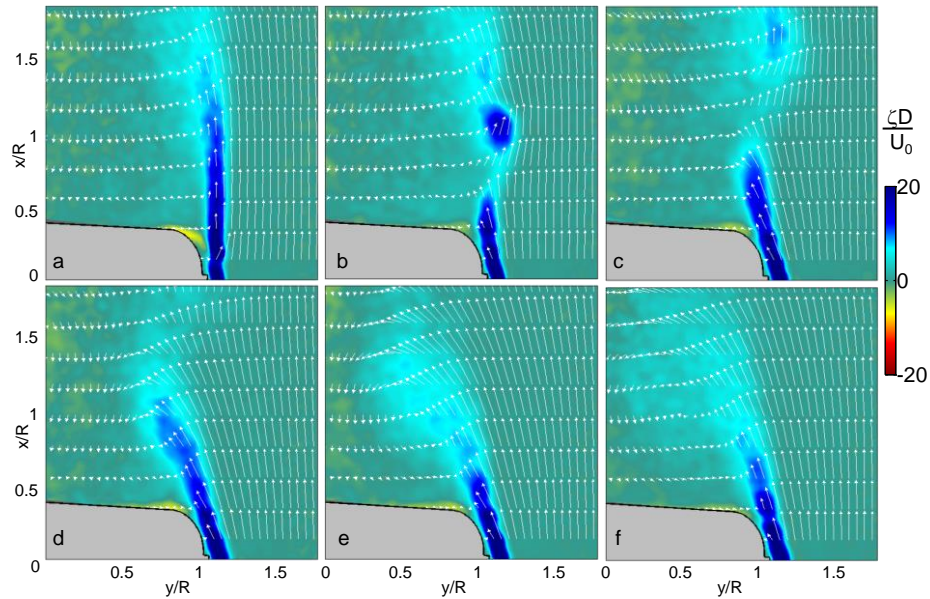


Figure III.25: Raster plots of the in-plane vorticity, ζ , with overlaid velocity field of the transient onset of synthetic jet actuation ($U_0 = 20$ m/s and $C_\mu = 0.003$) at initial model's deflection $\theta = -3^\circ$, with negative ω , phase locked at $t/\tau_{\text{cycle}} = 0$ (a), 4 (b), 8 (c), 12 (d), 16 (e), and 20 (f).

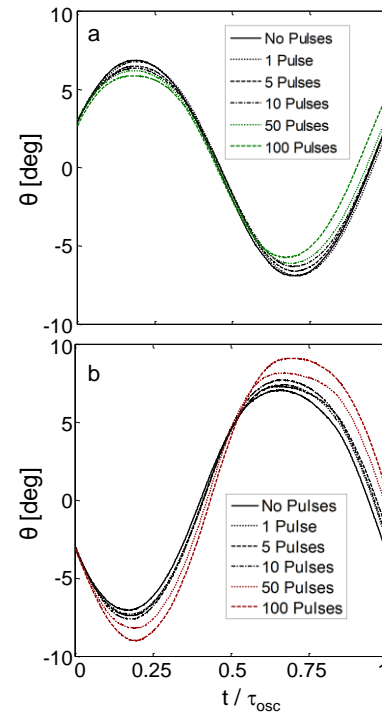


Figure III.26: Phase-averaged transient response of the model position with a width of the burst actuation cycle (number of actuation periods) for initial $\theta = 3^\circ$ (a) and -3° (b), at $U_0 = 20$ m/s and $C_\mu = 0.003$.

significance is sought by activation of packets of high-frequency actuation cycles, each of τ_{cycle} period, in a burst mode. Each of such packets of actuation is inherently associated with a single large-scale starting vortex. This study utilizes the same two model states investigated in Figures III.24 and III.25, with initial orientations of $\theta = 3^\circ$, and positive ω shown in Figure 12a, and $\theta = -3^\circ$, and negative ω shown in Figure III.26b. As the model assumes each of these orientations during its natural oscillations, the burst actuation pattern is applied that consists of 1, 5, 10, 50, or 100 actuation cycles. The model's response to these actuation patterns is recorded by the vibrometer, and model is allowed afterwards to return to its baseline state. This sequence is repeated fifty times for each of the burst cycles, and the averaged model trajectories are shown in Figure III.26, along with the baseline model trajectory over a single oscillation period, beginning at the onset of actuation ($t = 0$). In both Figures III.26a and III.26b, the effect of actuation on the baseline model motion appears to monotonically increase with the number of pulses, right from the onset of actuation. In Figure III.26a, the initial orientation of the model causes the jet pulses to suppress the model oscillation, and as the model oscillation is suppressed, the period of the model oscillation is also decreased monotonically with the extent of the burst duration. It should be noted that there is virtually no effect of the single-pulse burst, when a single starting vortex is accompanied by only a single small-scale vortex, and this finding stresses the importance of the small-scale actuation on the external flow vectoring. As the model orientation is mirrored in Figure III.26b, the actuation effectively amplifies the model natural oscillations. Similar to the

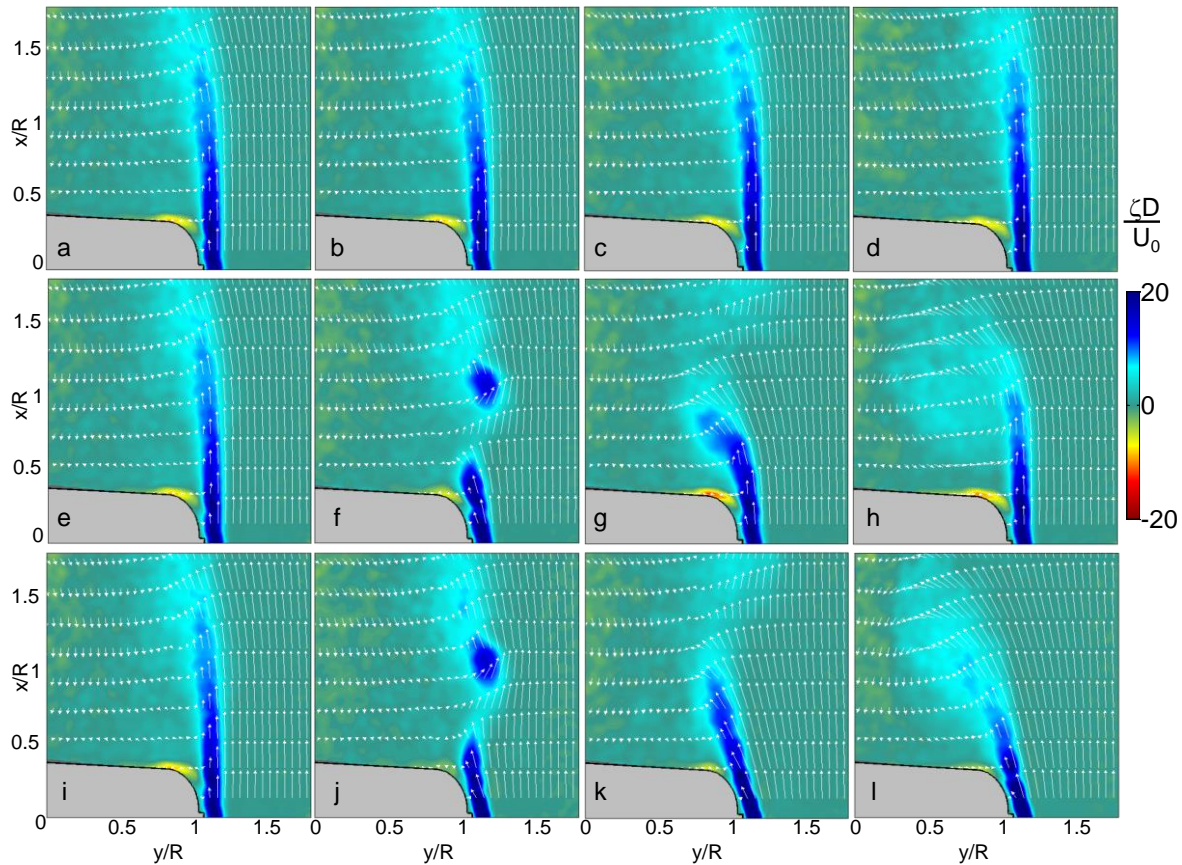


Figure III.27: Raster plots of the in-plane vorticity, ζ , with overlaid velocity field of the transient onset of synthetic jet control ($U_0 = 20$ m/s and $C_\mu = 0.003$) at model's deflection $\theta = -3^\circ$, phase locked at $t/\tau_{cycle} = 0$ (a,e,i), 5 (b,f,j), 10 (c,g,k), and 15 (d,h,l), for the baseline flow (a-d), a single-pulse (e-h), and continuous (i-l) control.

trends seen in Figure III.26a, amplification in model displacement increases with the burst period, which also leads to monotonic increase in the oscillation period. Furthermore, a sole existence of the starting vortex is not sufficient to impose alterations to the model trajectory, but it is successive train of small-scale vortices that plays a dominant role in the induced effect.

The effect of the number of actuation pulses on the wake development is further characterized by the phase-averaged PIV of 170 individual measurements, which are shown in Figure III.27. The initial orientation of the model is the same as Figure III.26b, with $\theta = -3^\circ$, and negative ω , and this initial orientation is shown in Figures III.27a,e, and i. The phase-averaged measurements are taken at $t/\tau_{cycle} = 0, 5, 10$, and 15 from the initial orientation. Figures III.27a-d show the unactuated wake variation due to the model motion over fifteen actuation cycles, which is only about 0.5° in model deflection. Such a small model deflection results in negligible difference among the flow fields in Figures III.27a-d. The flow fields under the single-cycle burst actuation are shown in Figures III.27e-h at equivalent time instances. Note that the corresponding model trajectory is shown in Figure III.26b. Clearly, at the onset of actuation (Figure III.27e), the flow field does not differ from the baseline, but after the five actuation periods (Figure III.27f), the large-scale starting vortex is already fully formed and shed. Note that there is no significant vectoring of the flow along Coanda surface at the tail. By the ten actuation periods (Figure III.27g), the recoiling severed shear layer entrains some of the fluid into the wake, further away from the body, while there is no flow vectoring along the body surface. As the time progresses (Figure III.27h), the initial shear layer is re-established back to the baseline, while the large-scale vortex rolls into the wake away from the body. As a consequence, there is no immediate flow vectoring over the body surface at any instant in time. Figures III.27i-l show the flow response to continuous jet actuation, as opposed to the single-period (“pulse”) actuation shown in Figures III.27e-h. It is interesting to note that the global flow field is very similar after five actuation periods (compare Figures III.27j and f): the effect of the large-scale starting vortex should be invariant in these two cases, as expected. However, the major difference can be seen near the body surface: during the continuous actuation, there is a notable flow vectoring along Coanda surface, which is a signature of the near-field vectoring effect. Furthermore, as the shear layer recoils (Figure III.27k), it is associated with a strong outer flow vectoring over Coanda surface, which is absent from the single-period actuation (Figure III.27g). Finally, after the fifteen actuation periods (Figure III.27l) there is the most dramatic difference in the wake alteration when compared with the single-period actuation, as the full wake vectoring is achieved. Therefore, the pre-selected actuation scheme for the closed-loop control approach is set to utilize continuous cycles, where successive actuation cycles are applied continuously, rather than with single-period cycles.

III.2.4 Closed-Loop Control of the Free Yawing Platform

In §III.2.2, the open-loop activation of the synthetic jets is shown to significantly alter the model's yawing angle. However, this open-loop approach does not take advantage of optimal activation duration by individual jets, and it is argued that utilization of a closed-loop control is necessary for an optimal response path. Therefore, the final step of the present study is the development of a closed loop controller to control the model's yawing angle. To illustrate this approach, a PID controller is developed, which utilizes a laser vibrometer as the sensor of the model's angular displacement, θ . The general theory of a PID controller uses the difference in the goal output, θ_G , from the sensor output, θ , as the proportional error (σ_P), and then uses a numerical integral and numerical derivative of σ_P to obtain the integral error (σ_I) and derivative

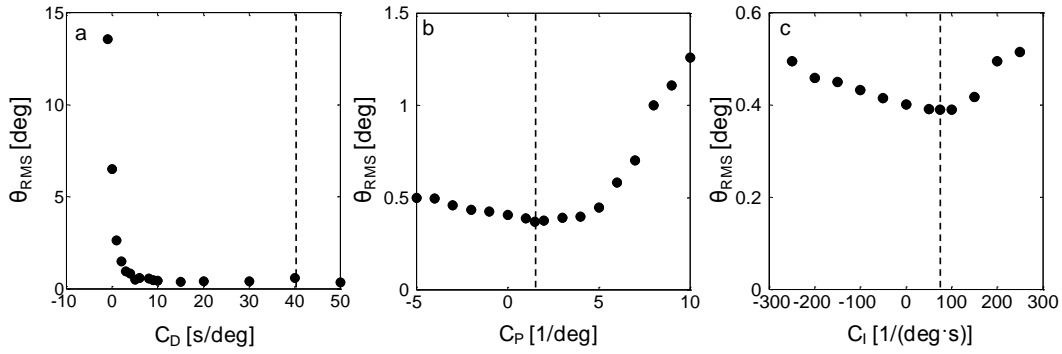


Figure III.29: Determination of C_P , C_I , and C_D ($U_0 = 20$ m/s, maximum $C_\mu = 0.003$) for suppression of model oscillations: varied C_D , $C_I=C_P=0$ (a), varied C_P , $C_D = 40$ s/deg, $C_I = 0$ (b), and varied C_I , $C_D = 40$ s/deg, $C_P = 1.5$ /deg (c). Selected operational parameters are shown by dashed lines.

III.29c. This led to the minimal $\theta_{RMS} = 0.40^\circ$, at $C_I = 75 \frac{1}{\text{deg} \cdot \text{s}}$, which is used as the operational C_I coefficient.

Three control schemes are singled out as the primary investigations of interest: holding the model steady at $\theta = 0^\circ$, holding the model steady at an offset $\theta > 0^\circ$, and amplification of baseline vibrations. The instantaneous implementation of these control schemes are shown in Figure III.30 with a free stream velocity of $U_0 = 20$ m/s during the time span of $600\tau_{conv}$ uncontrolled, $1200\tau_{conv}$ controlled, and $600\tau_{conv}$ uncontrolled. Figure III.30a demonstrates the implementation of the controller with a goal $\theta = 0^\circ$, with the controller onset and termination shown with vertical dotted lines, and the desired zero level is also shown as a dotted line for reference. As mentioned above, $\theta_{RMS} = 0.4^\circ$ about zero when implemented. It is important to note that upon the controller onset, the model response reaches its steady state position on the order of $2\tau_{osc}$, while when terminated, it takes significantly longer to return to its steady state oscillation. As an example of realized offset angle of attack, Figure III.30b shows results of implementation of the controller with a goal angle of $\theta = 2^\circ$, with both 0° and 2° shown as referenced dotted lines. This angle positioning was achieved with right jet modulation alone, and this control scheme takes a longer time period to reach a steady state angle, compared to angle of zero degrees (Figure III.30a). Figure III.30c implements the controller with the coefficients inverted from their optimal values, yielding an amplified response signal of the model vibration, again with zero shown as a reference with a dotted line. Similar to Figure III.30a, this control takes around $2\tau_{osc}$ to reach its controlled state, while needing a significantly longer period of time to return to its free stream vibration, once the control is terminated.

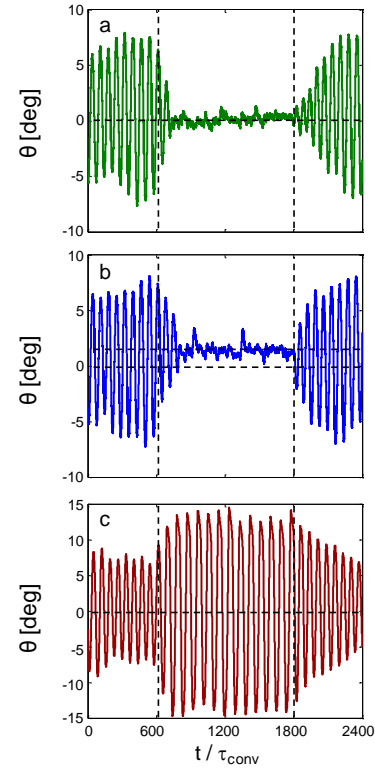


Figure III.30: Time-trace of the model deflection angle for the PID closed-loop control ($U_0 = 20$ m/s and maximum $C_\mu = 0.003$) of $\theta = 0^\circ$ (a) and 2° (b) angle of attack, and amplification of oscillations (c).

The transient response of each control scheme in Figure III.30 is investigated in more detail in Figure III.31. Figures III.31a-c show the instantaneous time traces corresponding to Figures III.30a-c from $120\tau_{conv}$ prior to $360\tau_{conv}$ after onset of control. The controller modulation signals are shown to the right jet in Figures III.31d-f, and to the left jet in Figures III.31g-i. In Figures III.31d and g the jet modulations of amplitude saturate for the first second of activation where the controller is attempting to rapidly compensate from the large differences in desired and measured angle, and settle to rapid minor activations of around 50% of the maximum jet output. Initially, the oscillation is a 1.7 Hz quasi-sinusoidal wave, making the derivative error σ_D a factor of ~ 10 ($2\pi/\tau_{osc}$) times larger than σ_P , which is in turn also ~ 10 times larger than σ_I . The result of this scaling causes the derivative term in the controller to dominate for the first few modulation pulses. This is observed in the first few modulation cycles in Figure III.31d, where the right jet initially activates when there is a negative angular velocity, and in the corresponding Figure III.31g the left jet activates when there is a positive angular velocity. The resulting activation of the synthetic jets leads to a control that primarily opposes the model's angular velocity. When the model response begins to settle, the other terms in the controller play a larger roll and the modulation signal become smaller, more rapid, and less periodic. Figure III.31e is similar to III.31d, with the exception that when the model is being held at an offset angle, the right jet modulation has more initial saturated pulses, and the steady angle modulations are larger in

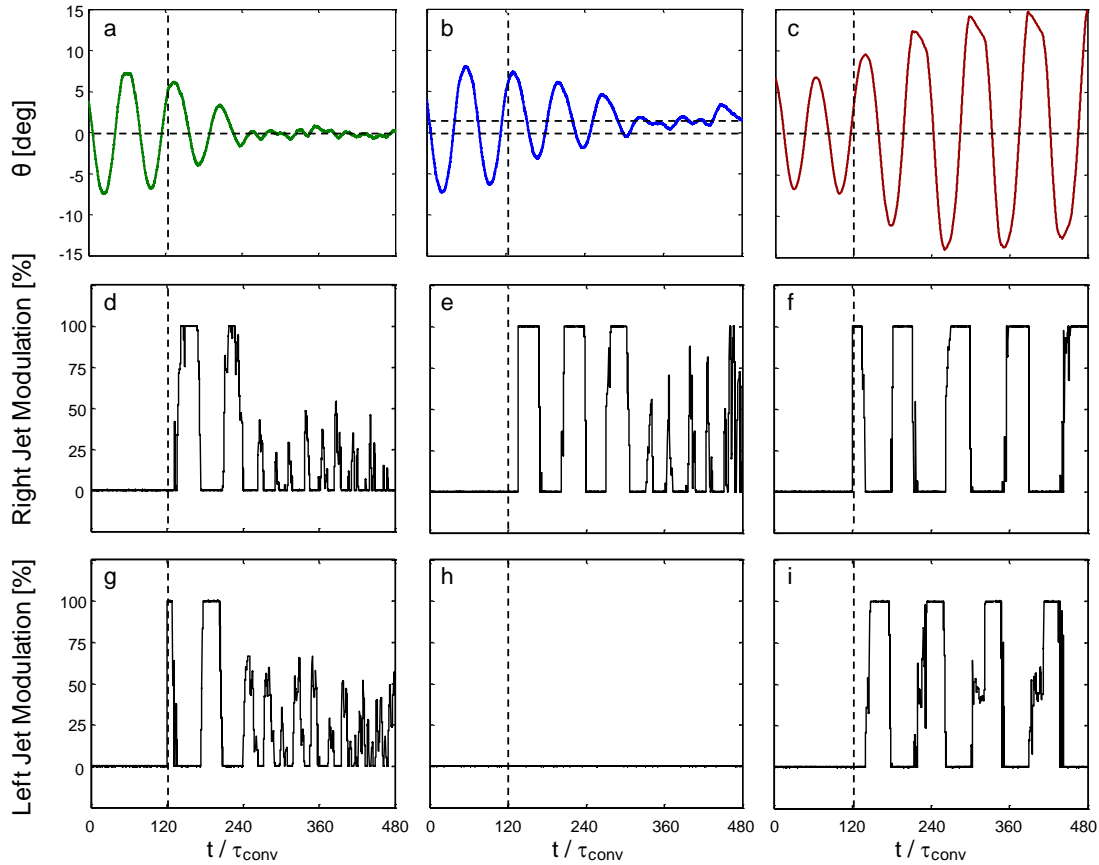


Figure III.31: Model deflection (a,b,c) and the corresponding modulation control signals to the right (d,e,f) and left (g,h,i) jet ($U_0 = 20$ m/s and maximum $C_\mu = 0.003$) for $\theta = 0^\circ$ (a,d,g) and 2° (b,e,h) angle of attack, and amplified oscillation amplitude (c,f,i) PID control schemes, with control onset at $t = 120\tau_{conv}$.

magnitude. In Figures III.31f and i the model response frequency remains around the same magnitude as the model oscillation frequency before the jet activations were triggered, making σ_D dominate for the entire duration of the controlled response. This causes the model to activate the jets primarily to enhance the model's angular velocity, where the jet modulations do not settle and instead continually saturate for the duration of this control.

The transient response of the controller command $\theta = 0^0$, both in activation and termination, is plotted in Figure III.32, with this result being the average of 25 data sets. Similar to Figures III.20 and III.21, the transient response is plotted $120\tau_{conv}$ prior to $600\tau_{conv}$ after the control actuation in Figures III.32a and c, and $120\tau_{conv}$ prior to $600\tau_{conv}$ after the control termination in Figures III.32b and d, with the control actuation shown in green. Figure III.32a shows ω vs. θ , initially forming an ellipsoidal path, where a circular path would represent perfect harmonic motion, and then upon the onset of the jet control, the model forced to $\theta = 0^0$ within $2\tau_{osc}$. The observation that the noise on this final model state is smaller than the fluctuation about the instantaneous suppression (Figure III.32a) is evidence that the induced disturbances in the model with the control activated are pseudo random, and average to zero. When the control is terminated in Figure III.32b, the model returns to the baseline path at a much slower rate compared to control onset, but at approximately the same rate as open loop actuation (Figure III.21b). There is a ringing oscillation present in the center of Figure III.32b, showing that the model becomes unstable in this forced position once the control is terminated. Figures III.32c and d show M_y vs. θ for the same duration of Figure III.32a and b. The onset of the jets in Figure III.32c command the model to reach zero angle of attack, but the aerodynamic force is more unstable then the position, leading to the steady state activation to average to a vertical line on this phase plot. Similar to Figure III.32b, Figure III.32d shows that the termination of the control takes a much larger time period to restore the baseline cycle, where the baseline cycle isn't fully restored even after $600\tau_{conv}$, similar to the open loop control cases in Figures III.19 and III.20.

A similar study of the transient response of the model is presented for the controller command $\theta = 2^0$ in Figure III.33, with the control actuation shown in blue. Figures III.33a and b show the development of ω vs. θ , and Figures III.33c and d show the development of M_y vs. θ . The control onset is shown in Figure III.33a and c, where the model is forced to $\theta = 2^0$, but a longer time

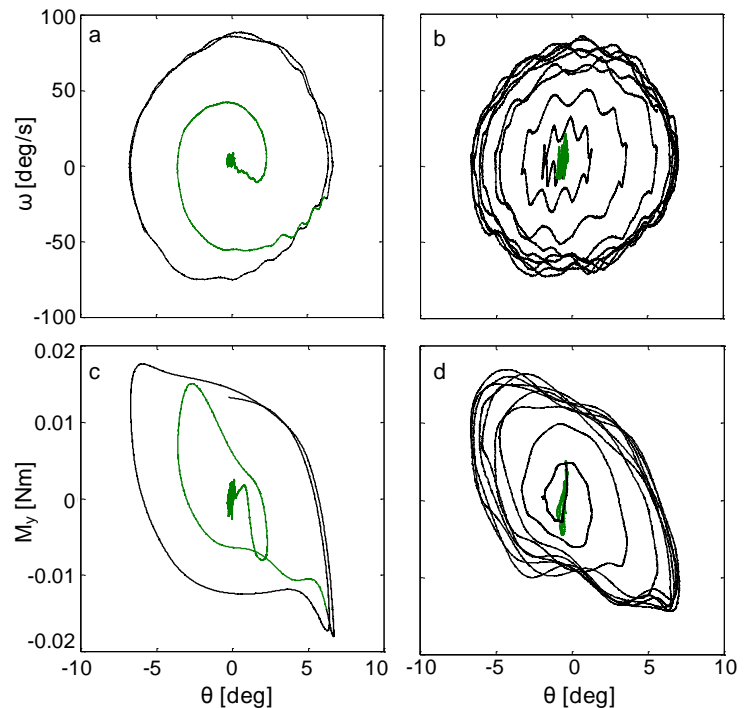


Figure III.32. Phase plot of 25 averages of angular velocity, ω (a,b), and yaw moment, M_y (c,d) for $120\tau_{conv}$ prior to $600\tau_{conv}$ after the transient activation (a,c) and termination (b,d) of the $\theta = 0^0$ PID control for $U_0 = 20$ m/s and maximum $C_\mu = 0.003$.

is needed to achieve this goal ($4\tau_{osc}$) due to the controller utilizing one jet as opposed to both to reach its command goal. It is interesting to note that the moment peaks present in the baseline in Figure III.33c diminish during the application of control, with large peaks still present in the first τ_{osc} , but these peaks diminish as the range of motion becomes smaller, which is in good agreement with Figures III.20 and III.21. When the control is established, the location of the model is less steady than when the controller was holding the model at $\theta = 0^\circ$, causing the established position to have a lot more noise in θ , averaging to an ellipse rather than a line (compare Figures III.32 and III.33). Upon termination of control, in Figures III.33b and d, the average path has a ringing oscillation, which is a similar instability to that observed in Figures III.32b and d, and the termination of the control also requires more than $600\tau_{conv}$ to return to the fully established baseline oscillation.

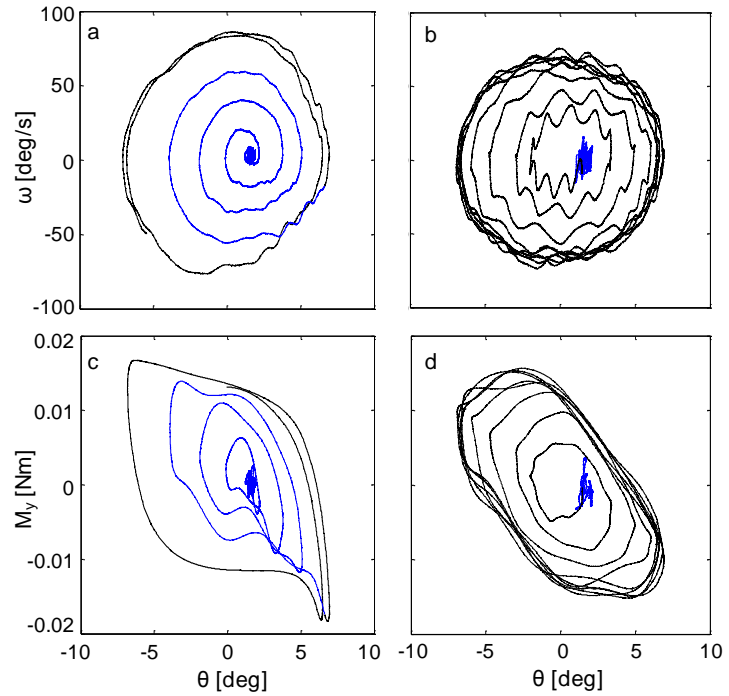


Figure III.33. Phase plot of 25 averages of angular velocity, ω (a,b), and yaw moment, M_y (c,d) for $120\tau_{conv}$ prior to $600\tau_{conv}$ after the transient activation (a,c) and termination (b,d) of the $\theta = 2^\circ$ PID control for $U_0 = 20$ m/s and maximum $C_u = 0.003$.

The amplification closed loop control scheme is investigated in detail in Figure III.34, in an analogous fashion to Figures III.32 and III.33. Upon the presence of actuation in Figures III.34a and c the ellipsoidal path is amplified to a new path with the introduction of angular velocity peaks at the extremes of motion, and the moment peaks become much more pronounced. The increase of prominence of the moment peaks with the larger oscillation amplitude shows that the model path is more unstable than it was initially, deviating further from simple harmonic motion, with sudden large aerodynamic moments introduced at the extremes of motion. This effect shows the same trend as Figure III.21, where an actuation scheme that decreased the oscillation amplitude also diminished these instabilities. The variation of the path once the control is established is significant, showing a similar development of time scale as the open loop control studies investigated in Figures III.20 and III.21. Before the termination of control in Figure III.34d, the path is significantly different than the path observed 5s after the onset of control in Figure III.34c, suggesting that the amplified path is very unstable, and was not fully established in Figure III.34c. Upon termination of the amplification control in Figures III.34b and d, the model returns to the baseline path at a significantly faster rate than the two held-stationary control schemes, which can be observed by the emergence of the moment peaks in Figure III.34d, which were not established in Figures III.32d and III.33d.

The effect of the different controller schemes on the model wake is examined using an ensemble average of 2,000 PIV fields shown with streamwise velocity, U , contours in Figures III.35a-e, and ζ contours in Figures III.35f-j. The biggest average wake disturbance is observed when the controller is set to amplify model's oscillations in Figures III.35a and f, with the minimum and maximum range of the model orientation shown with dashed lines at the bottom left of each figure. In this scenario, most of the wake effects are averaged out, with the key note that remnants of the out-of-picture jet are observed with a negative vorticity region when the model is most yawed clockwise, as well as a positive vorticity region which shows remnants of the largest model position when the angular velocity changes sign.

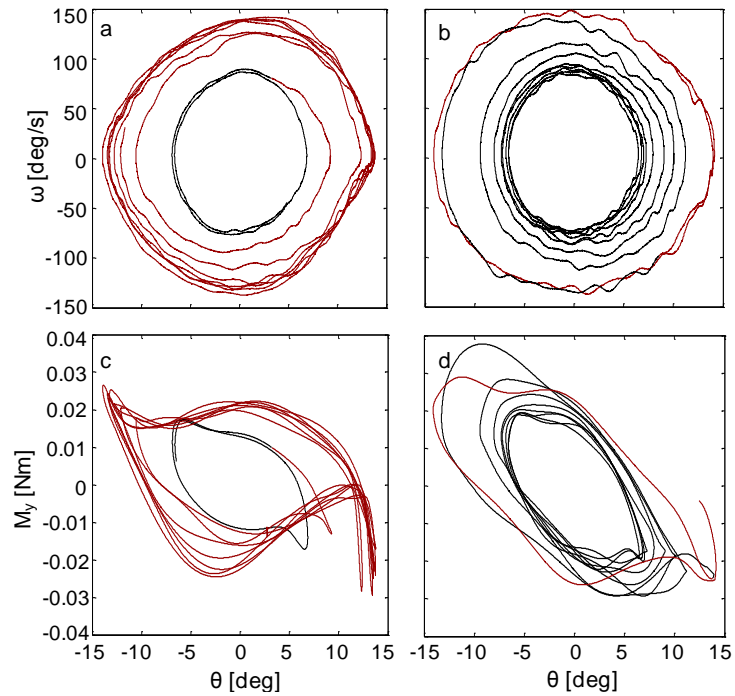


Figure III.34. Phase plot of 25 averages of angular velocity, ω (a,b), and yaw moment, M_y (c,d) for $120\tau_{conv}$ prior to $600\tau_{conv}$ after the transient activation (a,c) and termination (b,d) of the amplification PID control for $U_0 = 20$ m/s and maximum $C_\mu = 0.003$.

Figures III.35b and g again average out a lot of the wake's features but give a visual indication of the vorticity shed when the model changes direction at the extremes of its deflection. Figures III.35c,d, and e show a developed wake when the model is set to be held steady at $\theta = 2^\circ$, 0° , and -2° , respectively, where even though the model position is different, the wake structure of U is predominantly similar. Figures III.35h,i, and j show more clear differences in ζ , where the model being held primarily with the

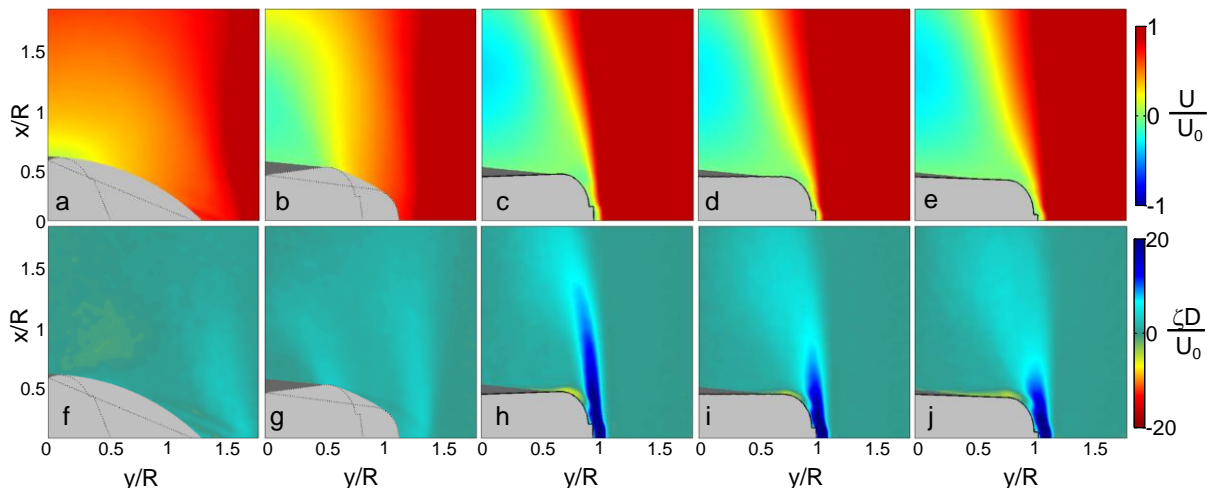


Figure III.35: Contour plots of the time-averaged streamwise velocity, U (a-e), and in-plane vorticity, ζ (f-j), for: amplified control (a,f), baseline (b,g), and $\theta = 2^\circ$ (c,h), 0° (d,i), -2° (e,j) control, for $U_0 = 20$ m/s and maximum $C_\mu = 0.003$.

out of plane jet has the largest area of the largest positive vorticity contour, but has the least spread (Figure III.35h), and the model being held primarily with the in plane jet has the smallest area of the largest positive vorticity with the most spread (Figure III.35j), and the model being held by both jets has an intermediate vorticity contour structure. (Figure III.35k).

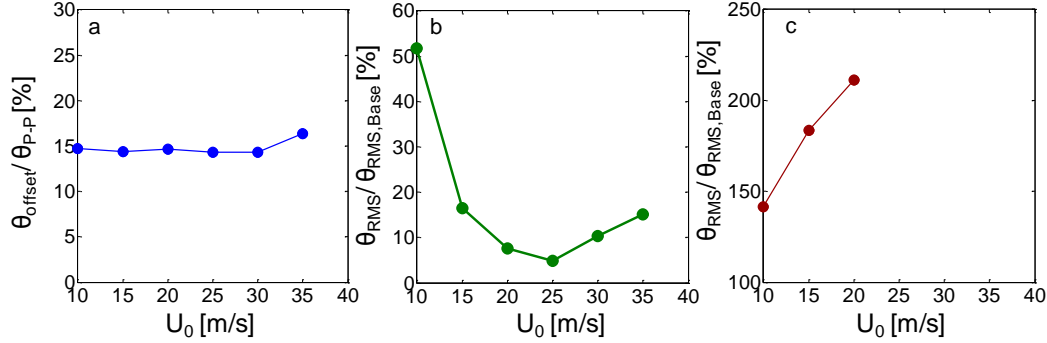


Figure III.36: PID control induced steady deflection (a), oscillation suppression (b), and oscillation amplification (c) percentages with the free stream speed, U_0 , at maximum $C_\mu = 0.003$.

The results of these three schemes of the controller were analyzed at various wind tunnel speeds, and the results are displayed in Figure III.36. Figure III.36a shows the ratio of the maximum steady deflection angle obtained, θ_{Offset} , normalized by the baseline θ_{P-P} , and plotted against U_0 , where this result appears to be almost invariant at the wind tunnel speeds investigated (10-35m/s). As the baseline vibrations increased approximately linear with the wind tunnel speed, the model's steady deflection angle also linearly increased with wind tunnel speed. A reason for this is that the primary force the synthetic jet induces is from vectoring the shear layer, so, as the shear layer becomes faster with U_0 , the induced model force becomes larger as well. Figure III.36b displays the θ_{RMS} of the $\theta = 0^\circ$ control compared to θ_{RMS} of the baseline, plotted against U_0 . When U_0 is relatively low, the jets do not effect enough of a force to counteract the instability force. Also, when U_0 is relatively high, the present C_μ is insufficient to fully vector the wake, which is required to stabilize the model. Therefore, there is a competing control effect, and a maximum reduction of the model oscillations is 95% at $U_0 = 25$ m/s. Figure III.36c displays the θ_{RMS} of the amplification control compared to θ_{RMS} of the baseline, plotted against U_0 . The maximum amplification percentage is shown for $U_0 = 10, 15$, and 20 m/s, where higher U_0 had excited the oscillation angles outside of the vibrometer range ($\sim \pm 15^\circ$), and therefore could not be recorded.

III.3 Aerodynamic Flow Control in 6 DOF Motions

The final study concerns the aerodynamic flow control on the axisymmetric body executing the prescribed, computer-controlled motion on a 6-DOF traversing mechanism. The experiments focus on active fluidic control of the aerodynamic forces and moments of an axisymmetric bluff body platform in time-periodic sinusoidal pitch oscillations at reduced frequencies $0 < k < 0.259$. The platform is wire-mounted on a six degree of freedom traverse where each of the eight support wires is individually controlled by a servo motor with an integrated in-line load cell for feedback control of the platform's motion. The aerodynamic forces and moments on the platform are manipulated by controlled interactions of the same azimuthal array of synthetic jet actuators on its aft segment, utilized in §III.1 and §II.2, with the local cross flow to induce partial (azimuthally-segmented) flow attachment that is coupled with vectoring of its near-wake. The actuation-induced forces and moments can either increase or diminish the corresponding pitch-induced baseline aerodynamic forces and moments. These actuation effects are exploited for open-loop control to suppress or augment the pitch-induced moment over a broad range of oscillation frequencies that are suitable for trajectory stabilization and steering in free-flight.

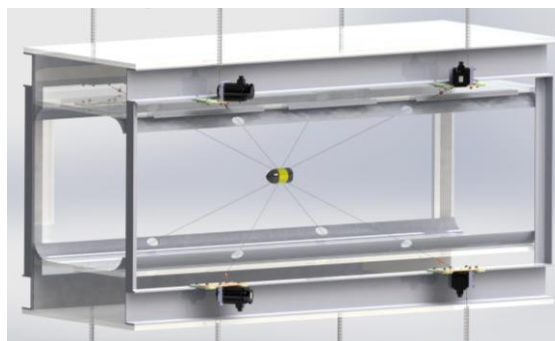


Figure III.37 A schematic diagram of the new dynamic 8-wire support mechanism each utilizing a servo actuator.

III.3.1 Dynamically-Controlled Motion of Wind Tunnel Models

The Eight-Wire Traverse

This system enables the mounting and testing of 3-D (and 2-D) wind tunnel models with minimal support interference either statically or dynamically (Figure III.37). In the dynamic mode, the motion of the model is enabled by time dependent variation of the tension and length of eight support wires (1.2 mm dia.) each connected to a servo actuator (Yaskawa SGMAV-10A, having peak torque of 9.55 N-m at 6,000 RPM peak) to control its length and tension. The wire driving pulley is also attached to an extension spring that provides a preload of 60 N (approximately half the allowed wire tension). This preload enables the model to remain stationary when the system is turned off, and boosts the effective output of the servo actuators by operating in parallel, where the motor response provides the incremental tension required to accelerate the model. The tension in each mounting wire is measured using an inline miniature load cell (Futek FSH0009, 0-110 N) that is used for force feedback. The actuator components are mounted outside the wind tunnel to minimize effects on the flow. It is important to note that the model can be mounted such that it has significant and comparable range in each of the three rotation axes (pitch, yaw, and roll).

On command, the system can synchronously adjust each wire length (while maintaining tension) to rotate the model around three independent axes: roll ($\pm 8^\circ$), pitch ($\pm 15^\circ$), and yaw ($\pm 9^\circ$), and translate independently ± 50 mm in all three (streamwise, lateral, and vertical) directions. In the current design the model can be rotated at up to 6 rad/sec and translated at up to 2 m/sec. The capability to rapidly reposition the model will provide a valuable tool to explore the effects of

motion and orientation on aerodynamic characteristics which is typically limited with conventional adjustable mounts. In addition, the time-dependent tension in each of the wires is simultaneously measured using inline miniature force sensors (Figure 4). The system is designed to handle a variety of models including munitions, small-scale UAVs, parafoils and parachutes, and rotorcraft configurations.

Control Electronics

A computerized control system automatically positions the actuators in response to a string of input commands to move the model through a prescribed, time-dependent trajectory. The system uses a multi-input multi-output (MIMO) state feedback controller to adjust the stroke of each of the electromechanical linear actuators in order to properly compensate for cable stretch. The executed motion is recorded by a Vicon Motion Analysis System (six *Vicon* MX-T40S cameras, Figure III.38) whose output is used as feedback to the controller to maximize the accuracy of motion. The goal is to achieve accurate motion control, with capability to reject unwanted disturbances for both constant set-point regulation and time-varying trajectory tracking of the wind tunnel model. The real-time control system utilizes two *Quanser* Q8 real time data acquisition boards that are used for signal communication of the motor commands, the motor encoders, the actuator commands, and the load cells measured. The controller also has eight available output channels for external trigger signals as well as modulation signals to be implemented with the model-embedded flow control elements.

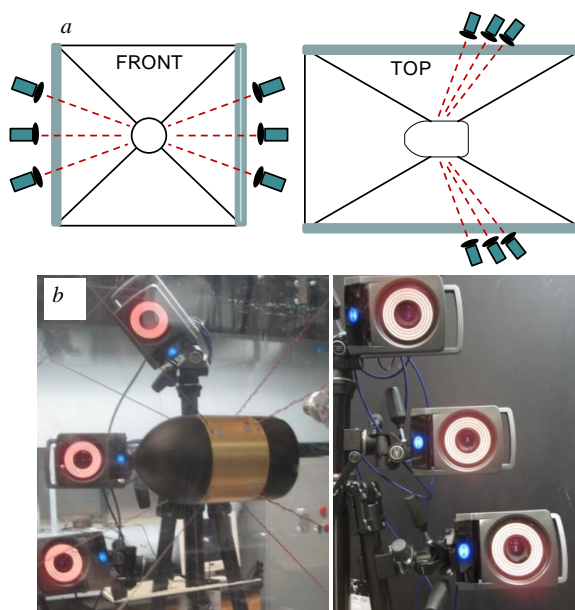


Figure III.38 Vicon motion analysis system: a) Schematic of the test configuration, and b) the actual hardware in the tunnel.

An important feature of this traverse is the routing of electrical signals for optimal realization of a real time controller. The user interfaces with a master computer which uses *Simulink* as an interface to build the controller. Upon completion of the desired controller, the code is compiled with *Microsoft* Visual Studio into an optimized C-script and transmitted through Ethernet to a high performance host computer with a *QNX* real-time operating system, with minimal delay and overhead in signal communication. When the master computer sends the execution command, the C-script on the host machine is executed interfacing in real time with the servo amplifiers, and sending signals back to the master machine with time-stamps for accurate data recording. The host machine has two *Quanser* Q8 real time data acquisition boards that are used for signal communication of the motor commands, the motor encoders, the actuator commands, and the load cells measured. The host machine is also connected via Ethernet cable to the broadcasted signal from the *Vicon* machine to use the position measured from the camera system as feedback for the control system code.

The load cells and piezoelectric actuator wires are both analog signals routed through the model test section to the host computer. The piezoelectric signals are generated as modulation signals

on the order of ~ 10 VAC with frequencies ~ 100 Hz in the host machine, which are routed to external function generators and amplifiers to create an actuation signal on the order of ~ 100 VAC and ~ 1 kHz to the model. The signal to noise ratio of the piezoelectric signal is very high, with noise of on the order of mV, and therefore minimal filtering is required. The load cell signals however are on the order of mV and are susceptible to noise, so each load cell is routed with a short cable to two nearby electronics boxes with exterior metal shields and corresponding amplifiers and RC filters to ensure the signal accuracy. This captured signal is then routed through Ethernet cables directly to the host machine.

Electric Drive Design

The electrical system designed for the six degree of freedom traverse can be considered as two separate composite subsystems. The first element is the high power distribution system that routes 480V AC power to the 8 individual servo amplifiers. Each servo amplifier is individually fused and is mated with the manufacturer recommended EMI filter. Upstream power is routed thorough a multi-pole horsepower rated contactor used as a part of the safety system (this component removes servo power when a kill switch is activated). The *Yaskawa* servo motors have an integrated 1 million count absolute encoder. Each servo amplifier provides an incremental encoder output derived from the absolute encoder as one of its functions. The current traverse has an accompanying sophisticated electrical design for routing power and signals. Each of the servo actuators run on three phase 480V AC power, and the accompanying system is designed to be safe and easily operational, and additionally the electrical radiation of power causes a lot of inherent signal noise, so diligent routing of the analog signals from the load cells and actuators, as well as digital filtering are paramount to the traverse's operation. Each servo actuator has a corresponding amplifier that provides power and interprets command signals from the host computer which the control system is executed on. These servo amplifiers are placed in an external electronics cabinet with in-series fuses to ensure the safety of each of the motors, as well as the user, and an external computer is used to program the initial settings and limit switches on the servo actuators.

III.3.2 Controller Design

The fundamental mathematical description of the system is as follows: There is an over-constrained model to be controlled in six output degrees of freedom ($x, y, z, \alpha_x, \alpha_y, \alpha_z$), to which there are eight input motor angles (m_1, \dots, m_8). The model has an inertial force and moment (F_I), an aerodynamic force and moment (F_A), and a gravitational force and moment (F_G) acting on it. In addition, each mounting cable has a tension (T_1, \dots, T_8) that is dependent on the forces on the body, as well as the motor angles. Each motor shaft has a certain amount of inertia and damping, and each wire is assumed to have an aerodynamic force that is entirely form drag, with negligible inertial force or friction drag. The mounting locations of each of the centers of the motor pulleys are known, along with the corresponding pulley radii. The mounting locations of each of the wires in the body are also known relative to the center of the model. The wires are not assumed incompressible, but each one is assumed to compress only as a spring with known

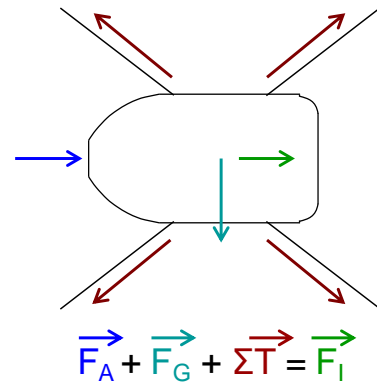


Figure III.39 Free body diagram of the aerodynamic platform.

elastic modulus and cross-sectional area.

In order to build a functional controller, there needs to be stable real-time solutions to two problems: the first is a calculation of the model orientation ($x, y, z, \theta_x, \theta_y, \theta_z$, and all components of F_A) given the motor orientation ($m_1, \dots, m_8, T_1, \dots, T_8$), where all values at the previous time step and all geometric variables are allowed to be used. To fully define the 6 degree of freedom coordinate system, a yaw first, pitch second, and roll last coordinate rotational system is adopted. In order to accurately model the traverse motion, the first function that is required is the direction of each mounting wire given the motor positions, model position, and wire tensions from the frame of the aerodynamic model shown in Eq. 1:

$$\begin{pmatrix} W_{x,n} \\ W_{y,n} \\ W_{z,n} \end{pmatrix} = \text{function}(x, y, z, \alpha_x, \alpha_y, \alpha_z, m_1, \dots, m_8, T_1, \dots, T_8, \text{and Mechanical Constants}) = \vec{W}_{3 \times 8} \quad (\text{Eq. 1})$$

The second function that is required is a relation between the wire tensions and the force on the model. This is done with a force and moment balance with the inertial, gravitational, and aerodynamic forces and moments with the wire tension, as shown in Figure III.39. The gravitational force and inertial force are entirely dependent on the orientation of the model, and independent of the orientation of the wires. This allows Eq. 1 to be reorganized as shown below in Eq. 2:

$$\vec{X} = \begin{pmatrix} x \\ y \\ z \\ \alpha_x \\ \alpha_y \\ \alpha_z \\ F_{Ax} \\ F_{Ay} \\ F_{Az} \\ F_{A\theta_x} \\ F_{A\theta_y} \\ F_{A\theta_z} \end{pmatrix} = \vec{C}_{12 \times 16} * \begin{pmatrix} m_1 \\ \dots \\ m_8 \\ T_1 \\ \dots \\ T_8 \end{pmatrix} = \vec{C} * \vec{M}, \quad \text{where } \vec{C} = \text{function}(\vec{W}, \text{Mechanical Constants, and time}) \quad (\text{Eq. 2})$$

The formulation of variables and constants as shown in Eq. 2 is powerful because it separates forces and displacements of the model (\vec{X}), with the tensions in the wires and the positions of the motors (\vec{M}). The transformation matrix between these two quantities (\vec{C}) depends on the orientation of both \vec{M} and \vec{X} and therefore must be reevaluated at each time step, where the current controller linearizes this calculation to optimize runtime and allow the controller to operate at 1 kHz. The inverse calculation from the model coordinates to the motor coordinates is also quickly computed with a least norm

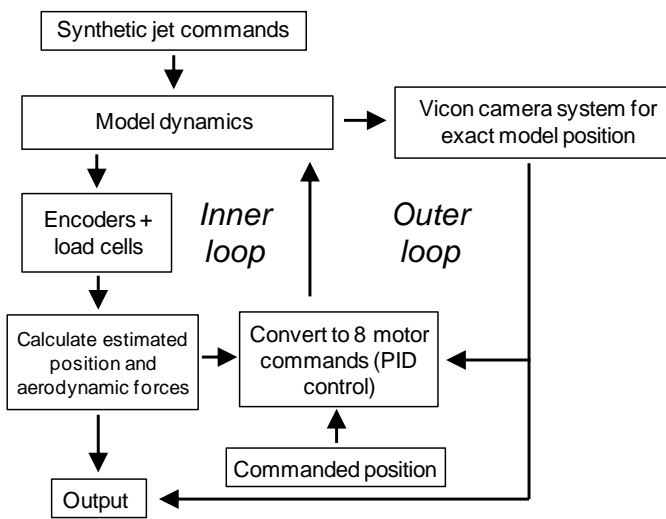


Figure III.40 Schematics of the control loop for achieving a commanded dynamic position.

matrix inverse solution.

This investigation uses an in-house designed controller to investigate the dynamic motion and force response of the model with the motorized traverse. The controller commands a dynamic position path and measures the aerodynamic forces and moments caused by both actuation and motion along that dynamic path.

A depiction of the control operation mode is shown as a block diagram in Figure III.40. The commanded position is specified to the controller as a six-vector, and it is compared with the measured position estimate determined from the load cells and motor encoders. This comparison is used to calculate an eight-vector of desired motor positions, and the motor command is then generated from the desired motor positions using PID control. The motors then effect the model dynamics, which is then interpreted by the encoders and load cells, thus closing an "inner loop" control. The load cell and encoder readings, as well as the estimated aerodynamic forces and model positions are recorded for data analysis. Independent synthetic jet commands can be defined by the user triggered relative to the desired motion, and the effect that the jets have on the aerodynamic forces and model motions are measured through the encoders and load cells as well. In addition, the motion analysis system is set up and calibrated for a much more accurate measurement of the model motion response, and is incorporated into the controller as an "outer loop" which is used to modify the motor commands to minimize the error between the desired motion and the recorded motion in the camera system, which is also done with PID control.

III.3.3 Dynamic Traverse Response

The implementation of the traverse in dynamic position command mode, as discussed in §III.3.2, is first demonstrated on canonical model motions. The model is set to be constrained along a specified dynamic path and the traverse records the forces that the model encounters as it moves. The mounting mechanism motion is limited in each of the different degrees of freedom by the path of the mounting wires, where the extremes of the motion are determined by where the mounting wires can no longer physically hold the model fixed in a certain orientation. An illustration of the achieved range of the motion of the traverse is shown in Figure III.41 for four of the six degrees of freedom. It is important to note that the range of pitch motion is larger than the amplitude of instabilities observed in a single degree of freedom model previously in §III.2, which was on the order of 8° .

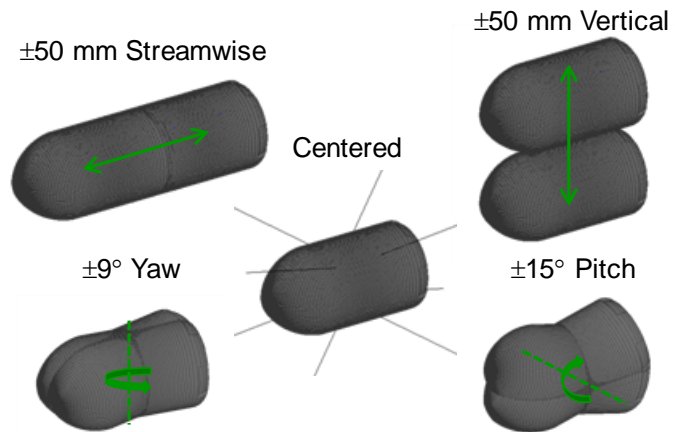


Figure III.41 Illustration of the traverse range of motion achieved in four degrees of freedom.

The system dynamic performance is characterized in terms of displacement range and frequency of sinusoidal commands and is depicted in Figure 6. The displacement amplitude is 50 mm plunge (x , y , and z), $8^\circ \alpha_x$, $9^\circ \alpha_z$, and $15^\circ \alpha_y$ at $f = 0.5$ Hz, and decreases to 5 mm (x , y , and z),

$1^\circ \alpha_x$, $2^\circ \alpha_z$, and $3^\circ \alpha_y$ at $f = 20$ Hz. The range of motion decreases with frequency of motion because the inertial force grows proportional to the acceleration of the system, and increases the required torque of the motors at higher frequencies. This larger torque requires the tension in the mounting wires to increase with the same motion range, and because the load cells are limited to 110 N of tension, the range of the motion of the system has to decrease.

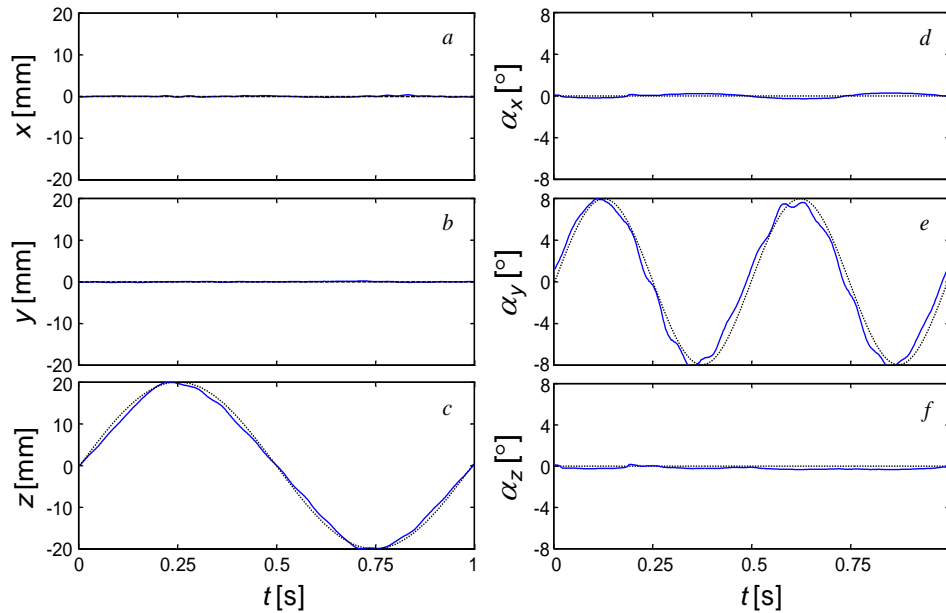


Figure III.42. *Traverse motion response for a controlled 1 Hz, 20 mm plunge and 2 Hz, 8° pitch with the translations (x, y, z) and rotations ($\alpha_x, \alpha_y, \alpha_z$), with desired response shown in dotted black and obtained response shown in blue.*

To test the position controller, a combination of translation and rotation is commanded and depicted in Figure III.42a-f with streamwise translation x , cross stream translation y , vertical translation z , roll α_x , pitch α_y , and yaw α_z , respectively. The commanded signal is a 20 mm amplitude sinusoidal plunge at 1 Hz with a simultaneous 8° amplitude sinusoidal pitch as shown with black dotted lines. The achieved path is shown in blue which shows great agreement with the commanded signal, with the largest deviation between the commanded and desired signals shown in the pitching angle, with a maximum error of around 0.5° . This error will arguably be diminished further with the future tuning of the PID controller that implements the motor commands.

III.3.3 Aerodynamic Response of the Centered Body

Before examining the model dynamics, a study was conducted to assess the synthetic jet control authority on generation of aerodynamic forces and moments on the axisymmetric body held stationary at the central position, to compare such results on the current model support and those from the previous studies (Abramson et al. 2011 and 2012, and §III.1.2).

Initially, a study of the drag of the model is conducted on the body held at center. The drag force was measured over a range of wind tunnel speeds as F_D . The expected wire drag is calculated treating the wires as cylinders with flow over them of the projected wind speed across the

cylinder F_W . The value of the extracted platform drag ($F_D - F_W$) is plotted against the dynamic pressure multiplied by the platform cross-sectional area to resolve a coefficient of drag (C_D) of 0.238, with good agreement with the expected C_D of 0.25 from Hoerner (1965), as shown in Figure III.43. The rest of the current investigation is conducted at the fixed free stream speed of $U_0 = 40$ m/s.

Next, the effects of the hybrid actuators are investigated with the jet momentum coefficient set to $C_\mu = (U_j^2 \cdot A_j) / (U_0^2 \cdot \pi D^2) = 3 \cdot 10^{-3}$, and the actuation cycle frequency set to $f_{cycle} = 1.4$ kHz ($\tau_{cycle} = 0.7$ ms). When the synthetic jets are inactive, the model experiences separation off of each of the backward facing steps on the aft end of the model, and the jet actuation leads to the partial attachment of the outer flow along the Coanda surface resulting in a reaction force by the turning of the outer flow into the wake region. This vectored wake induces a reaction force and moment on the model, which is shown in Figure III.44. The moment on the body throughout this work is measured relative to mounting center of wires on the body at x_m . The response of a single actuator measured by the load cells is shown in Figure 8a,b, and c, showing the actuator induced forces, $\Delta F_D = 0.03$ N and $\Delta F_L = 0.6$ N, and the actuator induced moment, $\Delta M_P = 0.008$ Nm, which is in good agreement with previous studies by Abramson et al. (2011, 2012), and in the study presented in §III.1.2. When both jets are activated, the effect of the jets in ΔF_L and ΔM_P is canceled out (Figure III.44d and e), while the actuator induced drag is approximately doubled to $\Delta F_D = 0.06$ N (Figure III.44f).

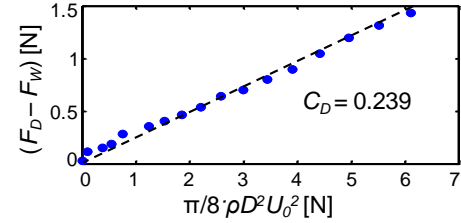


Figure III.43. Measured model drag (•) with scaled tunnel speed and a linear fit yielding the measured drag coefficient.

To understand the actuation-induced wake development while the axisymmetric model is centered, different actuation schemes are applied and the resulting flow fields are investigated with planar PIV. Figure III.45 shows the ensemble-averaged flow field (based on 300 individual flow realizations) in terms of the mean velocity field vectors overlaid on a raster plot of the mean vorticity, ζ , at the central vertical plane of the model. Figure III.45a shows the model wake without flow control, having expected symmetry about the body's axis. Although the flow field is axisymmetric (in a time-averaged sense), the upper and lower shear layers have a different sense of ζ due to the Cartesian coordinate system utilized in the measurement plane for calculating ζ . Figure III.45b shows the model wake with the top jet actuated, deflecting the wake downwards across the centerline and inducing a large asymmetry while decreasing the extent and magnitude of the region of ζ near the jet. This wake deflection causes a reaction on the model with positive ΔF_L and negative ΔM_P , as shown in Figure III.44b. Figure III.45c, showing both

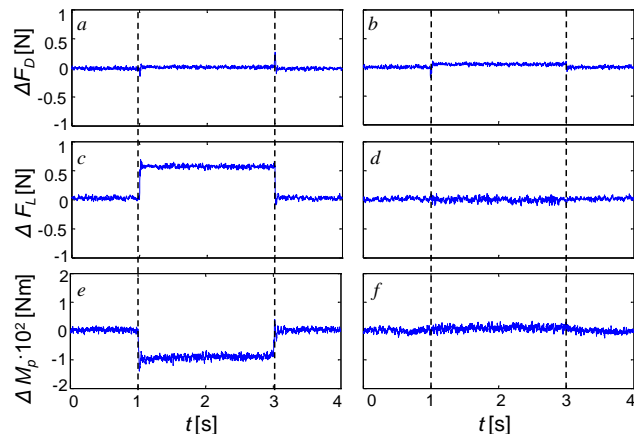


Figure III.44. Actuator induced drag (a,b), lift (c,d), and pitch moment (e,f) for one (a,c,e) and two (b,d,f) jets activated at $C_\mu = 3 \cdot 10^{-3}$ with jet onset and termination shown by dotted lines.

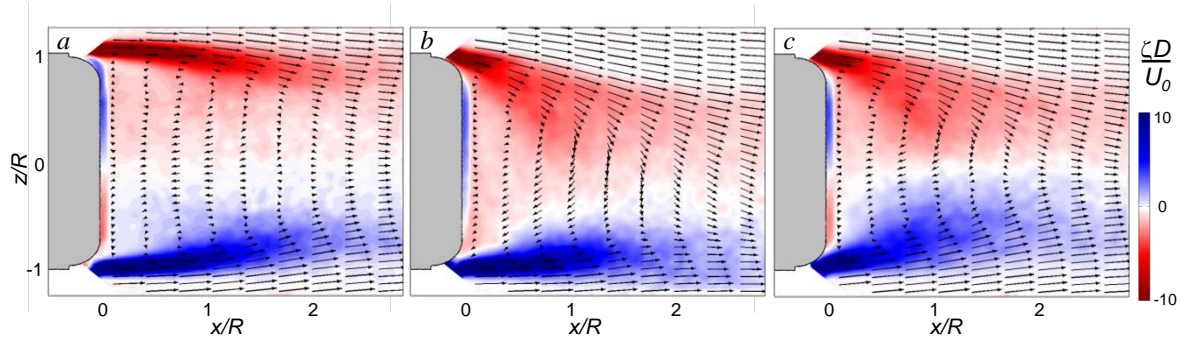


Figure III.45 Raster plots of the mean vorticity field with overlaid mean velocity vectors for a static model at $\alpha_\gamma = 0^\circ$ for the baseline (a), and the flows actuated by the top (b), and both top and bottom (c) jets at $C_\mu = 3 \cdot 10^{-3}$.

jets activated, causing the extent and magnitude of the region of ζ near each jet to decrease, and vectors the wake on both side closer to the center, closing the wake. Because this flow field is again symmetric, there is no ΔF_L or ΔM_P on the model, and the ΔF_D seen in Figure III.44f can be attributed to the change in shape and magnitude of the wake velocity outside of the controlled perimeter.

III.3.4 Aerodynamic Response of the Moving Bluff Body

Once the centered model response has been assessed, the main investigation focuses on commanding a dynamic response from the body. As an example of the canonical motion, the remainder of the present work focuses on sinusoidal pitch commands for the model motion. Figure III.46 shows the measurement of the lift induced on the model commanded for sinusoidal pitching at $f = 1$ Hz (a reduced frequency of $k = \pi c f / U_0 = 0.013$), and an amplitude of 3° . The force and moment traces presented here are the average of 100 seconds of data for noise suppression. The recorded lift force variation with pitching angle (F_L vs. α_γ) is plotted in Figure III.46a, and the pitching moment trace (M_P vs. α_γ) is shown in III.46c. It is notable that both F_L and M_P increase with increasing α_γ . In addition, a secondary traverse command is implemented with the same motion of the model with the top jet continuously actuated, where lift force induced solely by the actuation is plotted with pitching angle (ΔF_L vs. α_γ) in Figure III.46b, and the actuator induced pitching moment trace (ΔM_P vs. α_γ) is shown in III.46d. Activation of the top actuator in Figures III.46b and d vectors the wake downwards towards the center, causing a reaction force on the model with positive ΔF_L and negative ΔM_P , where the magnitude of the ΔF_L and ΔM_P depends on α_γ . Because F_L and M_P

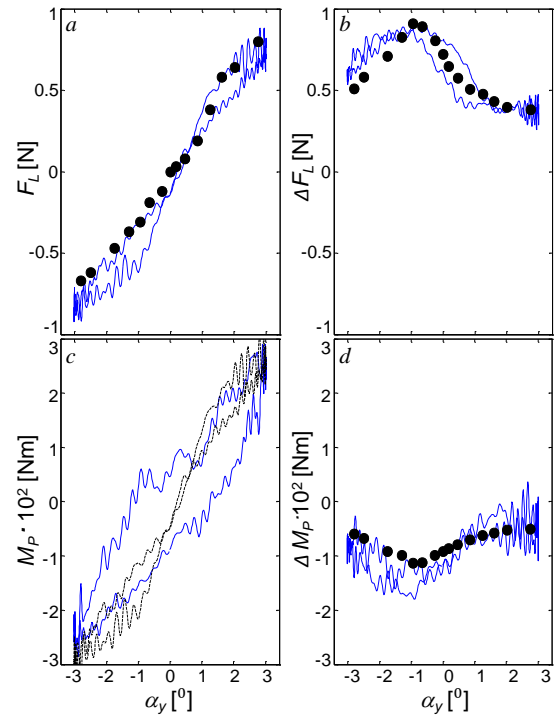


Figure III.46 Motion induced lift (a) and moment (c), and actuation induced lift (b) and moment (d), as well as the expected moment using the known center of pressure on the centered model (—) and the corresponding data of Fig. III.8 (●).

have the same sense and ΔF_L and ΔM_P have the opposite sense, actuation chosen to decrease F_L throughout the pitching cycle consequently increases M_P . It is observed that the maximum magnitude of induced $\Delta F_L = 0.9\text{N}$ and $\Delta M_P = -0.01\text{Nm}$ by the top actuator occurs when the model is pitched down to $\alpha_y = -1^\circ$, which is attributed to the geometry of the backward facing step, and the respective flow field on the model's aft end. The present range of body orientations were investigated in the previous study on the hoop-supported model held at a static angle of attack (§III.1.3). In that work, F_L , ΔF_L and ΔM_P were recorded (Figure III.8), and they are also plotted in Figure III.46a, c, and d in solid symbols. There is a small deviation in the ΔF_L and ΔM_P past the maximum values at $\alpha_y < -1^\circ$, but the agreement is very strong everywhere outside of this region. In addition, the center of pressure (C_p) of the centered model is known to be about $x/c = 0.24$ upstream of x_m , and the expected moment on the model ($F_L \cdot C_p$) is plotted in Figure III.46c in black. This measured moment has more hysteresis than the expected moment due to variations in the C_p over the cycle.

The primary emphasis of the current work is to assess the control authority of hybrid actuators on the present model when it is dynamically pitching. An important aspect of flow control implementation in dynamic configurations is the frequency response of both the hybrid actuators and the baseline flow. The onset of actuation induces a ΔF_L and ΔM_P response that acts like a step function with a rise time of about 20 ms (50 Hz), as shown in Figure III.44, with the magnitude of ΔF_L and ΔM_P on α_y as well as its rate, $\dot{\alpha}_y$. The frequency response of the baseline flow is analyzed using representative samples of $f = 1, 5, 10$, and 20Hz ($k = 0.013, 0.065, 0.130$, and 0.259, respectively) that span a range from pseudo-steady to quasi-unsteady frequencies, shown in Figure III.47. The emphasis of this investigation is on using actuation for steering and stabilization of an airborne model in pitch motion, and therefore the rest of this work places emphasis on the lift force trace, F_L vs. α_y , and pitch moment trace, M_P vs. α_y . Furthermore, as the pitch motion is detected

as representative for the flow control assessment, only two control jets are utilized in the remaining sections of the paper, namely the top and bottom jets. Figure III.47a and e show F_L vs. α_y , and M_P vs. α_y , respectively, of the model pitching at $k = 0.013$, as the 'low' frequency representative, which was shown to be in agreement with previous static data in Figure III.46a and c. Figure III.47b and e show the change in the F_L vs. α_y and M_P vs. α_y for $k = 0.065$, where the peak values of F_L remain similar,

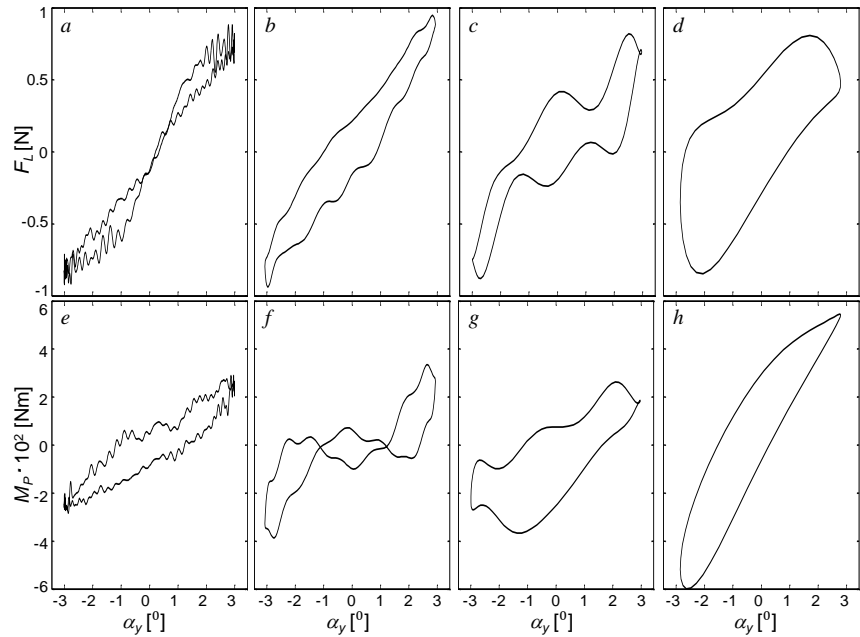


Figure III.47. Motion induced lift (a–d) and moment (e–h), development with pitch angle, α_y , at reduced frequencies $k = 0.013$ (a,e), 0.065 (b,f), 0.130 (c,g), and 0.259 (d,h).

yet the corresponding peak values of M_P increase. In addition, the path and hysteresis of both F_L vs. α_y and M_P vs. α_y are also altered. This pattern continues through $k = 0.13$, shown in Figure III.46c and g, and the 'high' frequency representative, $k = 0.259$, shown in Figure III.46d and h, where the F_L peaks remain unaltered (compare Figures III.47a-d), and the M_P peaks increase (compare Figures III.47e-h). The F_L vs. α_y and M_P vs. α_y paths and hysteresis vary notably with k , and therefore an actuation has to be tailored to effectively address the baseline response of the k of interest, as discussed below in §III.3.5.

To understand the baseline wake development of the dynamic model during oscillation at different k cycles, the phase averaged flow field is measured in a similar style to the time averaged flow field in Figure III.45. Figure III.48 shows six phase-averaged flow fields (based

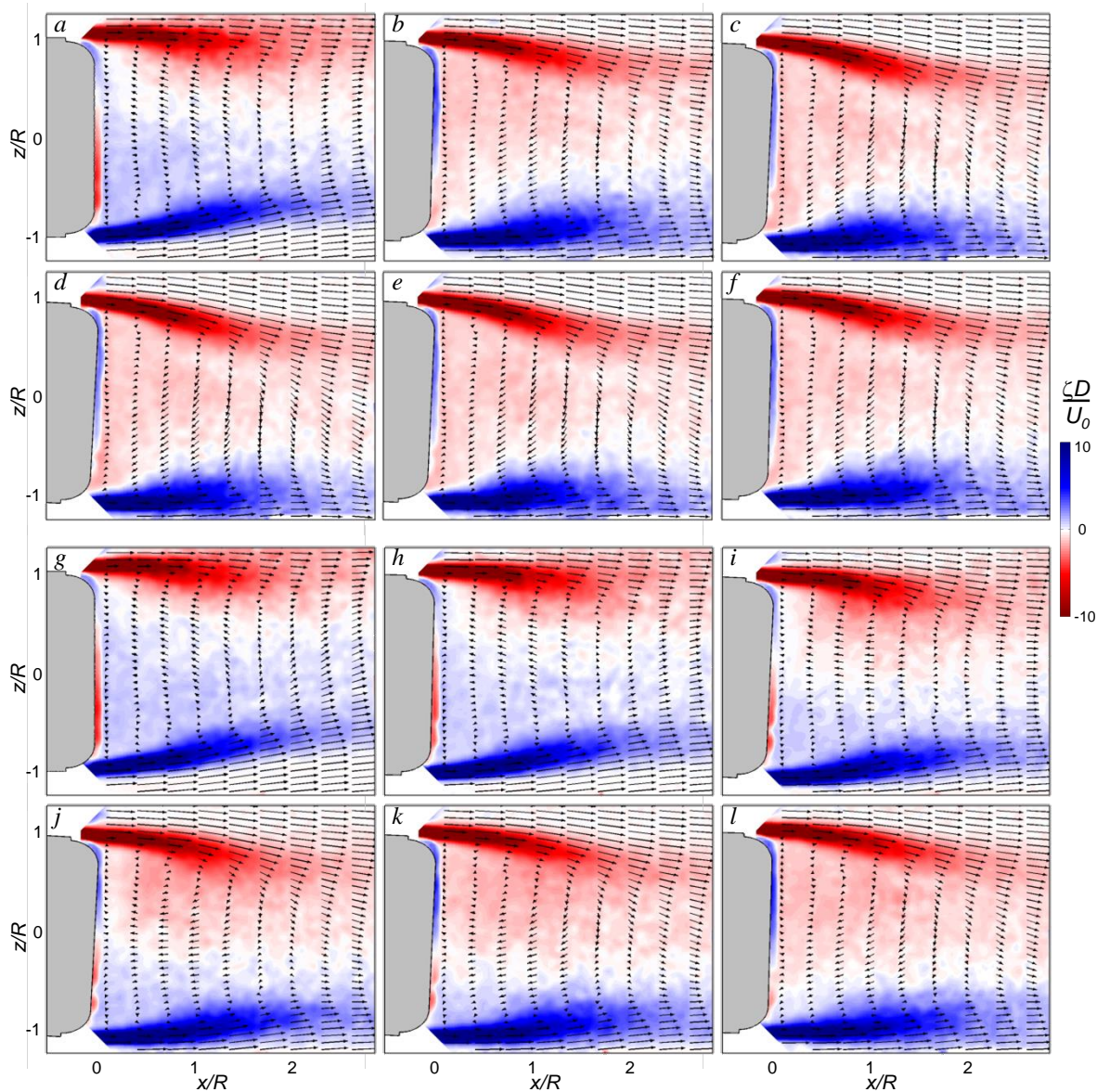


Figure III.48 Raster plots of the phase-averaged vorticity field with overlaid phase-averaged velocity vectors for $\alpha_y = \pm 3^\circ$ sinusoidal pitch at reduced frequencies of $k = 0.013$ (a-f), and 0.259 (g-l), at $t/\tau = 0$ (a,g), 0.083 (b,h), 0.167 (c,i), 0.25 (d,j), 0.333 (e,k), and 0.417 (f,l).

on 300 individual realizations) in terms of the velocity field vectors overlaid on a raster plot of ζ , at the central vertical plane of the model for $k = 0.013$ ($\tau = 1$ s, Figure III.48a-f), and $k = 0.259$ ($\tau = 50$ ms, Figure III.48g-l). The baseline cycle is symmetric regardless of frequency, therefore the phases chosen for brevity are representative for the first half cycle: $t/\tau = 0$ (Figure III.48a and g), 0.083 (Figure III.48b and h), 0.167 (Figure III.48c and i), 0.25 (Figure III.48d and j), 0.333 (Figure III.48e and k), and 0.417 (Figure III.48f and l). The model pitching angle corresponding to these phases is $\alpha_y = 0^\circ, 1.5^\circ, 2.6^\circ, 3^\circ, 2.6^\circ$, and 1.5° , respectively. In both Figure III.48a-f and Figure III.48g-l, the shear layer follows the model, and in both Figure III.48a and Figure III.48g, the shear layer is not centered when the model is at center, due to the wake lagging the model by a function of the convective time scale ($\tau_{conv} = D/U_0 = 2.25$ ms). However, this time scale is a much larger portion of the cycle when the model is moving faster, leading to much more asymmetry in Figure III.48g than in Figure III.48a, which is also commensurate with the increase in F_L vs. α_y , and M_P vs. α_y hysteresis with k shown in Figure III.47. In Figure III.48a, the wake ζ is predominantly counterclockwise, while, as it starts to pitch up $t/\tau = 0.083$ in Figure III.48b, the wake is dominated by the clockwise sense of ζ for the remainder of the pitch up cycle. In contrast, for $k = 0.259$, the ζ does not become clockwise dominant until $t/\tau = 0.167$, and the development of ζ is much more gradual throughout (compare Figures III.47a-f to Figures III.47g-l). It is expected that the ζ should develop as a function of the model convective time scale, which is a larger fraction of the $k = 0.259$ pitching motion, leading to the difference in the developed ζ over phase, as well as the difference of the F_L vs. α_y and M_P vs. α_y paths in Figure III.47.

III.3.5 Aerodynamic Force and Moment Control using Continuous Actuation

After the aerodynamic response from the body's baseline flow is assessed, the flow control actuation schemes are designed. To further understand the control authority of the hybrid actuation throughout a pitching cycle, the effect of continuous actuation by either the top or both the top and the bottom jets is examined over a range of k . The continuous actuation by a single (top) jet and dual (top and bottom) jets is shown in red and blue, respectively, in Figure III.49 with the baseline response shown as a dotted line for reference. Figures III.49 a and e show the response at $k = 0.013$ with significant ΔF_L and ΔM_P by one jet throughout the cycle, with a maximum effect at $\alpha_y = -1^\circ$, in agreement with Figure III.46a and c. When both jets are activated, the result is a F_L vs. α_y and M_P vs. α_y that is similar to the baseline case, showing that both jets impose equivalent but opposing effects and hence effectively cancel out the induced effect of each other. Figures III.49b and f show the response at $k = 0.065$, where there are several noticeable differences from the lowest $k = 0.013$, where the F_L vs. α_y and M_P vs. α_y path of both the single top jet and two jets has changed. It is noteworthy that although the F_L vs. α_y and M_P vs. α_y paths have changed from the lower frequency, the continuous actuation traces remain similar to the baseline paths, with the top jet path deflected to a larger F_L and lower M_P and the both jets path centered about the baseline paths. This trend continues in $k = 0.130$ (shown in Figures III.49c and g) and $k = 0.259$ (shown in Figures III.49d and h) with the actuated paths remaining similar to the non-actuated paths, and the activation of one jet causing a deflection of the path, with the largest variation occurring in the F_L vs. α_y path at $k = 0.130$ (Figure III.49c). It is also noteworthy that at the frequencies $k = 0.065$ and 0.130 the actuation effect changes to an induced $\Delta F_L = 0.6$ N and $\Delta M_P = -0.02$ Nm approximately independent of α_y (Figures III.49b,c,f and g) rather than an effect of $\Delta F_L = 0.9$ N and $\Delta M_P = -0.01$ Nm at a maximum

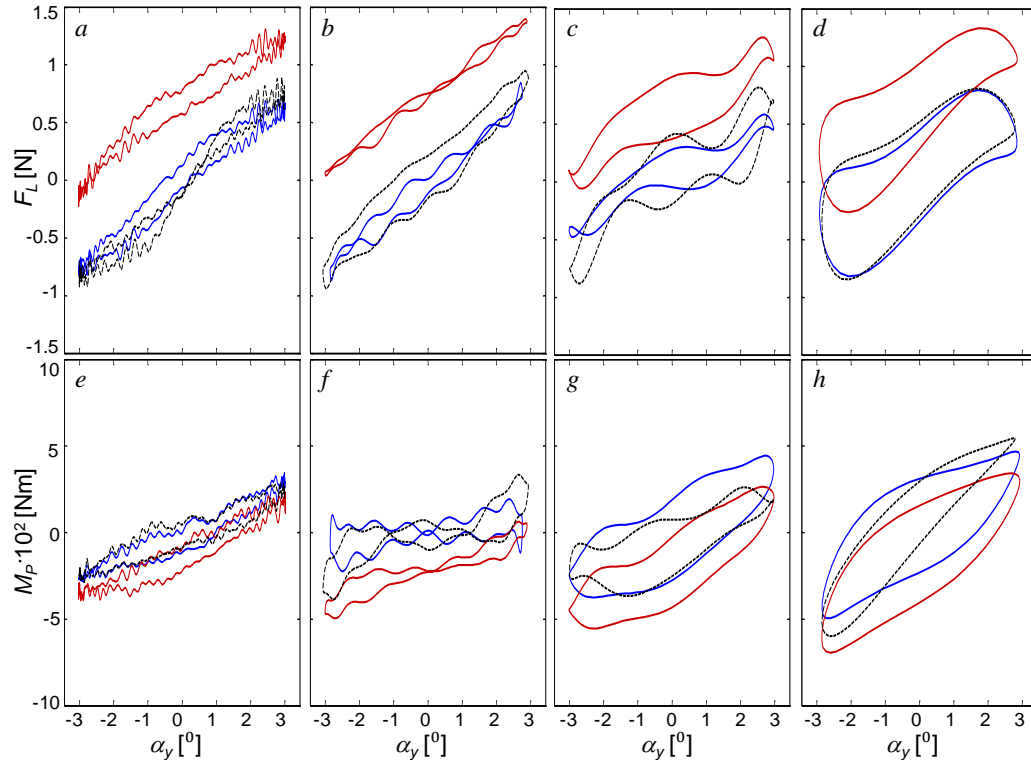


Figure III.49 Lift force (a-d) and pitching moment (e-h) for open-loop continuous activation of one (red) and both (blue) jets at $C_\mu = 3 \cdot 10^{-3}$ and $k = 0.013$ (a,e), 0.065 (b,f), 0.130 (c,g), and 0.259 (d,h). The non-actuated cases are shown in dashed (black) lines.

$\alpha_y = -1^\circ$ in the 'low' frequency of $k = 0.013$ (Figures III.49a and e). This change is attributed to the model moving fast enough that the flow doesn't have enough time to fully respond to the 'small' geometry of the backward facing step, and there is no longer dependence between the pitching angle and this local geometry. In the 'high' frequency case $k = 0.230$ again starts to vary with α_y , having a maximum effect of $\Delta F_L = 0.5\text{N}$ and $\Delta M_P = -0.015\text{Nm}$ at $\alpha_y = 3^\circ$ (Figure III.49 d and h). The emergence of this maximum at $\alpha_y = 3^\circ$ at $k = 0.259$ is attributed to the model moving fast enough such that the flow cannot fully respond to the model dynamic cycle, and therefore some parts of the pitching cycle become more favorable for actuation than other parts due to the altered shear layer dynamics. It is notable that the hysteresis in both the baseline and actuated responses in Figure III.49 increases with oscillation frequency past $k = 0.065$, which is due to the flow development (function of τ_{conv}) taking up a larger percentage of the cycle, τ , but the nature of the flow development (hence path of F_L and M_P) is similar for the baseline and actuated cases with a fixed frequency. Although the actuation effects differ for different frequencies, it is important to note that this continuous actuation has a sizable effect across all the pitch frequencies tested, causing an average deflection on the order of $\Delta F_L \sim 0.6\text{N}$ and $\Delta M_P \sim -0.01\text{Nm}$ with one jet, and effectively cancelling this deflection with both jets, and preserving similar F_L vs. α_y and M_P vs. α_y paths with respect to the baseline flow in all cases.

To understand the similarity of the actuation-induced wake development with frequency while the axisymmetric model is pitching with amplitude of 3° , the baseline, top jet, and both jets continuous actuation flow fields are investigated with planar time-averaged PIV. Figure III.50 shows the time-averaged flow field (based on 500 individual flow realizations) in terms of the mean velocity field vectors overlaid on a raster plot of ζ , at the central vertical plane of the

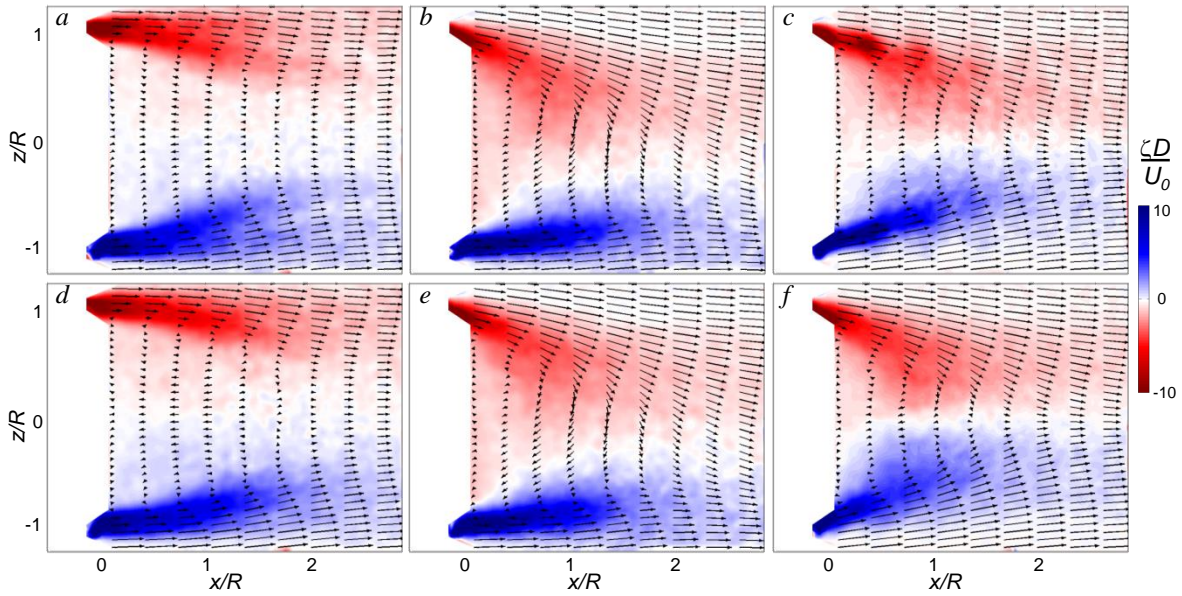


Figure III.50. Raster plots of the time-averaged vorticity field with overlaid time-averaged velocity vectors for $\alpha_y = \pm 3^\circ$ for non-actuated baseline (a,d), and the flow controlled by top (b,e), and both (c,f) jets for $k = 0.013$ (a-c) and 0.259 (d-f) at $C_\mu = 3 \cdot 10^{-3}$.

model. Figures III.50 a-c show the model wake with $k = 0.013$, and Figures III.50 d-f show the model wake with $k = 0.259$. Figures III.50a and d show the model wake without flow control, having expected symmetry about the body's axis of symmetry, and remaining similar to Figure II.45a when the model was held stationary, with an added diffusion of the shear layer originating from the dynamic motion of the model. The similarity between Figure III.50a and Figure III.50d suggest that the shear layer deflection magnitude is similar regardless of pitching frequency, with the major difference being the phase lag of the wake response, which is observed in Figure III.48. Figure III.50b shows the model wake with the top jet actuated, deflecting the wake downwards across the centerline and inducing a large asymmetry while decreasing the extent and magnitude of the region of ζ near the jet, analogous to Figure III.45b. Figure III.50c shows both jets activated, causing the extent and magnitude of the region of ζ near each jet to decrease, and vectors the wake on both side closer to the center, thereby closing the wake, analogous to Figure III.45c. The similarity between Figures III.50b and e with Figure III.45b, and Figures III.50c and f with Figure III.45c, suggest that the shear layer deflection with jet actuation is also similar regardless of pitching frequency, which also suggests ΔF_L vs. α_y and ΔM_P vs. α_y is comparable to F_L vs. α_y and M_P vs. α_y .

III.3.6 Aerodynamic Force and Moment Control using Modulated Actuation

Results shown in Figures III.49 and III.50 clearly demonstrate that the hybrid actuation approach has a significant control authority throughout the full range of the pitching dynamics $0 < k < 0.259$. The main objective of the present study is to apply such a control approach to control the aerodynamic forces (F_L vs. α_y and M_P vs. α_y paths) on the body undergoing dynamic pitch. It should be noted that the decrease of M_P growth with α_y can be used to stabilize the model, and increasing the M_P growth with α_y can be used to accelerate steering. This is a coupled system where the baseline F_L and M_P are both increasing with α_y , yet the ΔF_L and ΔM_P

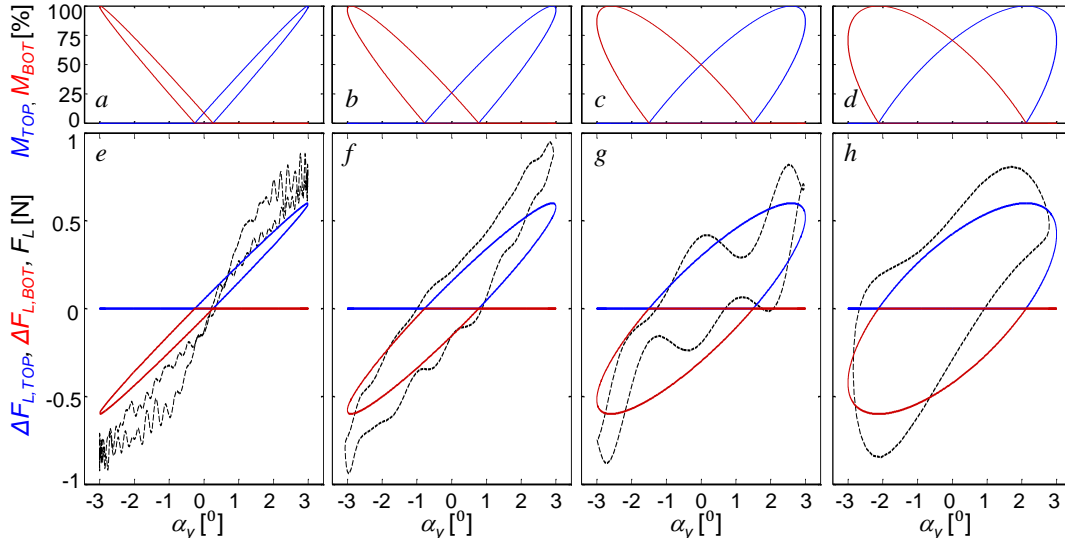


Figure III.51. Synthetic jet modulation schemes for force augmentation (a-d), and estimated actuator induced force (e-h) with top jet in blue and bottom jet in red for $k = 0.013$ (a,e), 0.065 (b,f), 0.130 (c,g), and 0.259 (d,h). The non-actuated force response is shown in dashed black. The modulation schemes for force cancellation are 180° out of phase.

by the actuators are in opposite senses, therefore increasing growth of M_P vs. α_y (for accelerated steering) simultaneously reduces growth of F_L vs. α_y , and likewise decreasing growth of M_P vs. α_y (for stabilization) simultaneously increases growth of F_L vs. α_y . As it is assessed from Figure III.49, the control authority ΔF_L relative to the baseline path of F_L was larger than ΔM_P relative to the baseline path of M_P , and therefore it is chosen to focus the flow control on augmentation of the F_L vs. α_y path as a case that can be used for stabilization, and cancellation of the F_L vs. α_y path as a case that can be used for accelerated steering. As it was presented previously (§III.3.1), the ΔF_L and ΔM_P induced by an equivalent synthetic jet varied linearly with $C_\mu < 3 \cdot 10^{-3}$, and such a relationship is utilized in the current control scheme. Modulation commands, M_{TOP} and M_{BOT} , are tailored for each jet to each of the baseline force responses of Figure III.47a-d with a jet momentum of $C_\mu = 3 \cdot 10^{-3}$ corresponding to 100% modulation, which is commensurate with a $\Delta F_L \sim 0.6\text{N}$, based on Figure III.49. Figure III.51a-d shows the resultant jet modulation signals with varying $k = 0.013$ (Figure III.51a), 0.065 (Figure III.51b), 0.130 (Figure III.51c) and 0.259 (Figure III.51d), where the only free parameter of variation used was the phase of the modulation signals. Here the top jet is shown in blue and the bottom jet is shown in red for force augmentation, although the modulation command for force cancellation can be generated by running the jets in the opposite fashion with the top jet in red and the bottom jet in blue. The corresponding predicted augmented ΔF_L using a maximum $\Delta F_L \sim 0.6\text{N}$ at 100% jet modulation for each jet, $\Delta F_{L,TOP}$ and $\Delta F_{L,BOT}$, are shown in Figure III.51e-f for these same values of k . The phase of these modulation commands was chosen such that the predicted augmented F_L is most similar to the baseline F_L , leading to the chosen modulation command phase lags of 5° ($k = 0.013$, Figure III.51a and e), 15° ($k = 0.065$, Figure III.51b and f), 25° ($k = 0.130$, Figure III.51c and g), and 45° ($k = 0.259$, Figure III.51d and h), relative to α_y .

The results of the augmentation control schemes, as described in Figure III.51, and the corresponding out of phase cancellation schemes, are shown in Figure III.52 in red and blue, respectively, with the baseline response overlaid in a dashed line. The response of F_L vs. α_y is shown in Figures III.52a-d, and the response of M_P vs. α_y is shown in Figures III.52e-h with

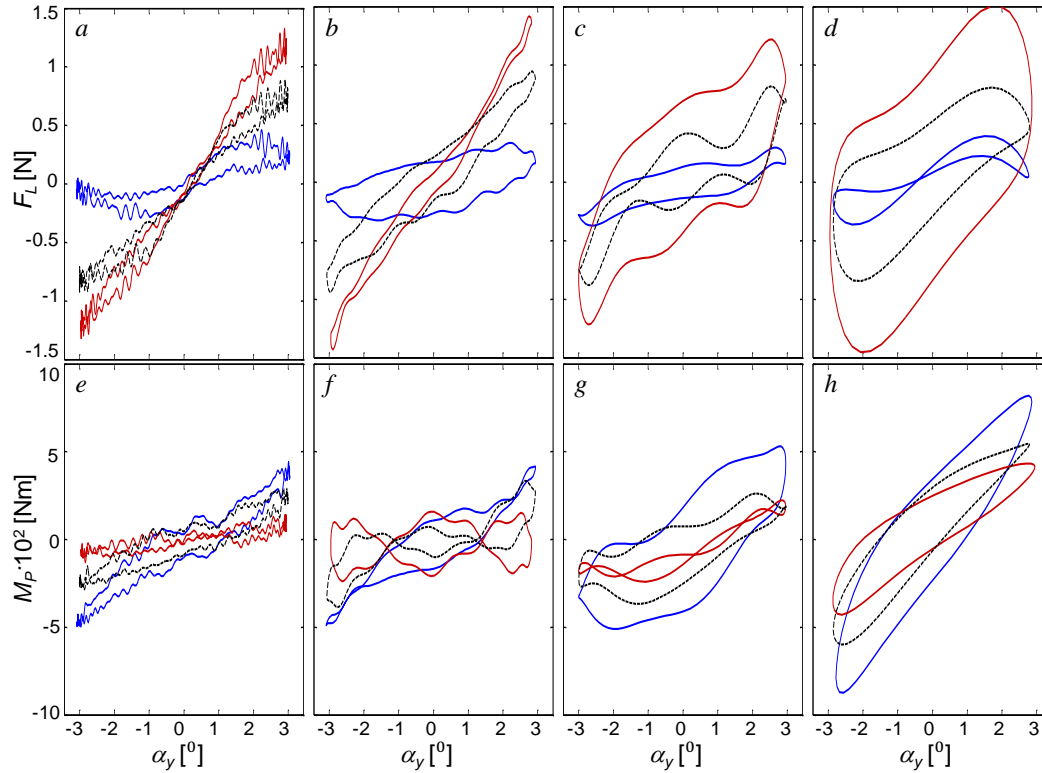


Figure III.52. Lift force (a-d) and pitching moment (e-h) for aerodynamic force cancellation (blue) and augmentation (red) with $k = 0.013$ (a,e), 0.065 (b,f), 0.130 (c,g), and 0.259 (d,h). Baseline responses are shown in dashed black.

varying k . At the lowest $k = 0.013$ (Figure III.52a), the maximum F_L is cancelled to 0.45 N or augmented to 1.3 N from its baseline value of 0.9 N, leading to a 50% decrease or a 45% increase in the force peaks. The respective case of M_P vs. α_y in Figure III.52e shows a 30% increase which can be used for model steering authority and a 65% decrease in the moment peaks which can be used for model stabilization authority. For $k = 0.065$ (Figure III.52b and f), the F_L augmentation case leads to a 55% increase in F_L with a 50% decrease in M_P , and the F_L cancellation case leads to a F_L decrease of 65% and an M_P increase of 33%. Overall, the control authority on the F_L vs. α_y increased and M_P vs. α_y decreased from $k = 0.013$ to 0.065 . At $k = 0.130$ (Figure III.52c and g), the control authority on F_L decreases slightly from $k = 0.065$, with a 50% increase and a 60% decrease, and the control authority on M_P becomes the respective 20% decrease and a 55% increase. The resulting F_L vs. α_y cancellation and augmentation effects remain significant at $k = 0.259$ (Figure III.52d and h), with induced changes on F_L of a 105% increase and a 50% decrease, with the respective changes on M_P of a 20% decrease and a 40% increase. For the two lowest k (Figure III.52a, b, e, and f) the cancelled and augmented paths show a hysteresis comparable to the baseline flow, but for $k > 0.065$ (Figure III.52c,d,g, and h), the cancellation of F_L vs. α_y decreases the force path hysteresis (decreases the lift response time relative to the cycle), and the augmentation of the F_L vs. α_y increases the force path hysteresis (increases the lift response time relative to the cycle). It is noteworthy that the hysteresis in M_P vs. α_y is of the opposite sense to the force, and therefore increasing the hysteresis of the F_L vs. α_y decreases the hysteresis of the M_P vs. α_y path, and vice versa.

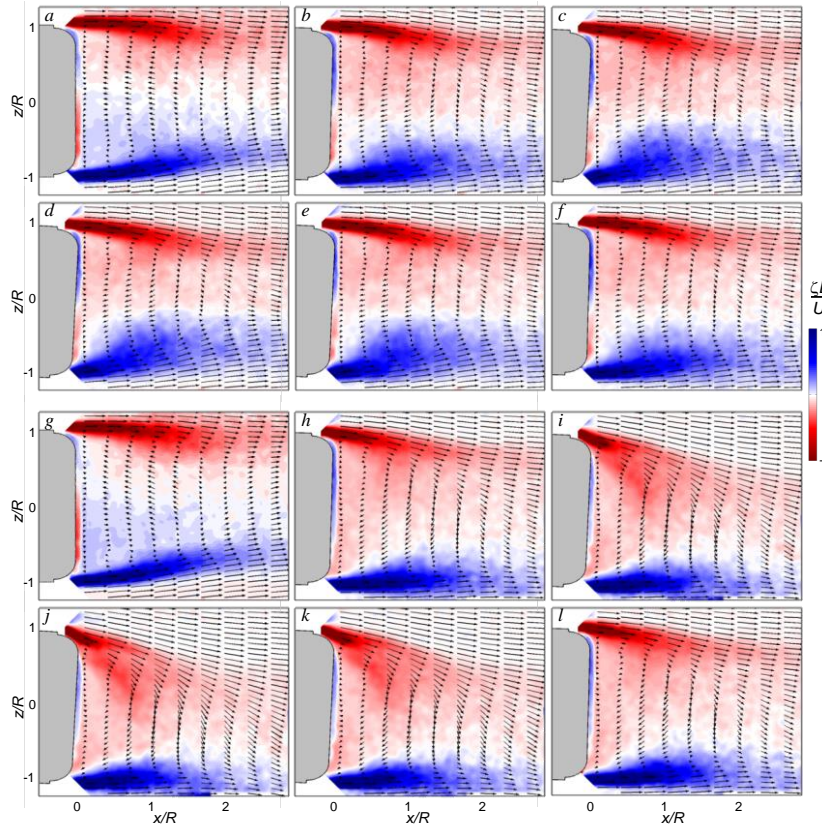


Figure III.53 Raster plots of the phase-averaged vorticity field with overlaid phase-averaged velocity vectors for $\alpha_y = \pm 3^\circ$ sinusoidal pitch at reduced frequency $k = 0.013$ using force cancellation (a-f), and augmentation (g-i) at $t/\tau = 0$ (a,g), 0.083 (b,h), 0.167 (c,i), 0.25 (d,j), 0.333 (e,k), and 0.417 (f,l).

half cycle, similar to Figure 12: $t/\tau = 0$ (Figure III.53a and g), 0.083 (Figure III.53b and h), 0.167 (Figure III.53c and i), 0.25 (Figure III.53d and j), 0.333 (Figure III.53e and k), and 0.417 (Figure III.53f and l). Based on Figure III.51, the actuation chosen for this value of k lags α_y in phase by 5° . In Figure III.53a, α_y has reached 0° and the top jet is weakly actuated. As the model pitches up to 3° in Figure III.53b-d, the bottom actuation is activated and increases in strength, causing the domain of counterclockwise ζ to increase, and the actuation then decreases from III.53d-f, causing the domain of counterclockwise ζ to decay. The presence of actuation in Figure III.53a-f causes the location of zero ζ to remain closer to the centerline and causes the velocity field to remain more symmetric about the centerline compared to the baseline flow (compare Figure III.53a-f with Figures III.48a-f), commensurate with the smaller peaks observed in the F_L vs. α_y path in Figure III.52a. For F_L vs. α_y augmentation (Figure III.53g-l), the opposite modulation command to the actuators is sent. Initially in Figure III.53g, the bottom actuator is active, and between the next phase shown in Figure III.53h the bottom actuator is terminated and the top actuator is activated. The top actuator's strength increases from Figure III.53h-j and then decreases from Figure III.53j-l. The presence of actuation in Figure III.53g-l causes the location of zero ζ to deflect farther from the centerline and causes the velocity field to remain less symmetric around the centerline compared to the baseline flow (compare Figure III.53g-l with Figures III.48a-f), commensurate with the enhanced peaks observed in the F_L vs. α_y path in Figure III.52a.

The 'low' frequency oscillation flow control cases are analyzed in detail with the phase-averaged flow fields measured by PIV. Figure III.53 shows six phase-averaged flow fields (based on 300 individual phase-referenced realizations) in terms of the velocity field vectors overlaid on a raster plot of ζ , at the central vertical plane of the model for $k = 0.013$ ($\tau = 1$ s) with the F_L vs. α_y cancellation (Figure III.53a-f), and augmentation (Figure III.53g-l). Similar to the baseline cycle, both the cancellation and augmentation actuation flow fields are symmetric across the pitching cycle, and therefore the phases chosen for brevity are representative for the first

To further understand the time varying 'low' frequency wake dynamics of both the controlled and uncontrolled flows, the time development of streamwise velocity, u_x , cross-stream velocity, u_z , and the planar vorticity, ζ in the wake behind the model is assessed. These quantities are characterized at a representative fixed downstream distance of $x/R = 1$ behind the model aft end for $0 < t/\tau < 1$. Figure III.54a shows the development of the u_x component of the wake velocity when there is no actuation present, where u_x responds to sinusoidal pitch cycle. The u_z component of the wake velocity is shown in Figure III.54d, where u_z is mostly downward for $t/\tau < 0.5$, corresponding to the wake following the model and being vectored downward when $\alpha_y > 0$, and mostly positive for $t/\tau > 0.5$, which corresponds to the wake being vectored by the model upward when $\alpha_y < 0$. Figure III.54g shows the development of ζ for the baseline flow, which also, as expected, follows a sinusoidal path similar to u_x . Upon F_L vs. α_y cancellation actuation, the wake's variation in u_x decreases significantly throughout the cycle from the baseline, as shown in Figure III.54b, and conversely, the wake's variation in u_x increases significantly with the F_L vs. α_y augmentation actuation, as shown in Figure III.54c. There is a different effect in the vertical direction, where F_L vs. α_y cancellation (Figure III.54e) causes the magnitude of the u_z to decrease significantly across the entire region throughout all times, and the F_L vs. α_y augmentation (Figure III.54f) enhances the u_z development seen in Figure III.54d. The response

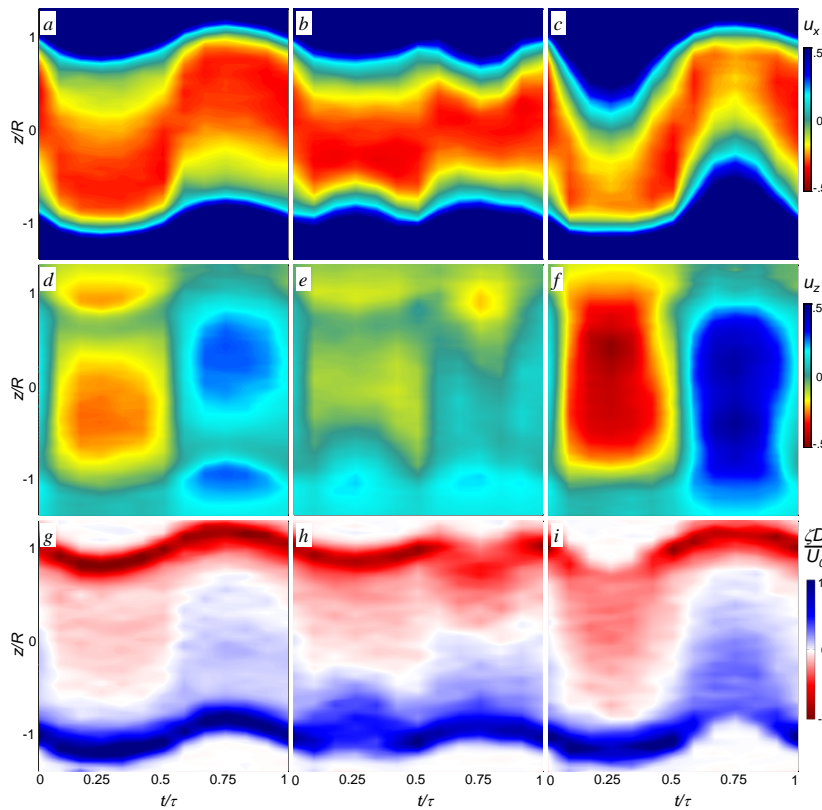


Figure III.54 Time development of streamwise (a-c) and cross-stream (d-f) velocity and vorticity (g-i) at a streamwise location of $x/R = 1$ from the model aft end for $\alpha_y = \pm 3^\circ$ sinusoidal pitch at reduced frequency of $k = 0.013$, without actuation (a,d,g), and for the force cancellation (b,e,h) and augmentation (c,f,i).

of ζ to F_L vs. α_y cancellation is shown in Figure III.54h, with a growth in the area of the shear layer upon actuation, with the bottom actuator present for $t/\tau < 0.5$ and the top actuator present for the other half of the cycle. There is a notable decrease in the deviation of the zero level of ζ with time that was observed in Figure III.53a-f, which is commensurate with the decreased force measured in Figure III.52a. The ζ response to F_L vs. α_y augmentation instead involves a strong vectoring and spreading of the shear layer and an increase in the ζ found in the wake, which increases the deviation of the zero level of ζ in the wake, commensurate with the augmentation of force measured in Figure III.52a.

The 'high' frequency, $k =$

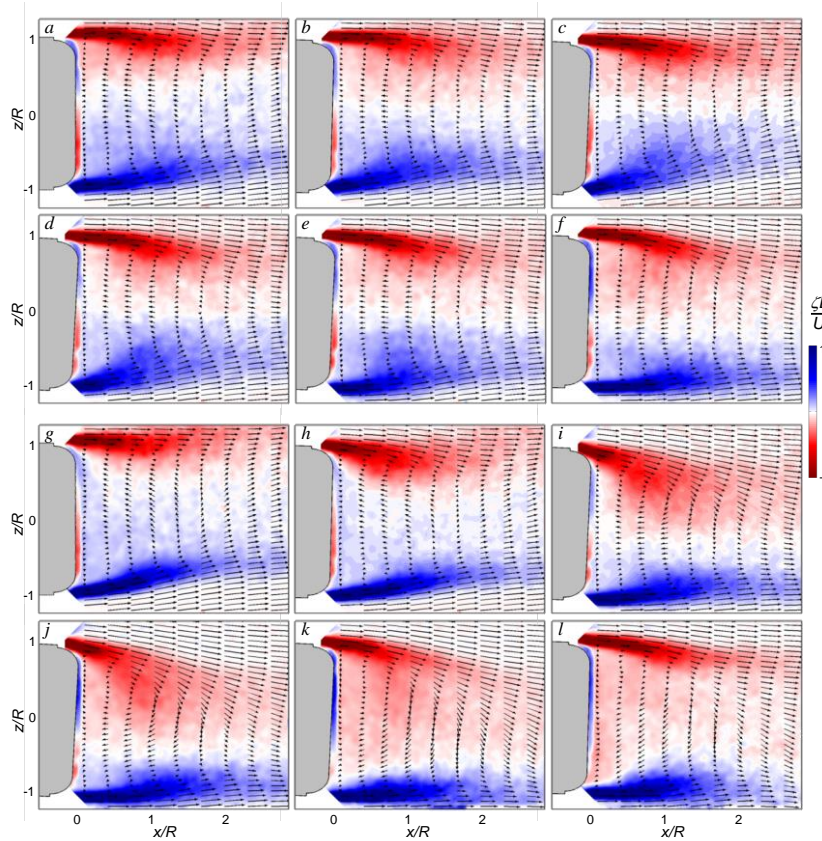


Figure III.55 Raster plots of the phase-averaged vorticity field with overlaid phase-averaged velocity vectors for $\alpha_y = \pm 3^\circ$ sinusoidal pitch at reduced frequency of $k = 0.259$ using force cancellation (a-f), and augmentation (g-l) at $t/\tau = 0$ (a,g), 0.083 (b,h), 0.167 (c,i), 0.25 (d,j), 0.333 (e,k), and 0.417 (f,l).

modulation at this 'high' frequency lags the modulation at the 'low' frequency by 40° , the flow observed through Figures III.55a-f remains more symmetric than the baseline cases shown in Figure III.48g to Figure III.55l. This is owing to the aerodynamic force and moment response on the model also inherently lagging the model motion with a similar delay. For 'high' frequency F_L vs. α_y augmentation (Figure III.55g-l), the opposite modulation command to the actuators is sent as in Figure III.55a-f. Initially, the model shear layer is deflected upward as it is lagging the model position, and the bottom jet is moderately actuated in Figure III.55g. As the model pitches up through Figures III.55g-i ($0 < t/\tau < 0.167$), the bottom actuation is terminated and transitions to increasing top actuation in Figures III.55c-e ($0.167 < t/\tau < 0.333$). In the time instances shown in Figures III.55e-f ($0.333 < t/\tau < 0.417$), the modulation of the top actuation is reduced. Comparing Figures III.55g-l and Figures III.48g-l show the increased time of transition of the wake ζ , is commensurate with the growth of hysteresis in Figure III.52d, as well as the increased extent of the shear layer is commensurate with the growth of the F_L peaks during actuation.

A detailed investigation analogous to the 'low' frequency pitch oscillations is conducted at the highest k to gain a better understanding of the 'high' frequency wake dynamics of the F_L vs. α_y cancellation and augmentation, and their similarities and differences to the 'low' frequency case.

0.259, oscillation flow control cases are also analyzed in detail with the phase averaged flow field measured by PIV, and represented in the same fashion as Figure III.53, over half of the pitching cycle. Based on Figure III.51, the actuation chosen for this value of k lags α_y in phase by 45° . In Figure III.55a, α_y has reached 0° and the top jet is moderately actuated. As the model pitches up through Figures III.55a-b ($0 < t/\tau < 0.083$), the top actuation is decreased, and transitions to the bottom jet, with increasing intensity in Figure III.55c-e ($0.167 < t/\tau < 0.333$).

Between Figures III.55e-f ($0.333 < t/\tau < 0.417$), the bottom actuation begins to decrease. It should be noted that although the

To do this, the time development of u_x , u_z , and ζ are presented for the 'high' frequency $k = 0.259$, showing the same comparisons as for the 'low' $k = 0.013$ (Figure III.54). Figure III.56a shows the development of u_x when there is no actuation present, where u_x responds as a sinusoid with the same $\sim 45^\circ$ phase lag behind α_y . Figure III.56d shows u_z development in the baseline flow, with a different structure than what was observed in the lower frequency case in Figure III.54d. Here, u_z is mostly downward when u_x is deflected downward, and u_z is mostly upward when u_x is deflected upward, showing the same $\sim 45^\circ$ phase lag from α_y observed in u_x . It is also notable that the magnitude of the baseline u_z is significantly smaller at this higher frequency (compare III.54d and III.56d). The baseline ζ development over the pitching cycle is shown in Figure III.56c, which follows α_y with $\sim 45^\circ$ phase lag in agreement with the streamwise and vertical velocity components. The structure of the ζ agrees well with the structure observed in the 'low' k pitching. Upon F_L vs. α_y cancellation actuation, the wake's variation in u_x decreases significantly throughout the cycle from the baseline, as shown in Figure III.56b, and conversely, the wake's variation in u_x increases significantly with the F_L vs. α_y augmentation actuation, as shown in Figure III.56c, in the same fashion as $k = 0.013$, with the exception that u_x now lags the model motion (compare Figures III.56a-c with Figures III.54a-c). At this 'high' frequency oscillation, there is a smaller effect in the vertical direction, compared to low frequencies, where F_L vs. α_y cancellation (Figure III.56e) does not change the magnitude of u_z , but instead slightly delays its development in time. The F_L vs. α_y augmentation (Figure III.56f) dominates the baseline u_z development seen in Figure III.56d, and causes an increase in magnitude of u_z . The response of ζ to F_L vs. α_y cancellation is shown in Figure III.56h, which manipulates the sense of ζ such that the region of zero ζ remains close to the centerline. Comparing Figure III.56h to Figure III.54h, the suppression of the vertical range of zero ζ is fundamentally similar, but the shear layer spreading is reduced. Although the structure is somewhat different, as the vertical range of zero

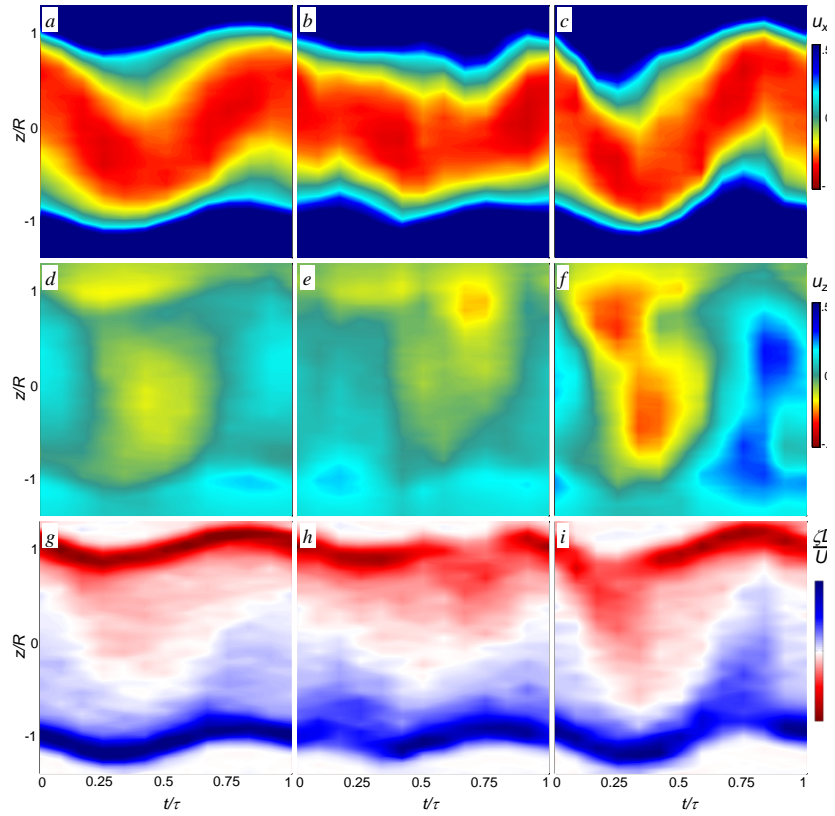


Figure III.56. Time development of streamwise (a-c) and cross-stream (d-f) velocity and vorticity (g-i) at a streamwise location of $x/R = 1$ from the model aft end for $\alpha_y = \pm 3^\circ$ sinusoidal pitch at reduced frequency $k = 0.259$, without actuation (a,d,g), and for the force cancellation (b,e,h) and augmentation (c,f,i).

ζ is still suppressed, the corresponding F_L vs. α_y on the body is also successfully reduced. The ζ response to F_L vs. α_y augmentation (Figure III.56i) instead involves an increase in the ζ in the wake, which increases the deviation of the zero level of ζ in the wake, commensurate with the augmentation of force measured in Figure III.52d. The two major differences between Figure III.56i and Figure III.54i are the phase lag of the response of the wake, and the reduced spreading of the shear layer.

IV. Summary

This research program focused on a fundamental investigation of the control of aerodynamic steering forces and moments on a wire-mounted subsonic ogive projectile model ($D = 90$ mm, $L = 165$ mm,) by fluidic modification of its apparent aerodynamic shape. The flow control approach exploits controlled, interactions of integrated fluidic actuation with the cross flow to induce localized, asymmetric flow attachment and thereby alter the near wake and the global aerodynamic forces and moments. Control was effected by an array of four synthetic jet actuators that emanate from azimuthally-segmented slots of height $h_J = 0.38$ mm and exit area $A_J = 13.03$ mm², equally distributed either around the perimeter of a ring-like Coanda surface at the tail section of the model. This flow control approach was tested in several stages: *i.* static model, *ii.* moving model at prescribed angles of attack, *iii.* single degree of freedom freely yawing model, and *iv.* dynamically moving model in a six degree of freedom traverse.

Initially each of the support wires includes a controllable, in-line shape memory alloy (SMA) segment that was coupled with miniature in-line force sensors. The system enabled arbitrary static orientations and quasi-static model motions in combinations of pitch and yaw with a range of attitude angles from $\pm 3^\circ$ at 0.5 Hz to $\pm 1^\circ$ at 5 Hz. In addition to the force measurements, the model near wake was characterized using PIV measurements in the vertical symmetry plane. Three configurations (base flow without actuation, and actuation with the top and bottom jets) were tested when the static model was aligned with the free stream, and both aerodynamic and fluidic-control-induced forces demonstrated close agreement with earlier static measurements (Abramson et al. 2011, 2012). Static measurements over a range of $\pm 4.5^\circ$ pitch angles were conducted using SMA wire activation, and the variation of the effectiveness of the control jets with pitching angle was assessed. It was found that the static aerodynamic pitch-induced forces and fluidic control-induced forces were comparable in magnitude over this range. It was also found that the optimal pitch angle for maximum actuation-induced lift and moment occurred when an actuator was inclined into the free stream by $\sim 1^\circ$. This off-axis peak is attributed to the model tail geometry and a presence of backward-facing step upstream from the Coanda surface, which defines a preferable flow alignment over the control jet orifice.

The static investigations were followed by measurements of the effects of quasi-steady, dynamic variation of the model's pitch angle for a time-resolved transient pitching step of 1.5° . Measurements in the base flow defined the terminal force and moment that the model attains upon step variation of the pitch angle. The introduction of step actuation during the pitching step cycle induced modification of the resulting forces and moments on the model causing it to physically displace to a different terminal pitching angle. In this scenario, the lift force is successfully dampened or augmented depending on the direction of the fluidic control applied relative to the direction of the transient pitching step. The model's pitch angle was then set to quasi-sinusoidal motion with a frequency of 1 Hz (reduced frequency of 0.013) and amplitude of 1.5° using time-dependent actuation of the SMA wires. It was shown that the magnitude of the

motion-induced forces and moments are similar to the static values at corresponding angles of attack. Fluidic actuation was used to either suppress or enhance the motion induced aerodynamic forces in an open-loop control scheme, as the model was undergoing oscillatory pitch. In addition, the suppression of aerodynamic forces was also successfully applied in only half of the model oscillation period, demonstrating the potential for control authority using prescribed aerodynamic forces that can be ultimately implemented for the stabilization and steering of airborne axisymmetric platforms during flight.

A single degree of freedom support system of the axisymmetric model was designed and built to enable 'free' model dynamic motion in yaw, in the absence and presence of aerodynamic flow control. The model was supported by a vertical thin steel wire and was secured such that there is minimal friction, translational and rotational vibrations. Flow control utilized two aft independently-driven synthetic jet actuators centered about the plane of the model yawing motion. The model's yaw motion was characterized using a laser vibrometer aligned with the yaw plane, and planar PIV measurements were utilized to characterize the coupled aft flow and near wake dynamics. It is found that, in the absence of actuation, the interaction of the cross flow with the model leads to natural time-periodic yaw oscillations which are attributed to a phase lag between the wake responses (and in turn force/moment response) and the dynamic body orientation. The predominant oscillation frequency and the oscillation amplitude are both directly proportional to the free stream speed. Open-loop continuous actuation with either one or both control jets demonstrated that such a control scheme can be applied to either suppress natural oscillations of the model by up to about 60%, or to shift the center of the body oscillations, along with suppression in amplitude. Open-loop actuation was used to characterize the time scale at which the full actuation effect is established, and it was found that the transient effects of the actuation onset die out in less than 1.5 convective time scales. Transient coupling between the jet actuation onset and the flow/wake response also revealed that an observed dominant vectoring effect can be attributed to a train of small-scale vortical structures that are induced by the actuation and interact with the near wake. To fully exploit the capabilities of active flow control to steer the attitude of the dynamically yawing model, a PID closed-loop control was developed and utilized to effect a desired trajectory. The model's measured displacement was used as the control input, while the amplitude modulation of both of the jets prescribed outputs at the fixed actuation frequency served as control output. These investigations demonstrated that this closed-loop control is capable of dramatically suppressing the model's unstable yaw oscillations, in excess of 90% in some instances. Furthermore, in reversed operation, the same control scheme can dramatically amplify natural oscillation by more than 200% of the natural amplitude. Finally, closed-loop control was used to deflect the body relative to the free stream and maintain a steady nonzero yaw angle.

Finally, a new 6-DOF model support and traversing mechanism was developed during the last phase of the project. The traverse utilizes a novel approach for providing dynamic wired support of a wind tunnel model, which is suspended by eight wires with servo actuators that control the end points and tensions in each wire. This mechanism is designed to move all the wires in patterns that cause rotation in three independent axes: roll ($\pm 8^\circ$), pitch ($\pm 15^\circ$), and yaw ($\pm 9^\circ$), and independent translations: streamwise, cross-stream, and vertical, all within a range of ± 50 mm. Each wire has an incorporated load cell that resolves the tension in each wire, and thereby captures the aerodynamic forces and moments on the model. Motion is effected by an in-house real-time PID controller that provides signals to the servo actuators as commanded. The

executed motion is recorded by an external six degree of freedom *Vicon* camera system (600 fps), which output is fed into the controller as a feedback signal to maximize the accuracy of motion. The real-time control system utilizes two *Quanser* Q8 real time data acquisition boards that are used for signal communication of the motor commands, the motor encoders, the actuator commands, and the load cells measured. The controller also has eight available output channels for external trigger signals as well as modulation signals to be implemented with the model-embedded flow control elements.

The final element of the present research work was focused on fluidic flow control applications to a moving aerodynamic platform, and coupling to and altering of the resulting aerodynamic forces and moments. The flow control concepts were demonstrated on an axisymmetric model having a prescribed sinusoidal pitch oscillations at a range of reduced frequencies $0 < k < 0.259$. In contrast to the earlier work on a single degree of freedom model, where the flow control was applied to either suppress or augment a body motion which was free to oscillate under the aerodynamic moment, this study focused on control of the motion-induced aerodynamic forces and moments while the body's dynamic path is prescribed and preserved.

The traverse-driven model motion was tested in multiple degrees of freedom, and it could generate desired complex trajectories, comprised of the combined translational and rotational motions. These trajectories could be realized with minimal error compared to the commanded motion, being executed in a PID control loop having feedback from the motion analysis system. Flow control capabilities were demonstrated on the model undergoing sinusoidal pitch oscillations. Actuation was effected by either continuous or modulated activation of two opposite synthetic jets on the model's aft end. Actuation by either jet induces a normal force and moment of opposite sense relative to the aerodynamic forces and moments. Hence, depending on which jet is activated, flow control was utilized to either suppress the aerodynamic moment (and augment the force) or augment the moment (and suppress the force). These actuation realizations were then implemented into an open-loop flow control scheme with adjustable phase offset of actuation relative to the model's period of oscillation. The resulting suppressed/enhanced pitch moment/lift force (and vice versa) flow control schemes were executed during the sinusoidal pitch motion, indicated a robust flow control effect over the full range of the tested pitch frequencies ($0 < k < 0.259$). The aerodynamic force and moment could be varied by as much as 50% of their uncontrolled levels indicating capabilities for steering and stabilization of a free-flying platform without moving (mechanical) control surfaces.

V. PERSONNEL

Prof. Ari Glezer: Principal Investigator

Bojan Vukasinovic: Research Engineer

Thomas J. Lambert: Graduate Research Assistant

VI. PUBLICATIONS

Lambert, T.J., Vukasinovic, B., and Glezer, A., “Aerodynamic Flow Control of a Moving Axisymmetric Bluff Body”, *AIAA Paper* 2014-0932.

Lambert, T.J., Vukasinovic, B., and Glezer, A., “Yaw Control of a Moving Axisymmetric Body using Synthetic Jets”, *AIAA Paper* 2013-0106.

Lambert, T.J., Vukasinovic, B., and Glezer, A., “Unsteady Aerodynamic Flow Control of a Wire-Suspended, Moving Axisymmetric Body”, *AIAA Paper* 2012-0073.

Abramson, P., Vukasinovic, B., and Glezer, A., Fluidic Control of Aerodynamic Forces on a Bluff Body of Revolution, *AIAA J.* **50**, pp.832-843, 2012.

Abramson, P., Vukasinovic, B., and Glezer, A., Direct Measurements of Controlled Aerodynamic Forces on a Wire-suspended Axisymmetric Body, *Exp. Fluids* **50**, pp.1711-1725, 2011.

IN PREPARATION

Lambert, T.J., Vukasinovic, B., and Glezer, A., “Aerodynamic Flow Control of a Wire-Suspended, Pitching Axisymmetric Body”, *to be submitted to AIAA J.*

Lambert, T.J., Vukasinovic, B., and Glezer, A., “Controlled Stability Characteristics of a Moving Axisymmetric Platform using Fluidic Actuation,” *to be submitted to J. Fluid Mech.*

REFERENCES

- Abramson, P., Vukasinovic, B., and Glezer, A., "Direct Measurements of Controlled Aerodynamic Forces on a Wire-suspended Axisymmetric Body", *Exp. Fluids*, Vol. 50, 2011, pp. 1711-1725.
- Abramson, P., Vukasinovic, B., and Glezer, A., Fluidic Control of Aerodynamic Forces on a Bluff Body of Revolution, *AIAA J.*, Vol. 50, 2012, pp. 832-843.
- Amitay, M., Smith, D. R., Kibens, V., Parekh, D. E., and Glezer, A., "Aerodynamic Flow Control over an Unconventional Airfoil Using Synthetic Jet Actuators", *AIAA J.*, Vol. 39, 2001, pp. 361-370.
- Barrett, R. M., Lee, G. M., "Design and Testing of Piezoelectric Flight Control Actuators for Hard Launch Munitions," *Proc. SPIE* 5390, Smart Structures and Materials 2004: Smart Structures and Integrated Systems, 459, 2004.
- Chang, R. C., Hsiao, F. B., and Shyu, R. N., "Forcing Level Effects of Internal Acoustic Excitation on the Improvement of Airfoil Performance", *J. Aircraft*, Vol. 29, 1992, pp. 823-829.
- Corke, T. C., Tillotson, D., Patel, M. P., Su, W. J., Toldeo, W., "Radius Flow Vectoring for Projectile Drag and Steering Control Using Plasma Actuators", *AIAA Paper* 2008-3769, 2008.
- Englar, Robert J., "Circulation Control Pneumatic Aerodynamics: Blown Force and Moment Augmentation and Modification; Past, Present, & Future", *AIAA Paper* 2000-2541.
- Erk, P. P., "Separation Control on a Post-stall Airfoil using Acoustically Generated Perturbations", PhD Thesis, Tech. Univ. Berlin, Germany, 1997.
- Freund, J. B., Mungal, M. G., "Drag and Wake Modification of Axisymmetric Bluff Bodies Using Coanda Blowing", *J. Aircraft*, Vol. 31, 1994, pp. 572-578.
- Glezer, A., Amitay, M., and Honohan, A. "Aspects of Low- and High-Frequency Actuation for Aerodynamic Flow Control," *AIAA Journal*, Vol. 43, 2005, pp. 1501-1511.
- Higuchi, H., Van Langen, P., Sawada, H., Timney, C. E., "Axial Flow Over a Blunt Circular Cylinder With and Without Shear Layer Reattachment", *J. Fluids Struct.*, Vol. 22, 1996, pp. 949-959.
- Hoerner, S. F., *Fluid-Dynamic Drag*, Hoerner Fluid Dynamics, Bricktown, New Jersey, 1965.
- Honohan, A. M., Amitay, M., and Glezer, A., "Aerodynamic Control using Synthetic Jets", *AIAA Paper* 2000-2401, 2000.
- Hsiao, F. B., Liu, C. F., and Shyu, J. Y., "Control of Wall-Separated Flow by Internal Acoustic Excitation", *AIAA J.*, Vol. 28, 1990, pp. 1440-1446.
- Lo, K. P., Elkins, C. J., Eaton, J. K., "Separation Control in a Conical Diffuser with an Annular Inlet: Center Body Wake Separation", *Exp. Fluids*, Vol 53, 2012, pp 1317-1326.
- McMichael, J., Lovas, A., Plostins, P., Sahu J., Brown, G., and Glezer, A., "Microadaptive Flow Control Applied to a Spinning Projectile", *AIAA Paper* 2004-2512, 2004.
- Murphy, C. H., "Some Special Cases of Spin-Yaw Lock In", US Army Ballistic Research Laboratory, BRL-MR-3609, 1987.

Murphy, C. H., "Symmetric Missile Dynamic Instabilities", *AIAA J. Guidance and Control*, Vol. 4, No. 5, 80-0320R, 1980.

Nagib, H. M., Reisenthel, P. H., and Koga, D. J. "On the Dynamical Scaling of Forced Unsteady Flows", *AIAA Paper* 1985-0553, 1985.

Nemat-Nasser, S., Guo, W. G., "Superelastic and cyclic Response of NiTi SMA at various strain rates and temperatures", *Mechanics of Materials*, Vol. 38, 2006, pp. 463-474.

Neuberger D. and Wygnanski I., "The Use of a Vibrating Ribbon to Delay Separation on Two Dimensional Airfoils", Proceedings of Air Force Academy Workshop in Unsteady Separated Flow (Colorado Springs, CO), F.J Seiler, ed., Report TR-88-0004, 1987.

Newman, B.G., "The Deflexion of Plane Jets by Adjacent Boundaries-Coanda Effect", *Boundary Layer and Flow Control Principles and Applications*, Vol. 1, 1961, pp. 232-264.

Nicolaides, J. D., "A History of Ordnance Flight Dynamics", *AIAA Paper* 70-533, 1970.

Ollerenshaw, D., Costello, M., "Model Predictive Control of a Direct Fire Projectile Equipped with Canards," *Journal of Dynamic Systems, Measurement, and Control*, Vol. 130, 061010, 2008.

Ollerenshaw, D., Costello, M., "Simplified Projectile Swerve Solution for General Control Inputs," *Journal of Guidance, Control, and Dynamics*, Vol. 31, 2008, pp. 1259-1265.

Price Jr., D. A., "Sources, Mechanisms, and Control of Roll Resonance Phenomena for Sounding Rockets.", *AIAA J. Spacecraft*, 4, No. 11, 1967, pp. 1516-1521.

Rinehart, C., "Aerodynamic Forces Induced by Controlled Transitory Flow on a Body of Revolution", Ph. D. Thesis, Georgia Institute of Technology, 2011.

Rinehart, C., McMichael, J. M., and Glezer, A., "Transitory Flow and Force Development on a Body of Revolution Using Synthetic Jet Actuation", *AIAA Paper* 2003-0618, 2003.

Sahu, J., "Time-Accurate Computations of Free-Flight Aerodynamics of a Spinning Projectile with and without Flow Control", *AIAA Paper*, 2006-6006.

Seifert, A., Bachar, T., Koss, D., Shepshelovich, M. and Wygnanski, I., "Oscillatory Blowing: A Tool to Delay Boundary-Layer Separation", *AIAA J.*, Vol. 31, 1993, pp. 2052-2060.

Smith, D. R., Amitay, M., Kibens, V., Parekh, D., and Glezer, A., "Modification of Lifting Body Aerodynamics Using Synthetic Jet Actuators", *AIAA Paper* 1998-0209, 1998.

Williams, D., Acharya, M., Bernhardt, K. & Yang, P., "The Mechanism of Flow Control on a Cylinder with the Unsteady Bleed Technique", *AIAA Paper* 1991-0039, 1991.

Wu, J.-Z., Lu, X.-Y., Denny, A. G., Fan, M., and Wu, J.-M., "Post Stall Flow Control on an Airfoil by Local Unsteady Forcing," *Journal of Fluid Mechanics*, Vol. 371, 1998, pp. 21-58.

Zäk, A. J., Cartmell, M. P., Ostachowicz, W. M., Wiercigroch, M. "One-dimensional shape memory alloy models for use with reinforced composite structures", *Smart Materials and Structures*, Vol. 12, 2003, pp. 338-346